Dissertation

submitted to the

Combined Faculties of the Natural Sciences and Mathematics

of the Ruperto-Carola-University of Heidelberg. Germany

for the degree of

Doctor of Natural Sciences

Put forward by

MPhys BSc Tanya Edwards

born in Durban, South Africa

Oral examination: 18 January 2017

Separation of γ-Ray, Electron and Proton induced Air Showers applied to Diffuse Emission Studies with H.E.S.S.

Referees: Prof. Dr. Werner Hofmann
Prof. Dr. Stefan Wagner

Abstract

A fundamental issue in ground-based gamma-ray astronomy is the identification of γ-ray events among the overwhelming background of air showers induced by charged cosmic rays. Reconstruction techniques exist to distinguish most of the background of hadrons but an irreducible background of electrons and gamma-like protons still remain. I present here a new technique making use of high-altitude Cherenkov light emitted by the charged primary particle and air shower development properties. This method provides a way to distinguish between electrons and gamma rays on a statistical basis. In addition to this, the remaining proton background can also be identified. The technique was developed, tested and applied to studies using the High Energy Stereoscopic System (H.E.S.S.) located in Namibia.

The analysis method is especially important in the detection of diffuse signals and eliminates the necessity of a background region in the field of view. The technique was applied to three scientific studies.

The latitude profile of the Galactic diffuse γ-ray emission was analysed. A width of σ = 0.25±0.05° (0.20±0.06°) for energies of 380 to 900 GeV (1 to 6 TeV) was determined. The cosmic electron spectrum was measured between 0.38 and 14 TeV and a broken power law was fit to the data. The spectrum steepens from Γ = 3.08±0.06 to Γ = 3.72±0.12 at a break in energy of 1.11±0.04 TeV. In addition, upper limits on the maximum γ-ray contamination from the Isotropic γ-Ray Background was placed at 4×10^{-3} (5×10^{-3}) MeV cm^{-2} s^{-1} sr^{-1} for energies of 1 to 6 TeV (380 to 900 GeV).

Zusammenfassung

Ein fundamentales Problem der bodengestützten Gammaastronomie ist die Identifizierung von Gammastrahlen vor dem überwältigenden Hintergrund der Luftschauer die von der geladenen kosmischen Strahlung erzeugt werden. Es existieren Rekonstruktionsmethoden um den Hauptteil des Hintergrundes der Hadronen zu unterscheiden, aber ein nicht reduzierbarer Hintergrund aus Elektronen und Gamma-ähnlichen Protonen bleibt übrig. In dieser Arbeit präsentiere ich eine neue Technik, welche das Cherenkov Licht, das von dem geladenen Primärteilchen in großer Höhe erzeugt wird und die Eigenschaften der Luftschauer Entwicklung ausnützt. Diese Methode ermöglicht es statistisch zwischen Elektronen und Gamma Strahlung zu unterscheiden. Zusätzlich kann der übrig gebliebene Hintergrund der Protonen identifiziert werden. Diese Technik wurde für Studien am High Energy Stereoscopic System (H.E.S.S.) in Namibia entwickelt, getestet und angewendet.

Diese Analysemethode ist besonders wichtig für die Detektion von diffusen Signalen und macht die Notwendigkeit eines Hintergrundfeldes im Sichtfeld überflüssig. Die Technik wurde bei drei wissenschaftlichen Studien angewendet.

Das Breitengrad Profil der galaktischen diffusen Gammastrahlung wurde analysiert. Eine Breite von σ = 0.25±0.05° (0.20±0.06°) für Energien von 380 bis 900 GeV (1 bis 6 TeV) wurde ermittelt. Das kosmische Elektronenspektrum wurde zwischen 0.38 und 14 TeV gemessen und ein gebrochenes Potenzgesetz wurde an die Daten gefittet. Bei einer Energie von 1.11±0.04 TeV wird das Spektrum steiler und der Exponent ändert sich von Γ = 3.08±0.06 zu Γ = 3.72±0.12. Zusätzlich wurde ein oberer Grenzwert für die maximale Gammastrahlen Kontamination von dem isotropen Gammastrahlenhintergrund bestimmt, mit Werten von 4×10^{-3} (5×10^{-3}) MeV cm^{-2} s^{-1} sr^{-1} für Energien von 1 bis 6 TeV (380 bis 900 GeV).

Contents

Introduction

The field of γ-ray astronomy has seen much development over the past decade. Since its full operation began in 2004, H.E.S.S. has expanded the TeV sky with the discovery of more than 70 very high energy (VHE) γ-ray sources in the Milky Way. As an array of five Imaging Atmospheric Cherenkov Telescopes (IACTs), the H.E.S.S. array has the ability to detect air shower cascades initiated by γ rays as well as cosmic rays (CRs).

Part of the success of ground based Cherenkov telescopes is the background suppression techniques used in identifying a γ-ray signal. As the overwhelming majority of extensive air showers (EAS) produced in the atmosphere are from hadronic CRs, powerful analysis methods have to be utilized to identify a small fraction of γ rays.

Using image analysis techniques makes this possible. Characteristics of the air shower development of hadronic and electromagnetic EAS can be studied with simulations. Identifying the ways in which these characteristics effect the air shower images produced in the telescope camera gives a basis on which to discriminate hadronic and electromagnetic (EM) induced air showers.

The analyses successfully reject nuclei heavier than protons and a large proportion of the proton background. However, a small fraction of incoming protons initiate cascades that are not identifiable from γ-ray initiated ones with current techniques. As the flux of CR protons is much higher than the flux of the brightest γ-ray sources, this misclassification of protons is comparable to the flux level of a strong γ-ray signal.

Furthermore, CR electrons are not distinguished from γ rays. Once a rejection of the background has been made, the fraction of electrons in the data becomes comparable to

protons.

An analysis method was developed to identify the remaining contribution of γ rays, electrons and protons. The background rejection power of the technique was assessed and systematic studies were carried out to estimate its accuracy.

The method is especially important in studies on diffuse emission. In order to study a γ-ray emission region, a comparison of a region containing no γ-ray sources is needed. When observing regions of the sky where the emission of γ rays extends further than the field of view, defining reliable background regions is not possible. This new method eliminates the necessity of a background region, making it ideal for studies on diffuse emission.

A study on the diffuse γ ray emission in the inner part of the Milky Way was carried out. The Galactic latitude profiles were studied at energies between 0.38 and 3 TeV.

The method was also applied to other diffuse studies. Upper limits of the Isotropic γ-ray Background (IGRB) were placed at 640 GeV and 3.5 TeV. Placing a constraining upper limit on the IGRB with an IACT array is ambitious, as the estimated IGRB flux is $\approx$ 2% of the total cosmic ray electron (CRE) flux. Hence, the upper limits placed are not constraining for models on the IGRB. Nevertheless, the upper limit placed at 1 to 6 TeV provides an estimate of the maximum contribution of isotropic γ rays.

The CRE spectrum was studied between energies of 0.38 and 14 TeV. The method provides an independent analysis of CREs from previous studies. The spectrum is compatible with previous measurements when statistical uncertainties are taking into account. However, the spectral index found in this study is less steep above the break in energy at $\approx$ 1 TeV compared to previous H.E.S.S. measurements.

CHAPTER 1

Extensive Air Showers

An Extensive Air Shower (EAS) is the term used to describe the cascade of particles that develops when a cosmic particle enters the atmosphere. Cosmic rays and photons entering the atmosphere interact with air molecules, producing a cascade of particles that grows as the shower propagates towards ground level until a maximum is reached, called the shower maximum (X_{max}). After this point, the air shower decreases in size.

The air shower can be categorized by the type of interactions involved as the cascade develops: hadronic and electromagnetic. An EAS initiated by a hadronic primary involves both hadronic and electromagnetic interactions. Air showers produced by electrons, positrons and photons only involve electromagnetic interactions. The topology and other properties of an EAS depends on which process is dominant.

1.1 Electromagnetic Air Showers

1.1.1 Air Shower Cascades

Electromagnetic air showers are named according to the interactions responsible for the developing cascade. In a simplified view, these showers consist of mainly photons and electrons. Compton scattering, pair production and the photoelectric effect are the main processes through which photons interact, while the processes dominating electron interactions are ionisation, excitation and bremsstrahlung.

When an electron decelerates in the presence of an electric field surrounding an atmospheric nucleus, the loss in kinetic energy results in a photon given off. This process is

known as Bremsstrahlung radiation, with the average energy loss rate defined below:

$$-\frac{\partial E}{\partial X} = \frac{E_0}{X_r} \tag{1.1}$$

where X_r is the radiation length. The radiation length is dependent on the type of medium the particle is travelling through. It is defined as the average distance an electron travels before losing $1/e$ in primary energy:

$$E(x) = E_0 e^{\frac{-x}{X_r}} \tag{1.2}$$

where $E(x)$ is the average energy at distance x. Another way to compare air showers and their characteristics is to describe their development in steps of radiation lengths rather than absolute distances. This gives a relative scale of the amount of matter traversed to model air shower cascades. The radiation length of a medium can be calculated with the following equation:

$$\frac{1}{X_r} = 4\alpha r_e^2 \frac{N_A}{A}\left(Z\,(Z+1)\,ln\frac{183}{Z^{\frac{1}{3}}}\right) \tag{1.3}$$

where Z is the proton number, A is the molar mass, r_e is the radius of an electron and N_A is Avogadro's number. α is the fine structure constant ($\alpha = \frac{1}{137}$). The charge, Z, and atomic number, A, of the nuclei determines the radiation length as the strength of the electric field depends on the charge of the nuclei and its size is related to its atomic number. The radiation length does not depend on the primary energy and is solely determined by characteristics of the medium through which it is travelling. The standard value of X_r in air is 37.15 g cm^{-2} (Linsley 1985).

For photons at GeV energies, the most dominant process of interaction is through pair production. A photon is converted into an e^- e^+ pair, with each particle, on average, carrying forward 50% of the initial energy. The radiation length can be defined in terms of the mean free path of a photon (λ) as $X_r = \frac{7}{9}\lambda$, where λ has a value of 47.8 g cm^{-2}.

The Heitler model provides a simplified view of an electromagnetic air shower cascade by making the following three assumptions:

- Both electrons and photons have the same interaction length
- Pair production and bremsstrahlung are the only processes taking place

- An equal amount of energy is distributed at every interaction

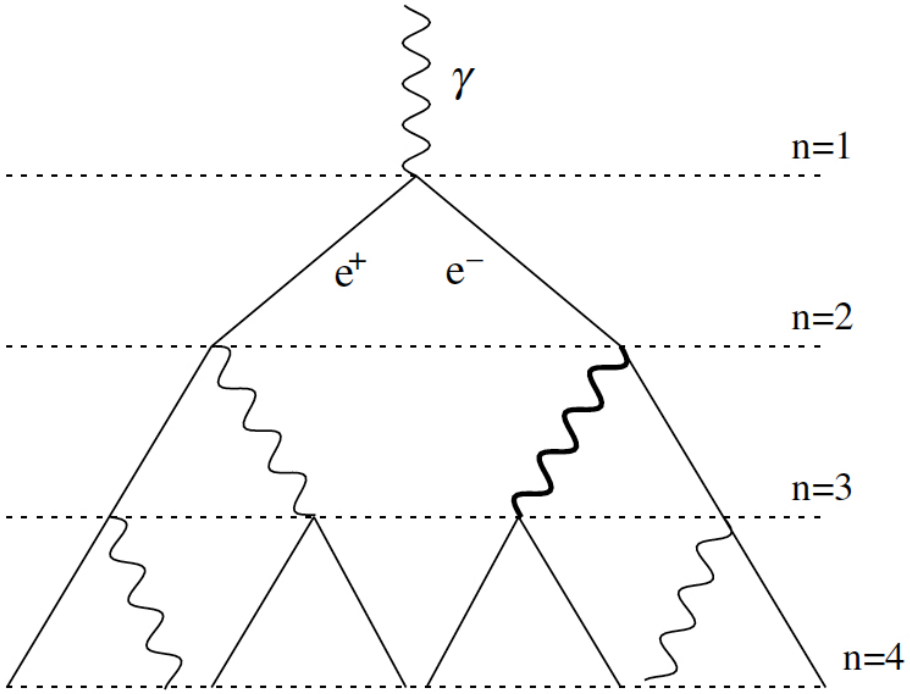

Figure 1.1: A schematic drawing of the Heitler Model for extensive electromagnetic air showers. The photon enters the atmosphere and interacts with nuclei to pair produce. A cascade of particles continue until a maximum is reached (Matthews 2005).

The Heitler model (Figure 1.1) provides a simplified way to estimate the development of electromagnetic showers. Each electron, positron or photon traverses the same distance, or splitting length, before undergoing either bremsstrahlung or pair production. At each interaction step, the total number of particles present in the cascade is multiplied by two. After a given number of splitting lengths, n, the total number of particles in the shower is 2^n. The air shower continues to expand until a maximum number of particles is reached, with the distance traversed being the *shower maximum* or X_{max}. After this point, the air shower

loses energy through ionisation rather than radiation and the cascade reduces in energy and size, with the particles getting absorbed by the surrounding molecules.

1.1.2 Shower Maximum

1.1.2.1 Heitler Model

The following derivation of the shower maximum requires the simplified assumptions made by the Heitler Model. The radiation length, X_r is proportional to the splitting length, d_{split} by (Heitler 1954; Matthews 2005):

$$d_{split} = X_r ln2 \tag{1.4}$$

The splitting length is the length the particles travel before interacting. d_{split} is found to be 25.8 g cm^{-2} when taking the standard value for X_r as 37.15 g cm^{-2}. The size of the shower at a given distance, x, is:

$$N = 2^n = e^{\frac{x}{X_r}} \tag{1.5}$$

where n is the number of splitting lengths travelled. The shower continues to expand until $N = N_{max}$ and the particles have an average energy equal to the critical energy, E_c. Particles with an energy lower than E_c have higher energy losses through ionisation than through bremsstrahlung or pair production. The value of E_c for an electromagnetic shower is 85 MeV. The number of particles reached at X_{max} is:

$$N_{max} = 2^{n_c} \tag{1.6}$$

The primary energy, E_0, is related to N_{max} by:

$$N_{max} = \frac{E_0}{E_c} \tag{1.7}$$

The radiation length is related to X_{max} and the corresponding number of splitting lengths, n_c, by:

$$X_{max} = n_c d = n_c X_r ln2 \tag{1.8}$$

Using Equation 1.7, an equation for estimating X_{max} is derived:

$$n_c = \frac{ln\frac{E_0}{E_c}}{ln2} \tag{1.9}$$

$$X_{max} = n_c X_r ln2 = X_r ln\frac{E_0}{E_c} \tag{1.10}$$

Equation 1.10 gives an estimate of the shower maximum. It is dependent on the energy of the primary photon, electron or positron entering the atmosphere, the critical energy at which energy losses due to ionisation dominate and the radiation length in air. These three values determine, on average, the properties of an electromagnetic cascade. For shower cascades in air, the single variable determining the variation in topology and size between individual air showers is the primary energy E_0, as X_r and E_c have constant values in air. As the Heitler model does not take into account all types of energy losses, the estimate provided by Equation 1.10 is a higher one. It is sometimes more useful to display X_{max} in units of radiation lengths:

$$t_{max} = ln\frac{E_0}{E_c} \tag{1.11}$$

The differences between photon induced showers and electron or positron initiated ones are not described by the Heitler model. An accurate description of the difference in X_{max} between electron and γ-ray induced air showers is an important property to quantify. Heitler suggested that, on average, a photon air shower cascade should develop one radiation length further into the atmosphere than an electron initiated one (Heitler 1954), resulting in a difference in X_{max} of one radiation length.

It should be noted that when comparing properties of air showers such as X_{max} or the first interaction, this can only be done on an average basis. In reality, individual air shower events have many fluctuations between them, and predicted behaviour can only be assumed in a large statistical framework.

1.1.2.2 Approximation B

In 1952 (Rossi 1952), a more theoretical approach of air shower cascades was taken. Similar to the Heitler model, *Approximation A* assumes only pair production and bremsstrahlung

interactions. Ionization losses were then introduced to formulate $Approximation\ B$. The energy deposited in a shower is:

$$\frac{dE}{dt} = E\beta\frac{(\beta t)^{\alpha-1}\, exp\,(-\beta t)}{\Gamma\,(\alpha)} \tag{1.12}$$

where α describes the shape, β the scaling factor and t the atmospheric depth in radiation lengths. The shower maximum is given as $t_{max} = \frac{\alpha-1}{\beta}$. Solving Equation 1.12 gives (Fabjan & Gianotti 2003):

$$t_{max} = 1.0\left(ln\left(\frac{E_0}{E_c}\right) + C_j\right) \tag{1.13}$$

where j represents the primary particle, j = e, γ. e denotes an electron primary and γ a photon primary. *Approximation B* finds values of $C_e = -1.0$ and $C_\gamma = -0.5$. This translates to a difference in X_{max} of half a radiation length between electrons and photons.

The Particle Data Group fit C_j for a range of elements between 1 and 100 GeV using EGS4, an electromagnetic shower package of CORSIKA (Heck 1998), and found $C_e = -0.5$ and $C_\gamma = +0.5$ for showers between 1 GeV and 100 GeV, giving a difference of one X_r (Olive et al. 2014).

1.2 Hadronic Air Showers

1.2.1 Air Shower Cascade

Hadronic showers can be thought of as numerous electromagnetic and hadronic sub-showers superimposed, involving both hadronic and electromagnetic interactions and a whole array of particles (e.g. π, K, p, n, e, μ, ν). The result is a complex spread of particles arriving at ground level at different times. The Heitler model was modified for hadronic interactions (Matthews 2005) and extended further to include all generations of sub-showers (Montanus 2014). For an incoming proton, the shower is initiated by:

$$p + p \rightarrow p + p + N + \pi^0 + \pi^+ + \pi^- \tag{1.14}$$

The pions then go on to decay through the following channels:

$$\pi^0 \rightarrow \gamma + \gamma \tag{1.15}$$

$$\pi^{\pm} \rightarrow \mu^{\pm} + \nu \tag{1.16}$$

$$\mu^{(\pm)} \rightarrow e^{(\pm)} + \nu_{(e)\mu} + \bar{\nu}_{e(\mu)} \tag{1.17}$$

The neutral pions that are produced in the first interaction go on to propagate EM showers through π^0 decay. Further hadronic particles are produced through charged pion processes. A small fraction of the electromagnetic sub-showers are produced by the decay of muons. The lifetime for π^0 is rather short, $\approx 8{\times}10^{-16}$s compared with $3{\times}10^{-8}$s for $\pi^{\pm}$. This allows enough time for the charged pions to propagate further before finally decaying and producing muons.

About a 1/3 of the primary energy is carried forward by the EM component and 2/3 by the hadronic one. The hadronic cycle continues until the charged pions have a higher probability of decaying than of further interactions, after which point the multiplicity of the shower stops.

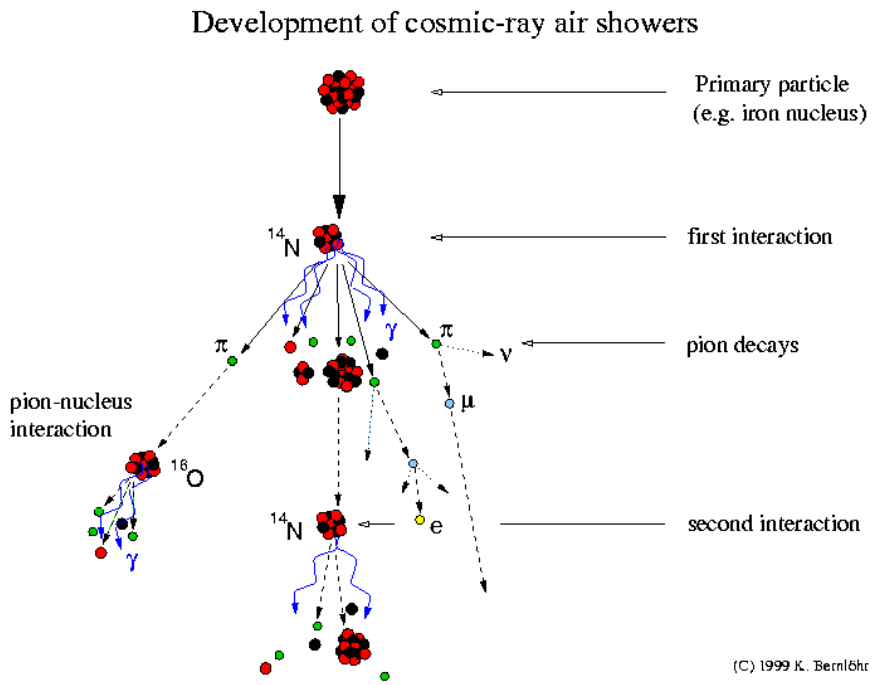

Figure 1.2: An illustration of the interactions involved in a hadronic air shower. Taken from (Bernlöhr 1999).

Although a larger fraction of energy is contained in the hadronic interactions, the majority of Cherenkov light produced originates from the EM component. Since $N_{max} = E_0/E_c$, the number of particles contained in the EM component is much higher than the hadronic one. This is due to the critical energy of pions being higher (E_c^{π} = 20 GeV) when compared to the critical energy of electrons (E_c^{e} = 85 MeV). Furthermore, the pions have a higher interaction length (λ_I^{π} = 120 g cm^{-2}), with hadronic showers multiplying over a splitting distance of $\sim$ 83 g cm^{-2} compared to the EM splitting length of $d_{split} = X_r ln2 \approx 26$ g cm^{-2}. Even with a higher multiplicity at each interaction step, this results in the hadronic sub-showers developing at a slower rate than its EM counterpart. Both of these effects contribute to the lower number of particles in the hadronic part of the air shower and therefore a lower Cherenkov light yield.

The large interaction length of a primary protons allows them to travel far into the atmosphere before initiating a cascade (Matthews 2005):

$$X_0 = \lambda_I^P ln2 \tag{1.18}$$

$$\lambda_I^P \approx 61 g cm^{-2}[1.0 - 0.1 ln(E_0/PeV)] \tag{1.19}$$

where X_0 is the atmospheric depth of the first interaction and λ_I^P the interaction length of a proton, approximately $\approx$ 103 g cm^{-2} at 1 TeV. The shower maximum can be conveniently compared with EM cascades as follows (Matthews 2005):

$$X_{max}^P = X_{max}^{\gamma} + X_0 - X_r ln\,(3N_{ch}) \tag{1.20}$$

with X_{max}^{γ} representing X_{max} in γ-ray induced air showers and N_{ch} the number of charged secondary particles arising from hadronic interactions. It follows that air showers from protons develop deeper into the atmosphere than electron or γ-ray initiated cascades.

As mentioned, hadronic showers generally have a more irregular topology than EM showers. However, heavier nuclei entering the atmosphere have less fluctuations in its Cherenkov profile. This is because extensive air showers induced by heavy nuclei can be considered as many proton showers superimposed. Their summed Cherenkov emission profiles minimize the amount of variations observed.

1.3 Atmospheric Cherenkov Radiation

1.3.1 Extensive Air Shower Radiation

When a charged particle travels through air, the associated electromagnetic field polarizes the surrounding molecules. This results in the closer air molecules aligning themselves towards the charge as it passes and then back to its original position, giving off dipole radiation as a result. When the speed of the particle is lower than the local speed of light, this radiation can be visualized as expanding rings of light that destructively interfere so that no radiation is detected at a distance.

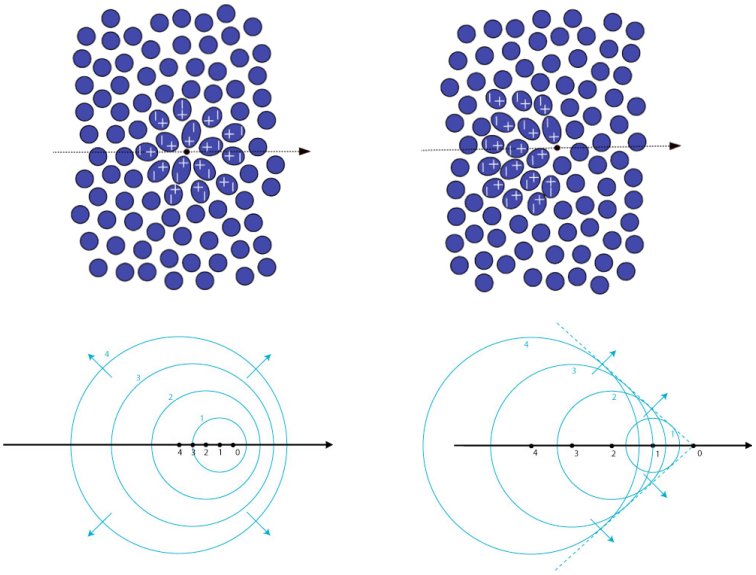

Figure 1.3: LEFT: Charged particles travelling through a medium will give off dipole radiation. RIGHT: When the particle travels with a velocity higher than the local speed of light, the radiation given off constructively interferes. Images taken from University of Minnesota (2004) and Skulls in the Stars (2009).

However, when the charged particle travels faster than the local speed of light, the surrounding molecules do not get the electromagnetic message that the particle is coming and do not align themselves until the particle has already passed. This creates concentric rings that now overlap and constructively interfere with each other (Figure 1.3), creating a wavefront of light known as *Cherenkov radiation*. This light travels towards ground level where it is reflected and then imaged by Imaging Atmospheric Cherenkov Telescopes (IACTs). Sim-

ulated Cherenkov light photons from a γ-ray and proton air shower arriving at ground level is shown in Figure 2.5. The angle at which the Cherenkov cone is produced at any point in the atmosphere can be found using:

$$cos\,(\theta) = \frac{1}{\beta n} \tag{1.21}$$

where n is the refractive index and $\beta = v/c$, with v representing the velocity of the particle and c the speed of light in a vacuum. The further into the atmosphere the charged particles travel, the higher the refractive index and the larger the angle of the Cherenkov cone emitted, as shown in Figure 1.4. All Cherenkov cones arriving at ground level will overlap to form a *light pool*, with photons emitted at a height of 30 km having an opening angle of $\sim 0.2^{\circ}$ and a light pool of radius ~ 80 m. θ cannot exceed a value of 1.3°, as the maximum value of n, at sea level, is 1.00029.

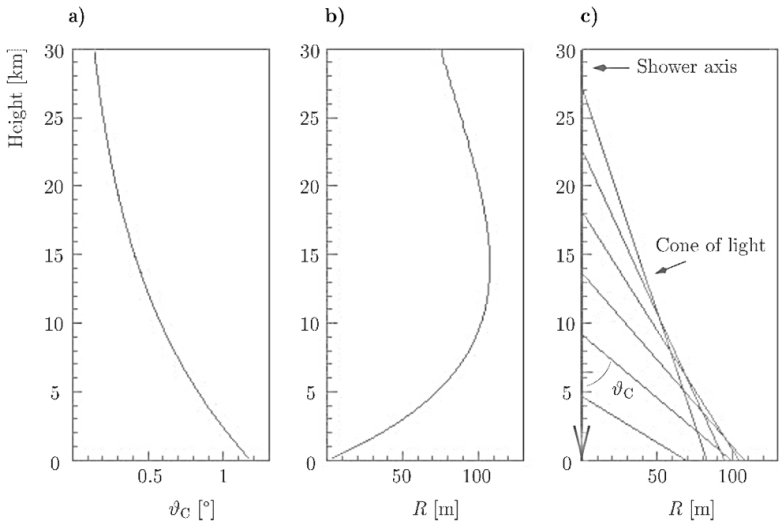

Figure 1.4: a) The Cherenkov emission half angle θ_c as a function of atmospheric height. As the incoming particle travels towards sea level, the emission angle increases due to the higher density of air. b) The size of the Cherenkov light pool reaching ground level. The radius of the light pool at ground level increases until an emission height of $\approx$ 10 km. Although the Cherenkov emission angle continues to increase, the proximity of the emission height to ground level prevents a larger light pool. c) The combined effect of the increasing angle of the Cherenkov light cone and the radius of light pool. Taken from (Ulrich 1996).

Cherenkov photons will peak at 330 nm, with photons having a wavelength between 300 and 600 nm. The number of Cherenkov photons given off can be described by the following equation:

$$\frac{dN_{ph}}{dx} = 2\pi\alpha z^2 \int_{\lambda_1}^{\lambda_2} sin^2\theta \, \frac{d\lambda}{\lambda^2} \tag{1.22}$$

The amount of Cherenkov light a single passing particle is responsible for is not dependent on its energy but rather its polarizing effect on the air, which is determined by its charge. However, when discussing Cherenkov light yield in the context of an EAS, the more energy an initiating cosmic ray or photon entering the atmosphere has, the more Cherenkov radiation produced in the shower as a whole. This is because a higher energy shower produces a higher number of particles, as shown in Equation 1.7, with each individual particle producing a number of Cherenkov photons determined by Equation 1.22.

1.3.2 Direct Cherenkov Light

Direct Cherenkov (DC) light is light given off as a direct result of the motion of the primary particle. It is defined as all light given off before the incoming charged particle undergoes its first interaction (Kieda et al. 2001).

There is a large variation in the distance a particle travels before interacting. Therefore, there is also a large variation in the amount of Direct Cherenkov light produced from event to event. The dependencies of the intensity of this light are the same as described for Equation 1.22.

The DC intensity at a given altitude does not depend on energy. For charged cosmic rays, the average atmospheric depth travelled before the first interaction is dependent on energy and so the Cherenkov light production scales with it. The relationship between DC light yield, altitude and energy has been studied in (Aharonian et al. 2007) and is shown in Figure 1.5. The number of DC photons produced is approximately constant with energy at heights above 30 km, where most first interactions take place.

The DC light yield is proportional to the charge of the particle squared. This relationship between light yield and charge provides a unique way to identify the primary particle initiating the air shower. For heavier nuclei, the DC component is comparable to the EAS light yield. Electrons and protons, on the other hand, have a charge of 1 and therefore the lowest DC

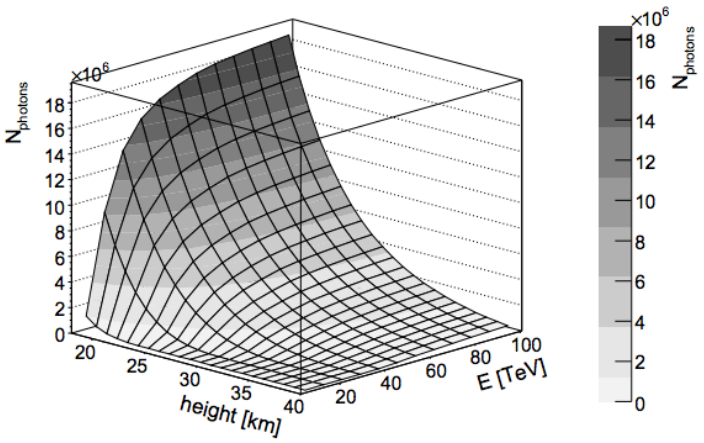

Figure 1.5: Number of DC photons given off at different first interaction heights and energies E. Events were produced at one zenith angle of 0°. Taken from (Aharonian et al. 2007).

intensity. Further discussion on how this intensity compares with the EAS light is provided in Chapter 3.

The condition to produce Cherenkov light is that the energy of the particle is larger than the local speed of light, $v_{CR} \geq c$. The energy threshold for Cherenkov light production can be calculated as:

$$E_{thr}(h) = \sqrt{\frac{\gamma^2 + m_0^2}{n(h)^2} + m_0^2} \tag{1.23}$$

where:

$$\gamma = \frac{1}{\sqrt{1 - (\frac{v_{loc}}{c})^2}} = \frac{1}{\sqrt{1 - (\frac{1}{n^2})}} \tag{1.24}$$

v_{loc} is the local speed of light, m_0 is the rest mass of the primary particle in units of MeV and n is the refractive index at height h.

Using a value of n-1 = 4.13×10^6, the threshold energy for Cherenkov light production at an altitude of 30 km (sea level) for protons is ≈ 330 GeV (42 GeV) and for electrons is ≈ 178 MeV (21 MeV).

As the incoming charged particles have a speed faster than the speed of light in air, the photons initiated at the top of the atmosphere are the last to arrive at ground level. The DC opening angle,calculated from Equation 1.21, at a height of $\approx$ 30 km is 0.1° due to the low air density (Wakely 2007). This is much smaller than the average EAS emission angles of 0.4° and larger (Figure 1.6).

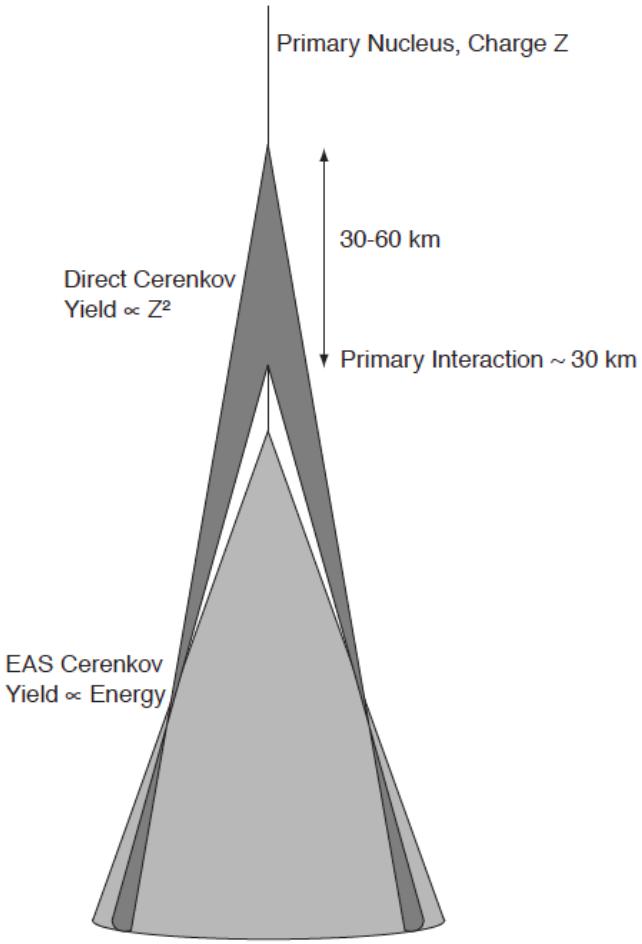

Figure 1.6: Illustration of the arrival direction of DC light compared to EAS light. Taken from (Kieda et al. 2001).

CHAPTER 2

The H.E.S.S. Experiment

Ground-based γ-ray astronomy uses the atmosphere as a medium to detect air showers from incoming Very High Energy (VHE) γ rays. The ground-based telescopes detecting light produced in these events are known as Imaging Atmospheric Cherenkov Telescopes (IACTs). They collect and image the Cherenkov light produced from the air shower cascades, described in Chapter 1. IACTs have a low energy threshold ($\approx$ 100 GeV) and a good separation of the hadronic background of CRs.

The production of air shower cascades as the result of VHE γ rays and CRs increase the detection area to $\approx 10^5$ m^2 for IACTs. Light from the air shower cascades is reflected off the IACT mirror and imaged by a camera sensitive to the the wavelength of Cherenkov light. These camera images are then used to reconstruct the air shower geometry. The H.E.S.S. experiment is an array of IACTs and its properties are described in this Chapter.

2.1 The H.E.S.S. Array

The High Energy Stereoscopic System (H.E.S.S.) is an array of five IACTs. The array detects γ rays in the multi-GeV and TeV energy regime and is located in the Khomas Highland of the Khomas region in Namibia. At 1800 m above sea level, the H.E.S.S. site provides very good observing conditions, with low humidity and the majority of observation nights being cloudless.

The array consists of two phases. They are H.E.S.S. I, which consists of the four smaller telescopes (CT1-4), and H.E.S.S. II, which includes all five IACTs (CT1-CT5). Phase I has been fully operational since 2003 while the larger, fifth telescope was inaugurated in

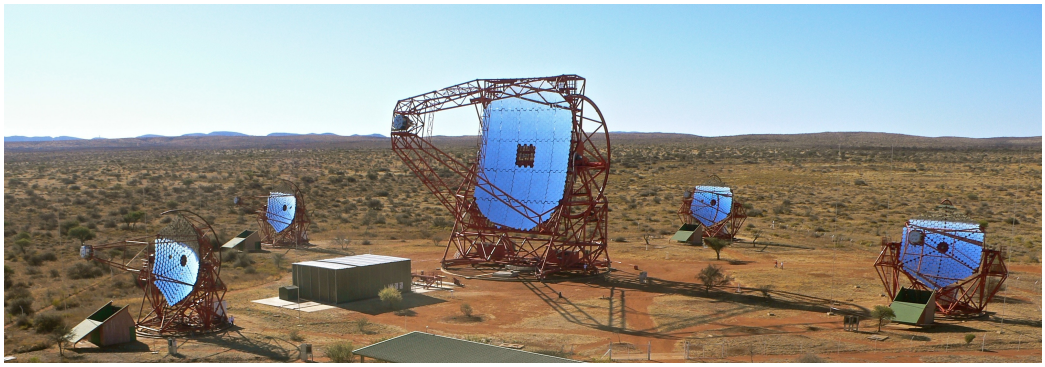

Figure 2.1: The High Energy Stereoscopic System (H.E.S.S.) located in Namibia.

2012. CT5 is capable making observations in a stereoscopic and individual mode, with the advantage of the individual mode being a lower energy threshold and image timing information.

The H.E.S.S. collaboration is a community of 170 scientists and 12 countries. The success of the H.E.S.S. experiment can partly be attributed to its wide field of view (FoV) of 5° and its location in the southern hemisphere. The wider FoV allows better detection of extended sources and the location of H.E.S.S. allows observations of the Galactic Centre.

2.1.1 Telescopes

The H.E.S.S. I telescopes are arranged in a square of 120 m side length. Although the diameter of typical Cherenkov light pool from a γ ray is $\approx$ 250 m, the telescopes are positioned closer to ensure that two or more telescopes are triggered from a VHE air shower.

The Cherenkov light is collected by the 382 mirror segments mounted onto each of the H.E.S.S. I telescopes. The mirror diameter is 12 m, with a total mirror area of 108 m^2. Light is focused at a distance of 15 m onto the camera. CT5 has a mirror diameter of 28 m, a factor of 2.5 times larger than CT1-4, with a total mirror area of 614 m^2. The corresponding focal length is 36 m.

The H.E.S.S. I cameras are designed to detect light at wavelengths larger than 330 nm. Each camera of CT1-4 consists of 960 photo multiplier tubes (PMTs). Each PMT covers an angle of 0.16° on the sky, giving a total FoV of 5°. CT5 has a total of 2048 PMTs, each covering an angle of 0.067°, giving a FoV of 3.2°.

2.1.2 Data Acquisition

Observations are taken during moonless hours or $dark\ time$ - after last moonlight and before first sunlight. Observations $runs$ are taken in periods of 28 minutes and are controlled by the data acquisition system (DAQ). Data is taken as the telescopes track a target on the sky with a position at $\geq 0.5^{\circ}$ offset from the source. This is to allow regions on and off the source to be positioned symmetrically with respect to the centre of the FoV. The runs are later analysed with one of two analysis chains: the H.E.S.S. Analysis Program or model++.

2.2 H.E.S.S. Analysis

Before the images are analysed with HAP, data is first selected, cleaned and calibrated. Events that are not fully contained in the camera are excluded by rejecting events with an image c.o.g. of more than 2° away from the centre of the camera. Additionally, events with an image amplitude of < 80 p.e. are discarded. These events have poor reconstruction accuracy and are excluded from further image analysis. For more information on the image cleaning procedure, see (Aharonian et al. 2006). For details on the calibration of H.E.S.S. data, refer to (Aharonian et al. 2004).

Data is processed with one of two analyses having different calibration chains and using separate Monte Carlo simulations: the H.E.S.S. Analysis Program (HAP) and model++ (de Naurois & Rolland 2009). The work discussed in this thesis was carried out with the HAP-HD analysis.

2.2.1 Reconstruction of Air Shower Parameters

The IACT technique utilizes a stereoscopic system to reconstruct the characteristics of the air shower such as the primary energy and direction.

As the geometry of air showers differ for different incoming particles, so does the topology of the images they produce in the camera. The Cherenkov light image is parameterized by a two-dimensional ellipse to determine the $Hillas\ Parameters$ (Hillas 1985). The Hillas Parameters (Figure 2.2) are useful in determining the initial conditions of the air shower. Six of the parameters are described below:

- **centre of gravity (c.o.g)**: the camera coordinates of the weighted mean signal of the image

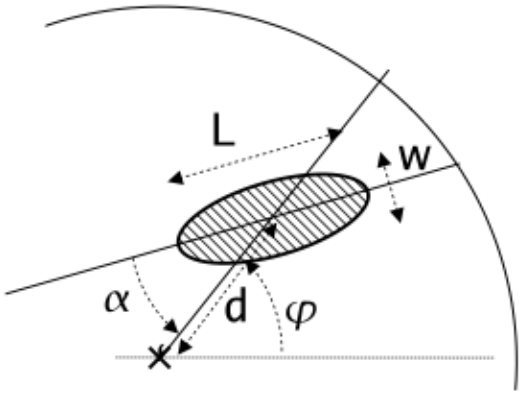

Figure 2.2: An illustration of the Hillas parameters used to describe an air shower. Taken from (de Naurois 2006).

- **length (L)**: RMS spread of intensity along the major axis of the ellipse
- **width (W)**: RMS spread of intensity along the minor axis of the ellipse
- **size**: total amplitude of the image
- **nominal distance (d)**: distance between c.o.g. and the centre of the camera
- **azimuthal angle (ϕ)**: angle between the camera axis and the line connecting the centre of the camera with the c.o.g.
- **orientation angle (α)**: angle between the major axis and the line connecting the centre of the camera with the c.o.g.

2.2.1.1 Energy and Direction

The arrival direction on the sky, also called the *source position*, can be reconstructed using the Hillas Parameters. The primary energy can also be estimated. Details are also discussed in (Aharonian et al. 2006).

The reconstruction of the source position is shown in Figure 2.3. The direction is estimated by finding the intersection points of the images major axes. A weighted average of the intersection positions are found, with each position weighted according to its image size and the intersection angle. Different approaches of the direction estimation is discussed in (Hofmann et al. 1999). The distance from the source position to the camera image is known as the *impact parameter*.

The primary energy of the air shower is estimated on the basis of image intensity. The energy is found with lookup tables generated from simulations by using two parameters, the

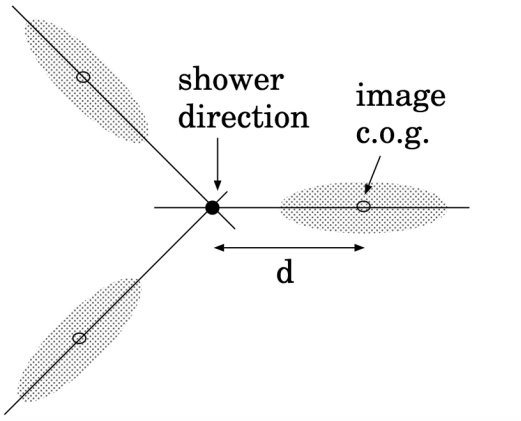

Figure 2.3: Illustration of the direction reconstruction using multiple images. Taken from (Hofmann et al. 1999).

impact parameter and the image size. The higher the telescope multiplicity of the event, the more accurate the estimation of the air shower characteristics.

2.2.1.2 Shower Maximum

Most of the Cherenkov light in an air shower is produced around the *shower maximum* (X_{max}). The different positioning of the telescopes relative to the shower axis can be used to determine the height of X_{max}.

The telescope locations can be described in 3 dimensions. The plane of the camera can be described as the xy plane and the axis of the telescope as z. Figure 2.4 illustrates the geometry of the air shower axis with respect to two telescopes. When the air shower cascade propagates towards ground level, the images produced in the camera will be shifted in the x direction by a distance L_m. Similarly, the images will be shifted in the z direction by the perpendicular distance of the telescopes, d_{12}. θ_x represents the shower axis orientation angle on the x axis and the height of X_{max} is represented by d.

The shift in the x direction is related to the orientation angle of the shower axis. As most of the camera image originates from light produced at d, the c.o.g. is used as the image reference. Subsequently, $y_{1,cog}$ and $y_{2,cog}$ can be calculated as:

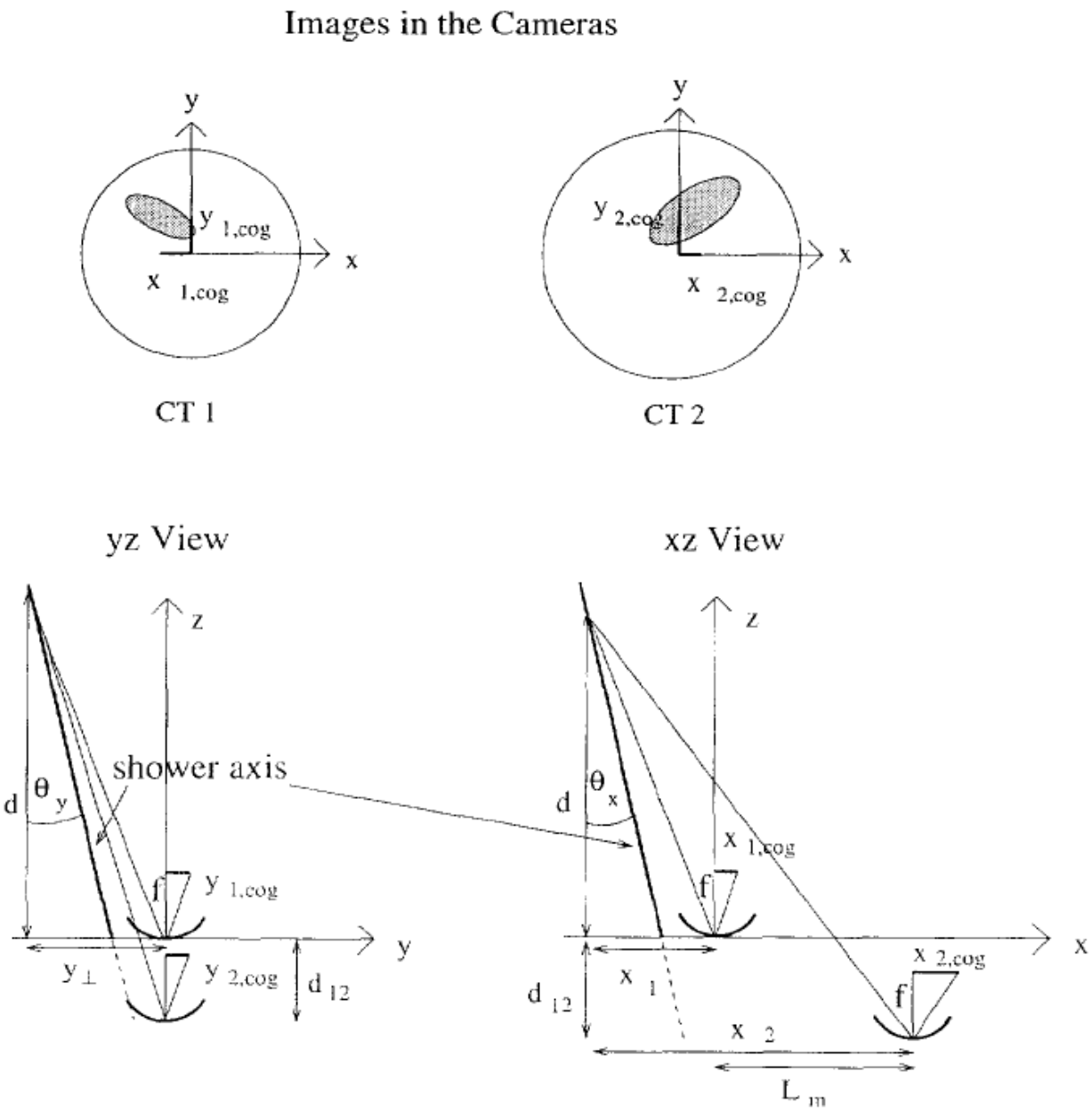

Figure 2.4: The orientation of the telescopes with respect to the axis of the air shower. The telescope location and shower position is described in one coordinate system to reconstruct the height of the shower maximum. Taken from (Kohnle et al. 1996).

$$\frac{y_{1,cog}}{f} = -\frac{y_{\perp}}{d} \tag{2.1}$$

$$\frac{y_{2,cog}}{f} = -\frac{y_{\perp}}{d + d_{12}} \tag{2.2}$$

where $y_{\perp}$ is the perpendicular distance of the telescope to X_{max} and f is the focal length. d_{12} is much smaller than d, therefore $y_{1,cog} \approx y_{2,cog}$. Similarly, the shift in the x direction can be calculated:

$$\frac{x_{1,cog}}{f} = -\frac{x_1}{d} \tag{2.3}$$

$$\frac{x_{2,cog}}{f} = -\frac{x_2}{d + d_{12}} = -\frac{x_1 - L_m}{d + d_{12}} \tag{2.4}$$

As $d_{12} \ll d$,

$$x_{2,cog} - x_{1,cog} = \frac{f L_m}{d} \tag{2.5}$$

From measuring the shift in the x direction of the stereoscopic images, the height of X_{max} (d) can be calculated from Equation 2.5. Due to variations in the lateral distribution of the Cherenkov light and misalignment of the image and shower axes, there is an uncertainty in the reconstructed X_{max}.

2.2.2 γ/Hadron Separation

The rate of background events is dominated by a hadronic origin with the rate of γ-ray events small compared to hadronic CRs. However, as described in Chapter 1, hadronic showers have a different shower development and therefore have images with very different features to electromagnetic ones.

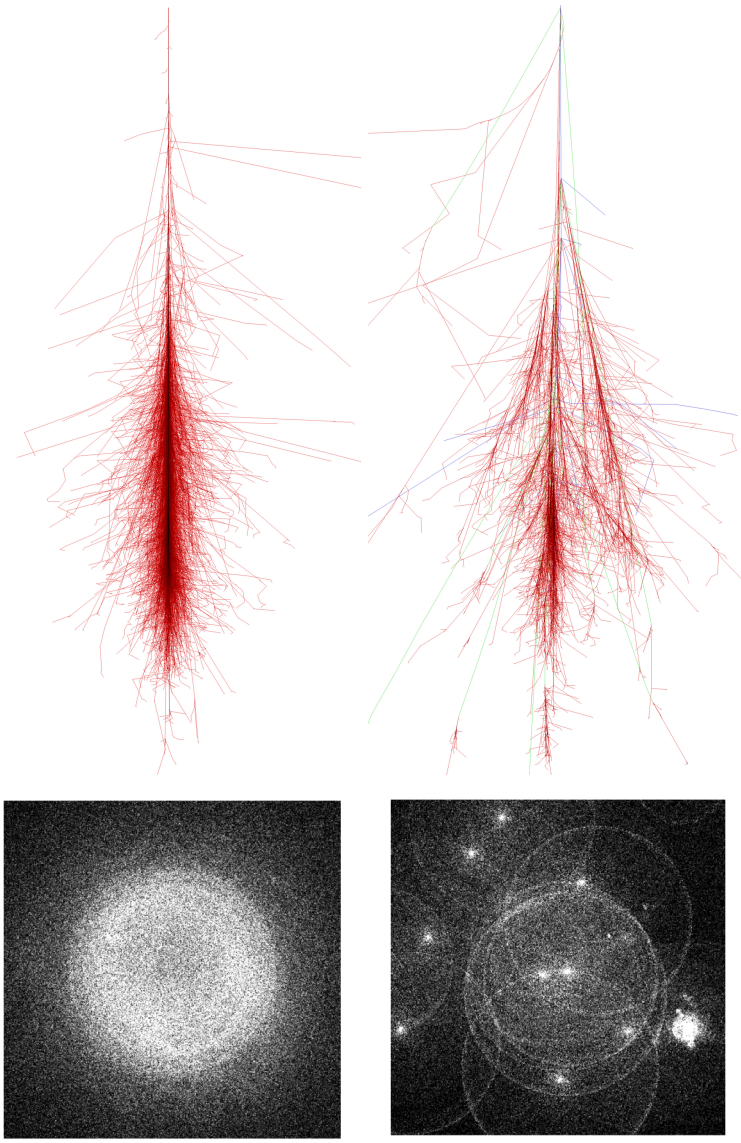

Figure 2.5: LEFT: An air shower initiated by a 100 GeV photon. The topology of EM cascade (top) produces homogeneous profile of Cherenkov light on the ground (bottom). RIGHT: The corresponding images for a 100 GeV proton shower. The cascade particles (top) travel far from the core and the lateral spread of light on the ground (bottom) is not uniform. Taken from (Schmidt & Knapp 2005) and (Berge 2002).

Hadronic showers have a larger lateral distribution when compared to EM showers (Figure 2.5). The strongly interacting particles travel far from the shower axis and a combination of both hadronic and EM sub-cascades are produced. The result is an uneven lateral spread of Cherenkov light. EM showers have a small lateral spread and particles interact close to the shower axis. Consequently, the EM images have a more smooth and symmetrical profile.

A successful approach in suppressing the hadronic background is *Scaled Cuts*. In this approach, the Hillas width and length of the image intensity profiles are compared to the expected mean and variance of EM air showers of the same impact parameter and image amplitude. The expected values are found from simulations and stored in lookup tables. The Scaled Width (SW) and Scaled Length (SL) of an image can then be determined (Fegan 1997):

$$SW = \frac{w(q,\rho) - < w(q,\rho) >}{\sigma_w(q,\rho)} \tag{2.6}$$

$$SL = \frac{l(q,\rho) - < l(q,\rho) >}{\sigma_l(q,\rho)} \tag{2.7}$$

where w is the Hillas width, l is the Hillas length, q is the image charge and ρ is the impact parameter. The Mean Scaled Reduced Width (MRSW) and Mean Scaled Reduced Length (MSRL) can then be determined:

$$MRSW = \frac{\sum_{i=1}^{n_{tel}} SW}{n_{tel}} \tag{2.8}$$

$$MRSL = \frac{\sum_{i=1}^{n_{tel}} SL}{n_{tel}} \tag{2.9}$$

where n_{tel} is the number of telescopes participating in the event reconstruction.

2.2.3 TMVA HAP

An increase the separation of γ-ray and hadron events is possible when additional parameters are combined with the Hillas Parameters (Ohm et al. 2009). The Toolkit for Multivariate Analysis (TMVA) package (Hoecker et al. 2007), implemented in the HAP framework, makes use of boosted decision trees to achieve a more sensitive analysis. The analysis will be referred to as TMVA HAP and the input parameters include:

- mean reduced scaled width / length (MRSW / MRSL)
- mean reduced scaled width / length off (MRSWO / MRSLO)
- depth of shower maximum (X_{max})
- spread in reconstructed energy (dE/E)

The MRSWO (MRSLO) is similarly defined to MRSW (MRSL) and compares the width (length) of the image to what is expected of a hadronic event. The parameter dE/E describes the average spread in the estimated energy, which is expected to be larger for hadronic events.

Chapter 3

Separation of Electrons, Protons and γ-ray Induced Air Showers

The term *direct Cherenkov* light has been traditionally used to describe light produced in the atmosphere as a direct result of the primary particles motion. In other words, all Cherenkov light that is given off before the first interaction of a charged particle entering the atmosphere. In this Chapter, the characteristics of direct Cherenkov light and its effect on the camera image for electron air showers are explored in Section 3.1. Another characteristic discussed is the shift in altitude in the air shower development between electron and γ-ray induced air showers (Section 3.1.2). In Section 3.2, a description of variables capable of separating γ rays, electrons and protons on a statistical basis is given.

3.1 Differences in EM Air Showers

Identifying the species of primary particle initiating an air shower relies on differences in their resulting Cherenkov emission profiles. As hadronic showers are much more diffuse than γ-ray ones, cuts on the shape of the Cherenkov emission imaged in the camera are sufficient in eliminating most of the hadronic background. After cuts are applied using the so called *standard zeta* cuts of TMVA HAP (Ohm et al. 2009) (Section 2.2.3), it is expected that the remaining electron and proton backgrounds become comparable.

Electron and γ-ray air showers involve the same interactions and the Cherenkov light produced in these showers is more compact with emission staying closer to the shower core when compared to hadrons (Chapter 1). The shape of the corresponding camera im-

age, parameterized by its mean scaled width and length, for both types of electromagnetic showers is practically indistinguishable. This implies that for electron and γ-ray events to be separated, new variables outside of shape cuts need to be established in order to successfully emphasize any differences.

As mentioned in Chapter 1, there are two important differences that impact the Cherenkov profile and shower development, one being the distance to the first interaction. On average, γ rays travel one radiation length, or 48 g/cm^2, before pair-producing in the VHE regime. In contrast to this, electrons interact almost immediately upon entering the atmosphere, forcing the air shower to start its development earlier (Figure 3.1).

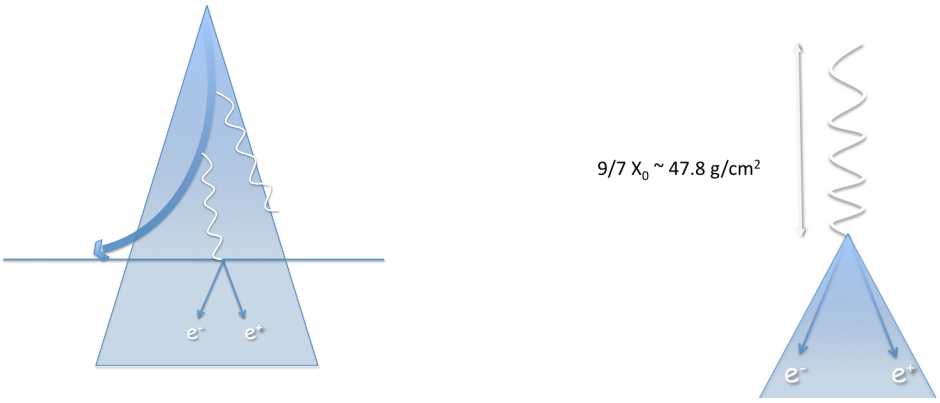

Figure 3.1: An illustration of the difference in the first interaction of electron and γ-ray induced air showers. LEFT: An electron enters the atmosphere and gives off bremsstrahlung photons, which travel further before pair producing and hence, starting the EAS development. The term *direct Cherenkov* (DC) is modified here to include all light given off above the horizontal line. RIGHT: The average first interaction of a γ-ray photon is $\approx$48 g/cm^2. An electron positron pair is produced and the shower starts to develop deeper into the atmosphere than it does for electrons. Note that this illustration is not to scale.

As the intensity profile of the camera images is of more interest than the shape, the difference in the first interaction is very important as it allows for different Cherenkov intensities to be detected at the head of the shower image. Furthermore, the difference in the distribution of the first interaction for both primary particles is of particular interest, giving an indication

of the feasibility of separating these events individually. This is discussed further in Section 3.1.1. An important point to note is that the Cherenkov intensity at the start of the shower is not only attributed to emission given off before the first interaction but rather, in the case of electrons, all emission given off before the first bremsstrahlung photon pair-produces. All Cherenkov light given off above this height contributes to an excess in intensity at the start of the image, known as *direct Cherenkov* (DC) light (see Section 1.3.2). This point in the air shower is illustrated in Figure 3.1.

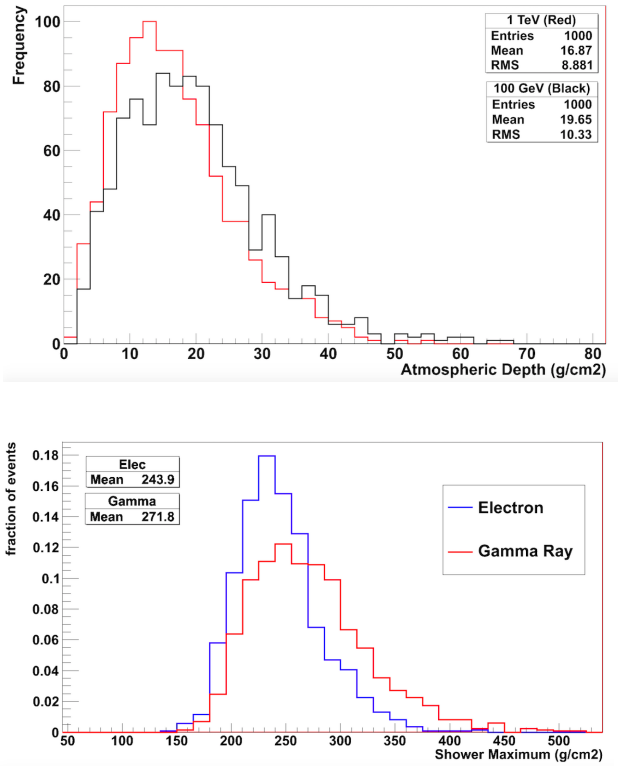

Figure 3.2: TOP: Height of first pair production in electron showers. The line in black represents 100 GeV electron shower events. The distribution of the first pair production in events with a true energy of 1 TeV is shown in red. BOTTOM: Height of the shower maximum of an electron air shower (blue) and γ-ray air shower (red), both having a simulated primary energy of 100 GeV.

Hence, for the purpose of this analysis, the more useful parameter to study is the height of the first pair production in electron showers rather than the first interaction itself. The air shower simulation program CORSIKA (Heck 1998) was used to probe this distance, which

is shown in Figure 3.2. The electron air showers are found to produce Cherenkov light over a distance of 20 g/cm^2 at 100 GeV before more Cherenkov light from secondary particles, known as extensive air shower (EAS) light, is given off. At 1 TeV this distance is 17 g/cm^2.

A second important parameter is the shower maximum, X_{max}. As mentioned in Section 1, most of the Cherenkov light and therefore camera image is produced at the point in the air shower where most of the particles are produced, known as X_{max}. The variation in the shower maximum of electron and γ-ray induced air showers is shown in Figure 3.2. According to Rossi (1952), the theoretical difference in X_{max} between an average electron and γ-ray air shower is half a radiation length (Chapter 1). However, this value is disputed as the Particle Data Group analysed data for elements ranging from carbon to uranium and measured a difference of one radiation length (Nakamura & Particle Data Group 2010). Using the air shower simulation package CORSIKA (Heck 1998), which simulates conditions of our atmosphere, the difference in X_{max} at 100 GeV is found to be 27.9 g/cm^2. This is $\frac{3}{4}$ of a radiation length or $0.75X_0$.

3.1.1 Direct Cherenkov Light

Direct Cherenkov light is an important characteristic of air showers and provides a unique opportunity to not only distinguish between charged and non-charged primaries, but also to identify the charge on the primary itself. As γ rays have no charge and travel much further before interacting, a deficit in the intensity of light is expected, with electrons and protons providing some intensity originating from the top of the atmosphere.

As mentioned earlier in this section, for the purpose of this study, the term *direct Cherenkov* is redefined here as all Cherenkov emission given off above the height of pair production of the first bremsstrahlung photon. This is the point in the shower at where the extensive air shower (EAS) begins and therefore, also the *EAS* light. This redefinition allows us to investigate the true difference in intensity at the start of the air shower of electron and γ-ray primaries.

An earlier study by Rolf Buehler (Aharonian et al. 2007) focussed on studying characteristics of direct Cherenkov emission from high energy, high charge cosmic rays. One of the applications of this study was to identify events based on the light yield found at the start of the shower image. Figure 3.3 shows a typical event that was studied, an iron event with a true energy of 58.3 TeV imaged in a CT5 camera. The higher the charge of the primary, the more recognizable the event as the light intensity yield of Cherenkov emission is propor-

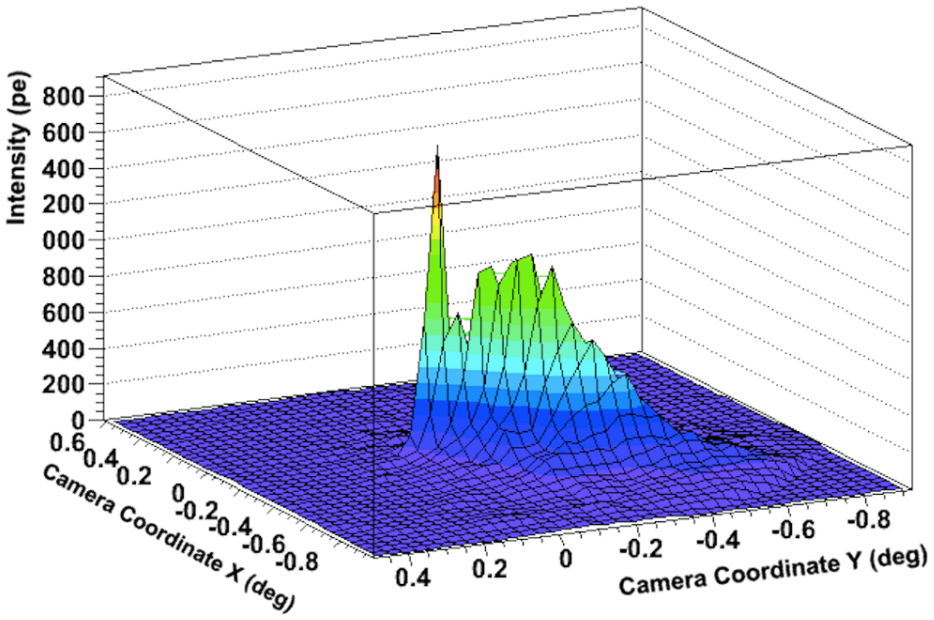

Figure 3.3: An iron event imaged in a CT5 camera with a simulated energy of 58.3 TeV. The intensity is shown as a function of the camera coordinates. The direct Cherenkov light is visible as a sharp peak at the head of the shower image.

tional to the charge of the primary squared (equation 1.22). These high charge events can be compared to superimposed proton showers, where the variations arising from emission produced far from the shower core average out and what is left is a smooth longitudinal profile with a sharp peak in intensity at the start of the image.

Electrons and protons do not produce as much direct Cherenkov light as nuclei as they have a charge of one (Kieda et al. 2001). For electron and proton air showers, the direct Cherenkov light is overwhelmed by the EAS light produced by secondary particles. Furthermore, the variation from one electron, γ-ray and proton air shower to another means that it would be hard to attribute any peak, or lack thereof, in intensity towards the shower direction as DC emission. Direct Cherenkov photons also have to travel further through the atmosphere, making them more likely to be absorbed. To qualitatively show this, an example of a 100 GeV electron shower and its corresponding DC light is shown in Figure 3.4.

The Cherenkov photons given off by the atmosphere from an electron primary were tracked using CORSIKA. Figure 3.4 shows the Cherenkov photons that came from a height

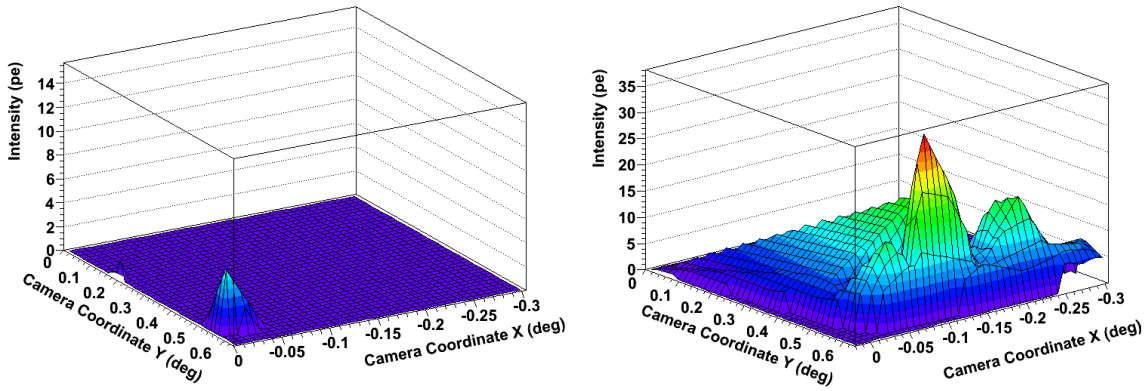

Figure 3.4: CT5 camera images of Cherenkov light produced in a single 100 GeV electron air shower at an impact parameter of 60 m. LEFT: All Cherenkov emission given off before the first bremsstrahlung photon pair produces, classified as the DC component. RIGHT: The fully contained electron shower image.

above the first pair production as well as the full camera image, with both the EAS and DC light fully contained.

The direct Cherenkov component of the shower is completely dominated by the EAS light of this event. Furthermore, this electron event is comparable to the H.E.S.S. lower energy threshold. If the DC component is not recognizable in a typical electron event at 100 GeV, then the DC component is also not strong enough to distinguish electron events at higher energies. As the energy of the primary increases, there is an increase in EAS light produced while the direct Cherenkov component remains almost constant (Section 1.3.1). Therefore, the EAS light has an even greater dominating effect at higher energies.

Due to the dominating wash out effect of the EAS light and the fact that any peaks at the start of the electron shower could be caused by variations of the shower profile, applying a similar analysis as Aharonian et al. (2007) would be very difficult indeed. Identifying on an event-by-event basis with current instrumentation would be extremely difficult, if even possible. Any new separation variables would have to focus on the differences between particle species over many showers, separating them on a statistical basis.

In Figure 3.5, the percentage of all simulated Monte Carlo events in which a H.E.S.S. II camera detected at least one DC photon is shown. Events in which one or more EAS photons were detected in the same pixel(s) is also shown. At 100 GeV and at 60 m impact

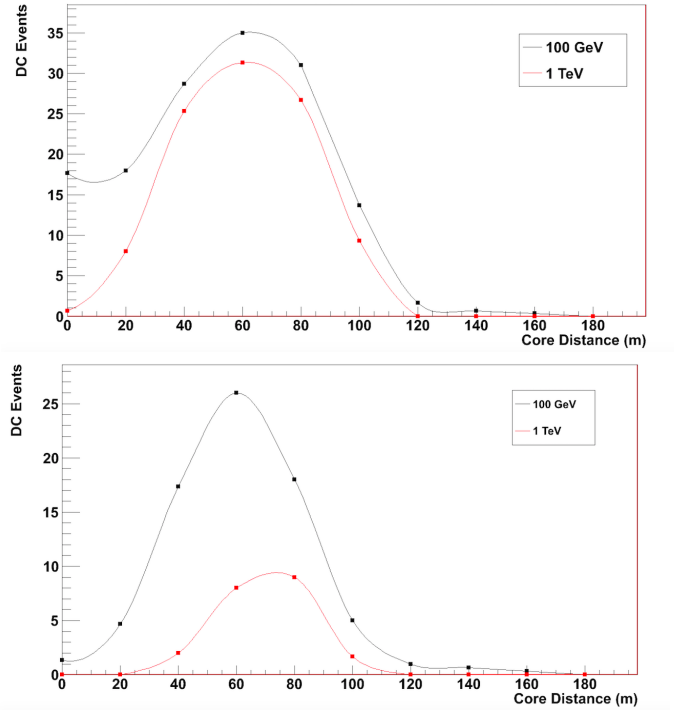

Figure 3.5: TOP: The percentage of electron air shower events with DC photons that are detected in a CT5 camera at different core distances from the array center. BOTTOM: Percentage of electron air shower events that have one or more pixels that detect only DC photons and no EAS photons.

parameter, 35% of events are found to contain DC light. At 1 TeV, the highest amount of DC light is again detected at 60 m impact distance, with slightly less events, 31%, having DC photons reaching the camera. Towards lower and higher impact parameters, this percentage falls. As the bremsstrahlung photons have an average pair production height that is higher in the atmosphere for 1 TeV events than for 100 GeV events (Figure 3.2), it follows naturally that less DC light will reach the camera at 1 TeV.

Figure 3.5 shows the percentage of electron events in which a H.E.S.S. I camera received *uncontaminated* DC photons. *Uncontaminated* in this context means an event in which at least one individual pixel detected only DC photons, with no EAS photons contaminating the DC signal. At 100 GeV, 25% of events were found to contain one or more pixels having only DC light at 60 m impact distance.

At 1 TeV, only 9% of events contain one or more DC pixels with no contamination from the EAS light. This is significantly lower than the 31% of all events having direct Cherenkov

detections, regardless of whether they were contaminated with EAS light or not. This is due to the much higher amount of EAS Cherenkov photons at higher energies washing out the DC signal. Even though over a third of electron events have DC photons that reach ground level and is eventually detected in a H.E.S.S. I camera, most of this light is overshadowed by the EAS light, with the effect more pronounced at higher energies.

An interesting feature is that the impact parameter at which most pixels detect DC light at 1 TeV is shifted towards 70 m, compared with 60 m shown in Figure 3.5. This is most likely because larger impact distances have an EAS camera image that is shifted further away from the source position, allowing the DC light at the head of the image to emerge. Due to the opening angle of Cherenkov light at the top of the atmosphere and the low refractive index, there is only a small range in which to view the DC light. As shown in Figure 3.5, hardly any DC light is imaged past 100 m.

3.1.2 Shifting of Camera Image

Another important parameter that was studied is the Shower Maximum, X_{max}. As discussed in Chapter 1, the earlier shower development of electron initiated air showers results in the shower maximum occurring higher in the atmosphere for primary electrons than it does for γ rays. As the entire air shower is shifted higher in the atmosphere, the light imaged in the camera starts closer to the source position, with the electron image being *shifted* towards the shower direction.

This study focussed on two differences in the air shower development between different particle species: the first interaction (X_0) and the shower maximum (X_{max}). In the last section the DC component, which is influenced by X_0, was studied. In this section, the differences in the shower image itself is studied. This differences found in the camera image is influenced by both the shifting of the EAS image from differences in X_{max} as well as by the existence of DC light before the air shower develops. These properties are not disentangled here, but rather their combined influence is discussed.

Using ImPACT (Parsons & Hinton 2014), a template style analysis, electron and γ-ray images were averaged over many thousands of events. As the intrinsic properties of the images were important at first, a telescope with 100% optical efficiency was assumed. All events were produced at zenith with a simulated energy of 200 GeV and at an impact parameter of 60 m. The corresponding averaged electron and γ-ray images are shown in Figure 3.6.

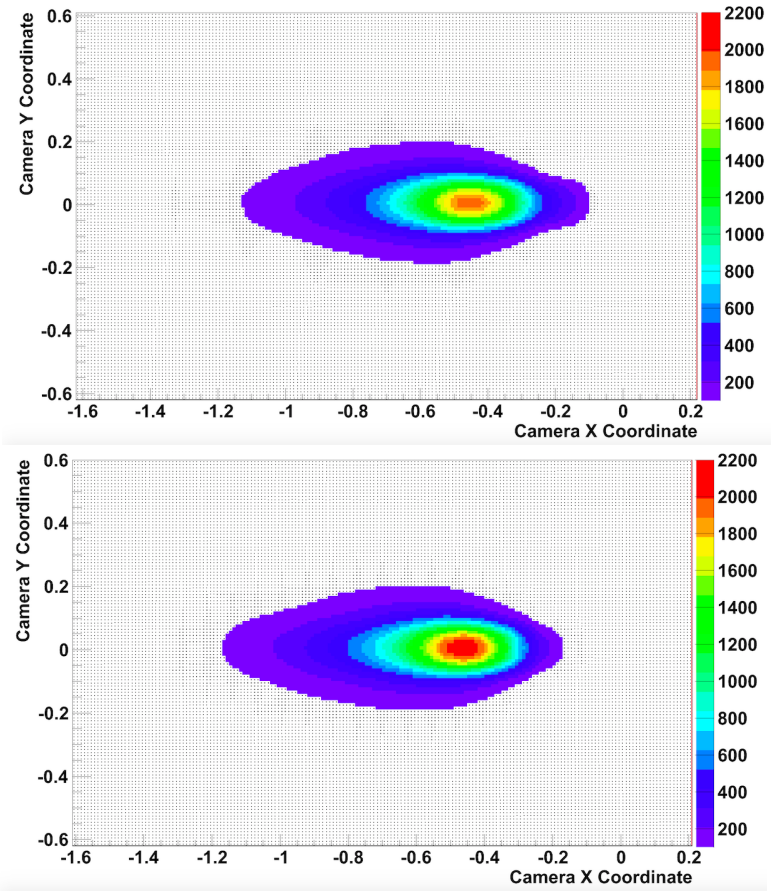

Figure 3.6: Averaged camera images for electron air showers (TOP) and γ-ray air showers (BOTTOM) with a simulated energy of 200 GeV. All air showers were produced at zenith with a simulated source position at the center of the camera and at 60 m impact parameter.

Qualitatively, it can be seen that the electron image has a higher intensity towards the source position at (0,0). Moreover, the shape of this excess intensity is not continuous with the main EAS component, showing a distinct change in the expansion of the width of the image. This feature is not noticeable in the averaged γ-ray image, where a continuous, smooth widening is seen.

The difference in intensity between the two images is clearly shown in Figure 3.7, where the averaged γ-ray image is subtracted from the electron one. An excess in intensity at the start of the image as well as a deficit at the tail is found. This deficit suggests that the c.o.g. of the EAS image is shifted further away from the source position for γ rays than it is for electrons, which is expected due to its later shower development. The excess found at the

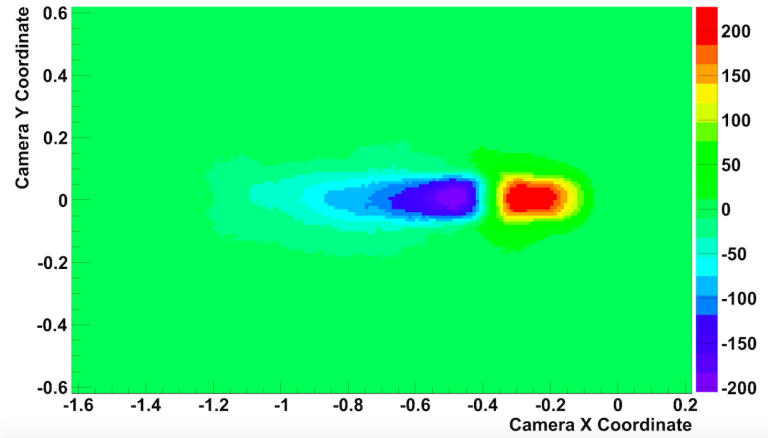

Figure 3.7: A histogram of the averaged γ-ray image subtracted from the averaged electron image at a simulated energy of 200 GeV. An excess in intensity, shown in red, is found close to the camera center whereas a deficit, shown in blue, is found at the tail of the image.

head of the shower could be due to a combination of the image shift as well as DC light.

Figure 3.8 shows the ratio of intensity of the averaged electron image to the γ-ray one. The average of 200 GeV electron showers at three different impact parameters were divided by the same corresponding γ-ray images. These were generated using ImPACT and assume a perfect camera at 100% optical efficiency with both types of showers generated using the same true energy.

The largest difference in the excess at the head of the image is found at 60 m impact parameter, with approximately two times as much intensity recorded for electrons over two pixel lengths. At 40 m and 80 m impact distance, the ratio of intensity decreases. This corresponds with the results shown in Figure 3.5 in which most of the DC photons that were detected were at an impact distance of 60 m.

There is a clear difference between γ-ray and electron shower images, which is noticeable in a CT5 camera. The next step was to find out how best to utilize these differences in order to provide some separation power between the two types of EM events. Another question is whether the same techniques used to separate electron and γ-ray air showers could also be used in identifying proton air showers, as they also contain DC light and have

an even later shower development.

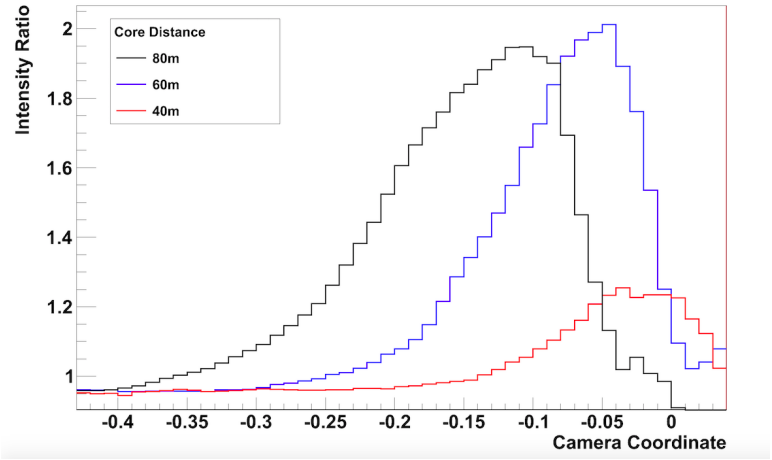

Figure 3.8: The profile of the averaged electron image divided by the averaged γ-ray one at 200 GeV, taken along one coordinate. This ratio was taken at 40 m (red), 60 m (blue) and 80 m (black).

3.2 Variables for Shower Characterization

Three sets of separators were developed to identify events as having either an electron, proton or γ-ray origin. They are: Image Slices, Quantiles and Ratios. All sets of variables contribute to identifying EM showers from proton induced ones, as well as the type of EM shower. The variables were assessed using H.E.S.S. I telescopes in the phase1b configuration.

When cleaning the images, pixels that pass certain criteria are kept. In this case, pixels that detect a minimum of 7 pe and have a neighbouring pixel of at least 4 pe survive the criteria (so called *extended images*). Similarly, pixels having an amplitude of at least 4 pe and a neighbouring pixel of 7 pe or more are included.

3.2.1 Image Slices

Both the direct Cherenkov emission and the shifting of the camera image alters the Cherenkov emission profile of the shower. This changes the variation in intensity of the image as a function of distance from the shower origin. The first set of variables, or *Image Slices*, is illustrated in Figure 3.9.

The image is divided radially into multiple slices, with the first slice starting from the reconstructed source position. For simplicity, the slices are drawn linearly. Each slice has a width of a pixel length. In the case of the H.E.S.S. I telescopes, this is 0.16°. If the centre of a pixel falls within each slice of the image, its intensity is added to the total intensity of the slice. The intensity of eleven image slices are found and therefore a set of 11 variables are used to discriminate.

Figure 3.9: An illustration of the first set if separation variables, or *Image Slices*. LEFT: A depiction of where the DC light should arrive in relation to the EAS emission of the shower. RIGHT: How the image is sliced. The slices have a length of one pixel length and are in fact radially divided. In the case of CT5, each pixel has a length of 0.08°.

It is important to note here, that the first image slice should be taken from the reconstructed source position and not where the amplitude of the image is above zero. This is an important point if the geometry and intensity of the Cherenkov emission is to be compared correctly.

The absolute values for this set of variables are shown in Figure 3.10. The variables can be mean scaled, analogous to MRSW and MRSL described in Section 2.2.2. Simulations were used to create lookup tables that stores the mean and σ values for the corresponding energy and impact parameter. The mean scaled values of events with a telescope

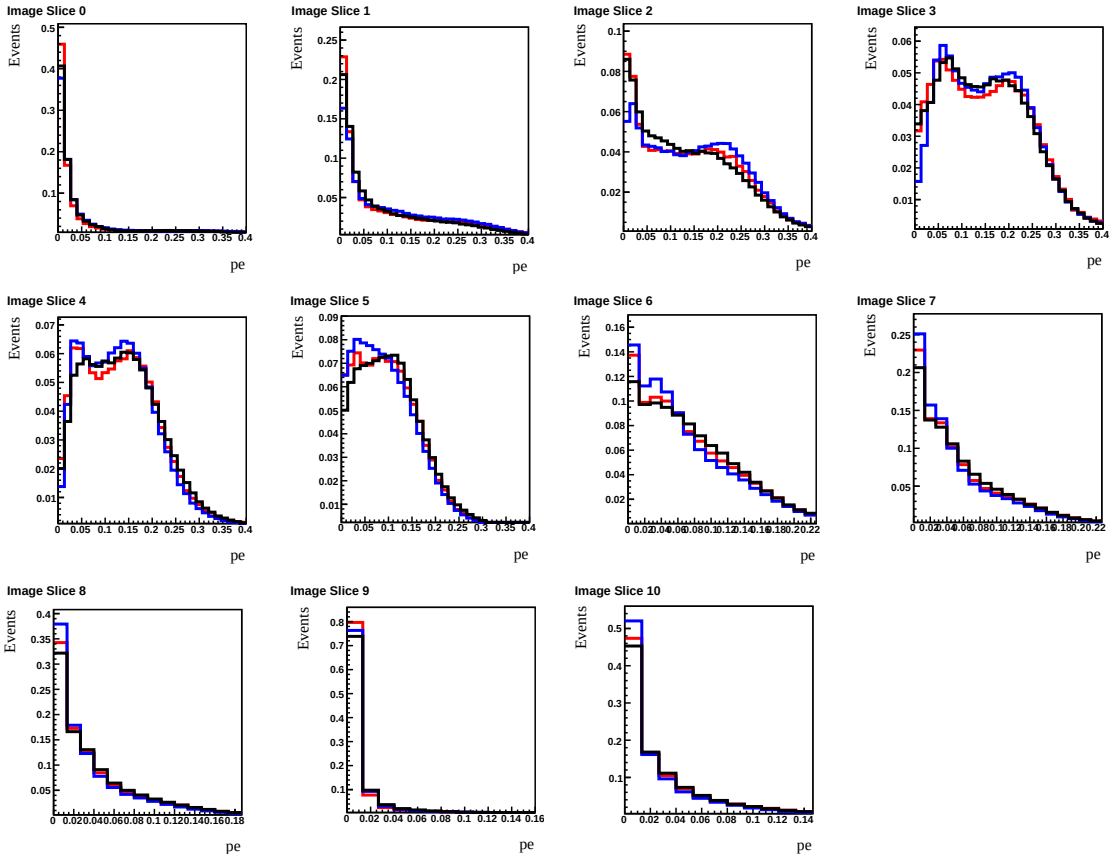

Figure 3.10: The absolute values of the Image Slice separation variables. The histogram title represents the position of the slice from the source position, the higher the number the further away the slice from the source position. The intensity of the image slice over many events in photoelectrons (pe) is shown against the fraction of events. γ rays are shown in red, electrons in blue and protons in black.

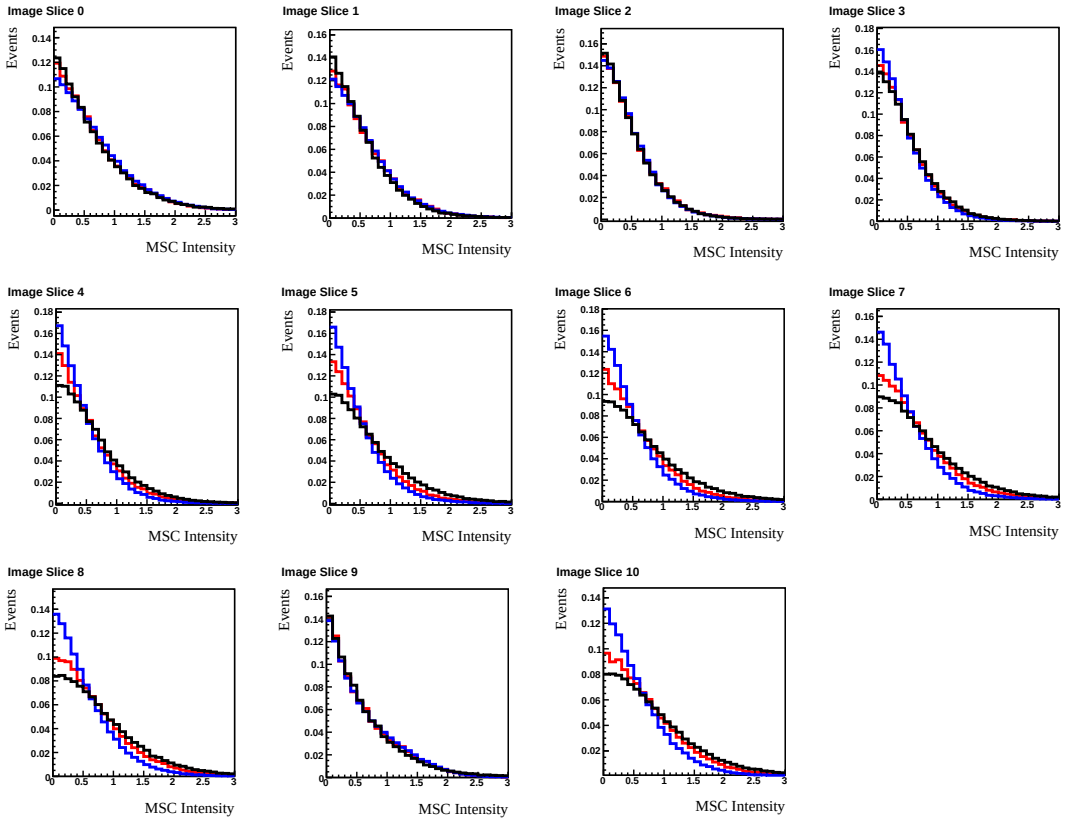

Figure 3.11: The mean scaled values of the Image Slice discriminators. Electrons are shown in blue, γ rays in red and protons in black. The discriminator name (shown as the histogram title) denotes the image slice position. *Image Slice 0* is the first slice starting from the reconstructed source position. The mean scaled intensity of the image slice is shown against the fraction of events.

multiplicity of four, a reconstructed energy between 380 and 900 GeV and an impact parameter of less than 280 m are shown in Figure 3.11. The last image slice is taken at 1.6° to 1.76° from the camera center.

γ rays are found to have the lowest intensities in the first few slices, as their images are shifted further away from the reconstructed source position. Even though protons have the same charge and hence produce the same amount of DC light as electrons, they too have a larger first interaction depth than EM air showers and therefore a later shower development. This means that although DC light is detected early, EAS light from proton induced air showers is first detected further from the camera center than for primary electrons or γ rays. Additionally, the reconstructed source position of protons is more inaccurate, resulting in a proportion of images being integrated along the wrong direction.

3.2.2 Quantiles

Another set of variables making use of the increased intensities due to DC light and the shifting in the camera image is $Quantiles$. The Quantile variables provide another way of distinguishing different types of events by finding the distance from the camera centre to a certain proportion of the image amplitude.

In the case of the Image Slices, the pixel centres are taken as the location of the pixel. In reality, the photon could arrive anywhere within 0.16° of each pixel center. As radial slices cut across pixels, this contributes to the incorrect assigning of a pixel intensity to the wrong image slice. The Quantile variables reduce this noise factor, rather giving the distance along the image that 10%, 20% and every additional 10% of the integrated intensity is found. Though, in practice, it is the inverse cumulative distribution function (CDF) of the image amplitude that is taken, rather than the amplitude itself.

In order to have the images correspond to each other, they are translated so that the source position lies at the center of the camera as shown in Figure 3.12. The images are then rotated so that the major axis falls along the same camera coordinates. This rotation is not necessary in the case of Image Slice discriminators as a reference of the major axes of each image is not needed.

As γ-ray initiated air showers start their development deeper into the atmosphere, the first EAS light imaged lies farther from the camera center than for electron induced air showers. The Quantile length along the major axis of the image will be largest for electrons.

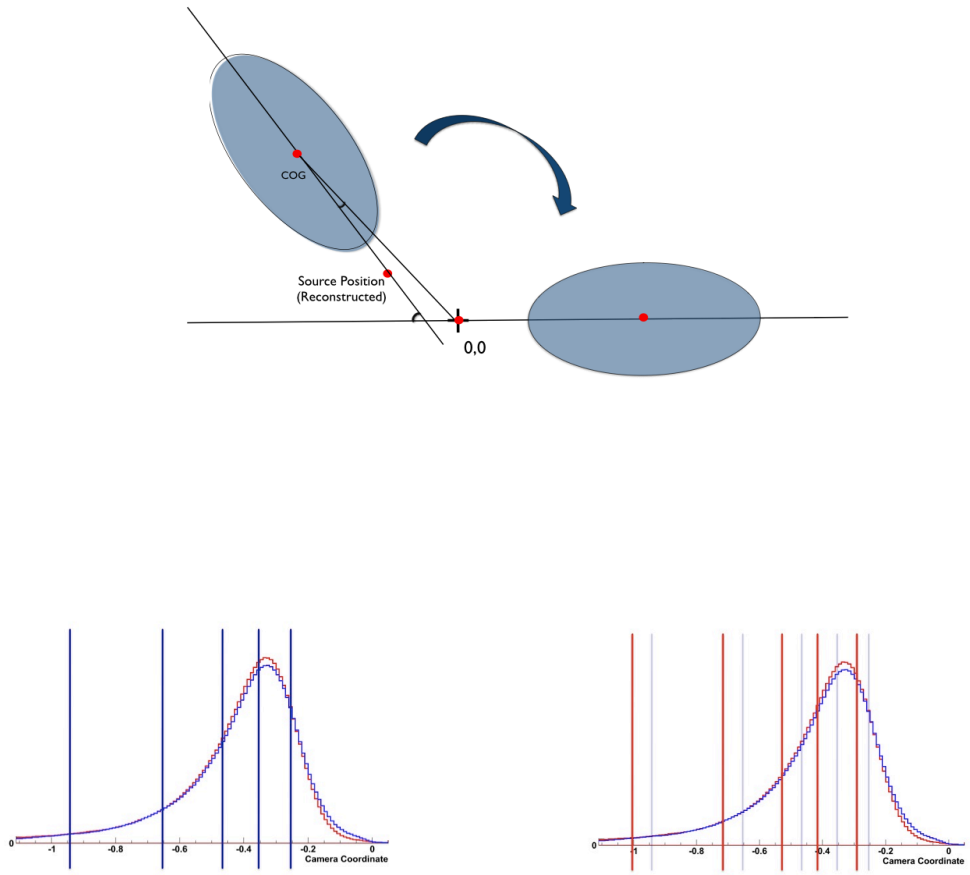

Figure 3.12: The Quantile variables are depicted here. TOP: The reconstructed source position of all camera images is first translated to coordinates 0,0 and rotated so that the Quantile values are correctly compared. BOTTOM: Longitudinal profiles of electron images (blue) and γ-ray images (red). The lines compare the Quantile variables found from these profiles for electrons and γ rays.

The values for nine quantiles, 10% to 90%, are used as the second set of separation variables. Figure 3.14 shows the mean scaled values (discussed in Section 3.2.1) of these nine Quantile variables. The absolute values are shown in Figure 3.13. The γ-ray and proton variables have similar distributions, while the electrons have lower values on average.

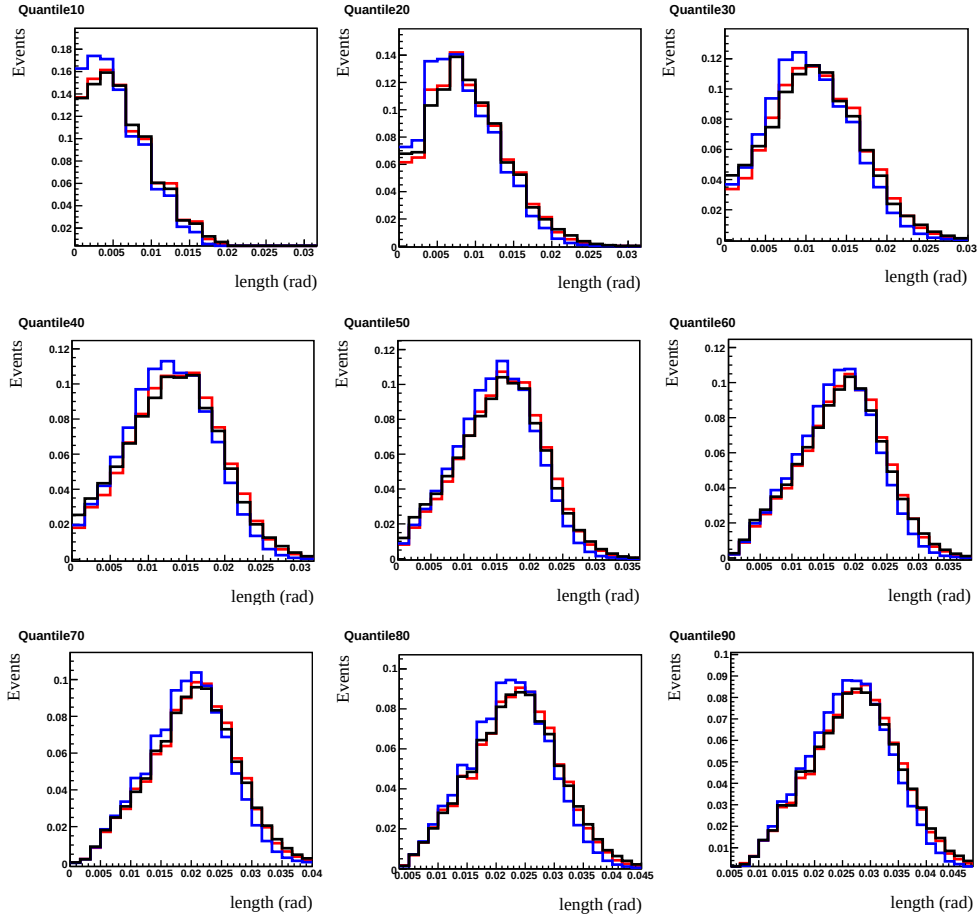

Figure 3.13: The absolute values of the Quantile variables. The histogram title represents the percentage of amplitude used to calculate the discriminator. The x-axis value shows the discriminator length in radians. The y-axis shows the fraction of events. Electrons are shown in blue, γ rays in red and protons in black.

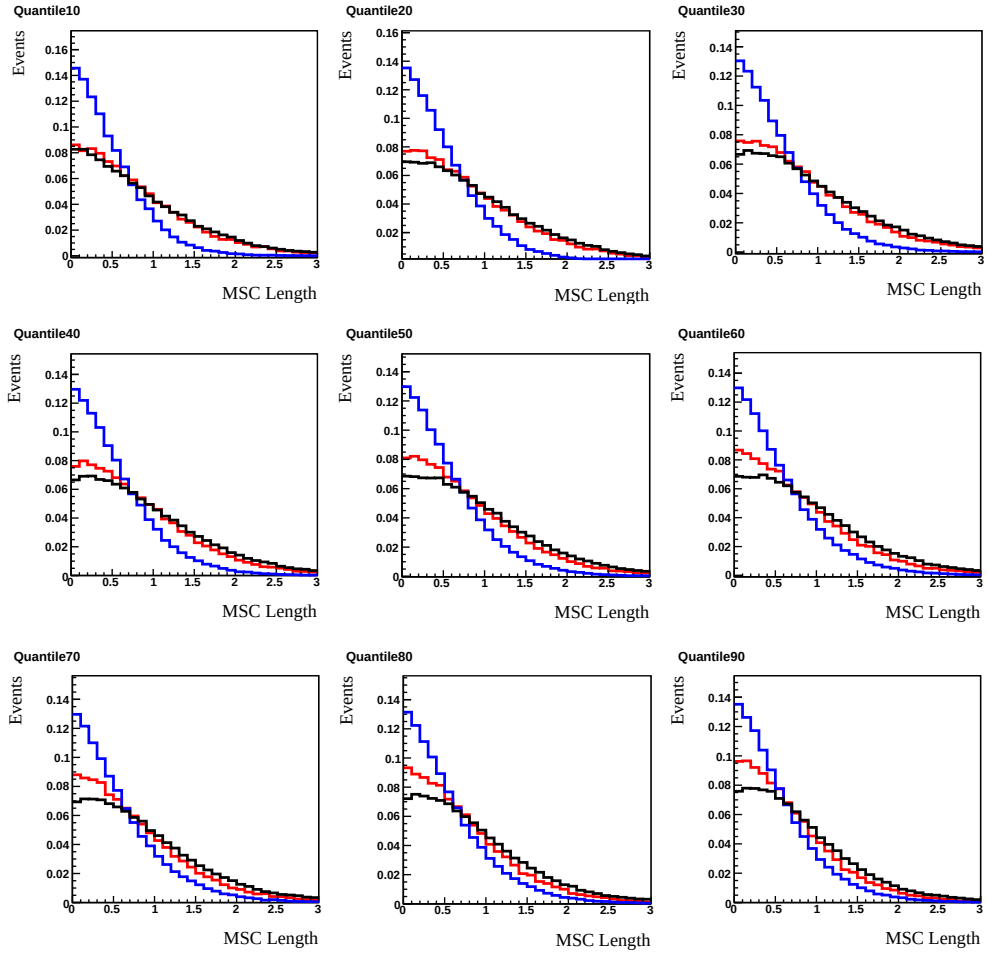

Figure 3.14: The mean scaled values for the Quantile variables. Electrons are shown in blue, γ rays in red and protons in black. The title shows the discriminator name, which represents the percentage of amplitude used to find the variables. The x-axis shows the mean scaled length along the camera and the y-axis the fraction of events.

3.2.3 Ratios

The third method finds the ratio of intensity of the start of the image to the remaining amplitude. Six distances are defined, whereby the total amplitude found at smaller distances to the source position is divided by the total amplitude found after it. This is to maximise the difference in intensity found at the head of the image. This method is illustrated in Figure 3.15. The longitudinal profiles of γ rays and electrons differ slightly, with an excess in intensity at the start of the image in the electron profile. This is absent in the γ-ray shower profile due to a lack of DC light at the start of the shower.

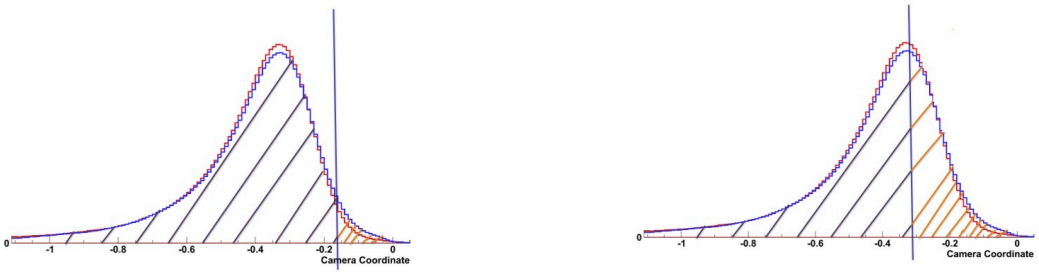

Figure 3.15: The Ratio variables are found from dividing the head of the image (orange) by the remaining image (blue). For each variable, a distance was chosen (blue line) that divided the the image into two amplitudes.

The variable name denotes the position at which the starting intensity (I_1) and the remaining intensity (I_2) were defined. The lower the variable number, the smaller the defining distance and the greater the difference between I_1 and I_2.

Figure 3.17 shows the six mean scaled Ratio separation variables. The Ratio variables for all three types of particles - electrons, protons and γ rays - have very similar distributions when compared to the other separators. Hence, this set of variables provides the least separation. However, extending this set of variables to further distances may provide better classification power. The absolute values before mean scaling can be seen in Figure 3.16.

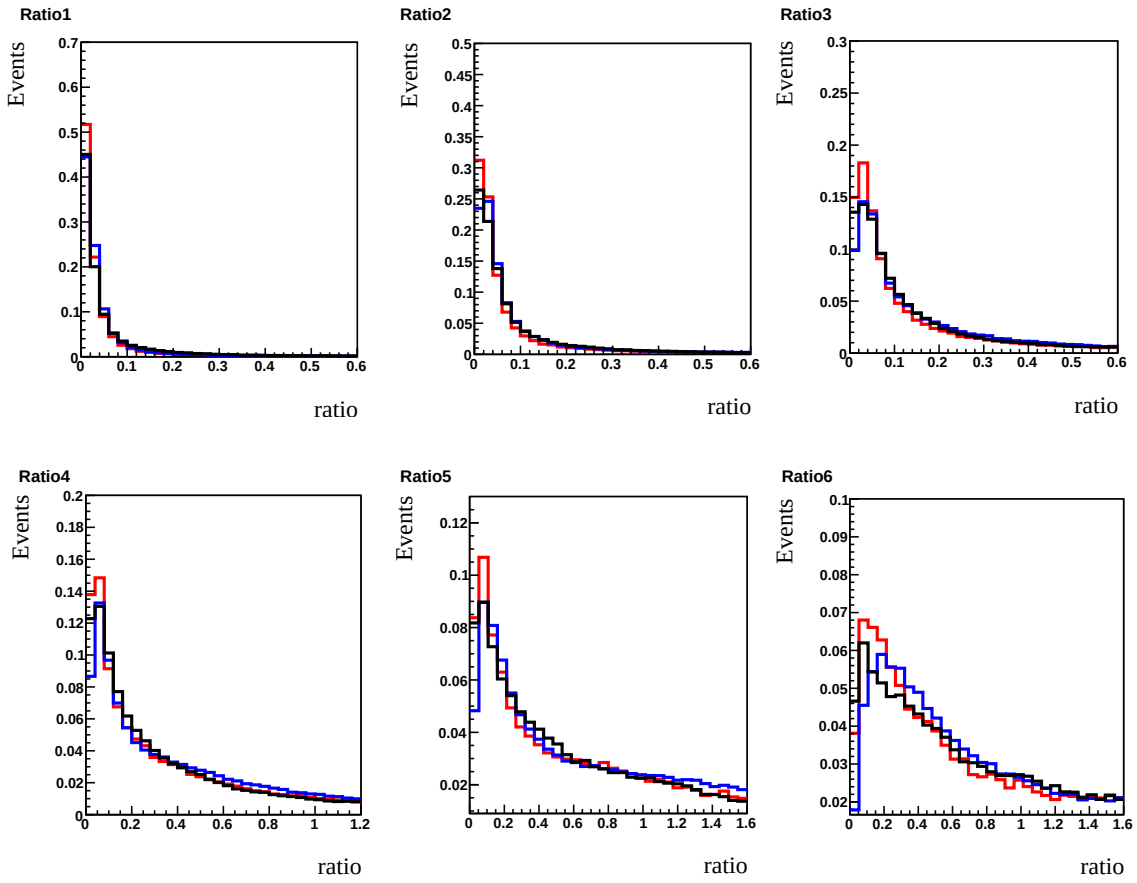

Figure 3.16: The absolute values of the Ratio discriminators. The title denotes the position at which I_1 and I_2 is defined. The x-axis shows the ratio between the two amplitudes, I_1/I_2. The y-axis shows the fraction of events. Electrons are shown in blue, γ rays in red and protons in black.

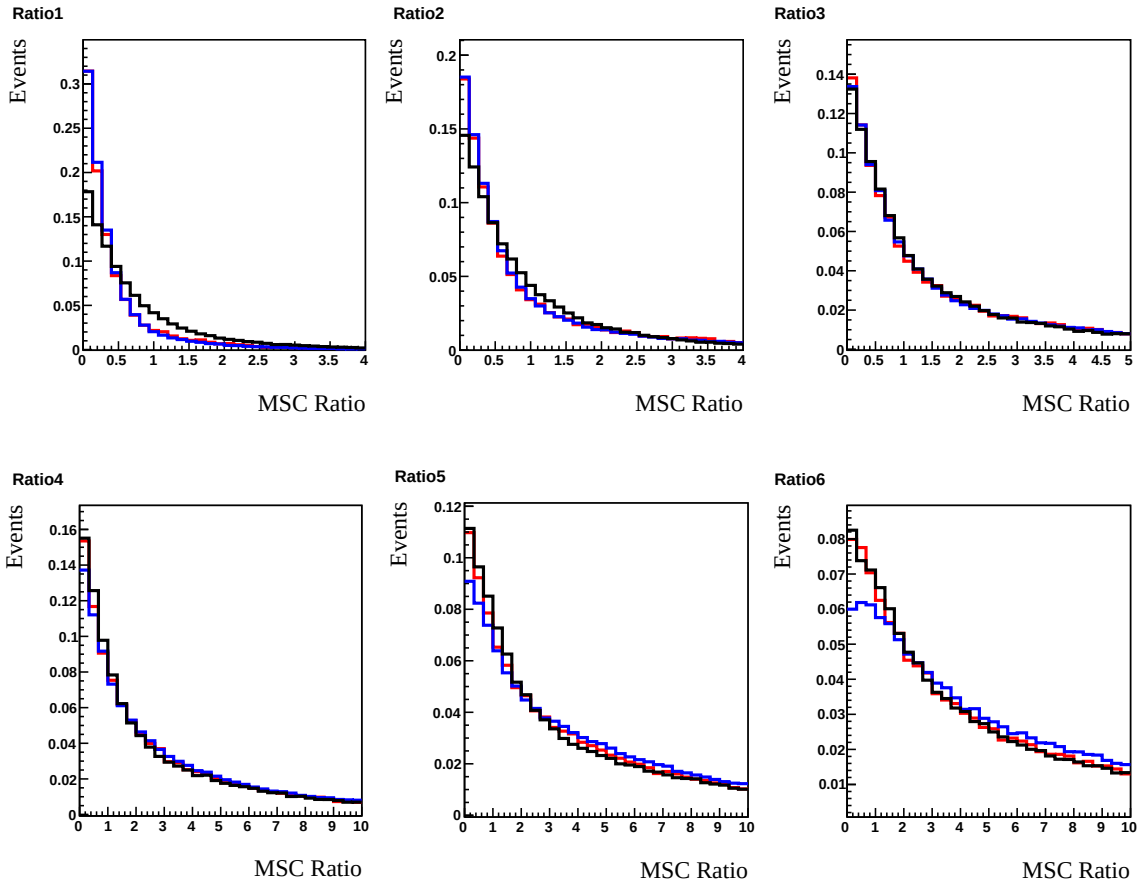

Figure 3.17: Mean scaled values of the set of Ratio separation variables. Six variables were used, with different distances dividing the amplitude of the image into two. The mean scaled values of the ratio of these two amplitudes are shown here. The values found for γ-ray air showers are shown in red, electron showers in blue and proton showers in black.

3.3 Conclusion

Characteristics of DC light have been studied in this Chapter and its effect on the camera image identified. Two differences in the air shower development of electrons and γ rays were discussed. These were the height of the shower maximum (X_{max}) and direct Cherenkov (DC) light.

The higher shower development of electron cascades compared to γ ray air showers was confirmed, with a difference in X_{max} of 27.9 g/cm^2. The characteristics of DC light in electron air showers was also explored. Traditionally, DC light has been defined as light produced above the first interaction. However, when looking for unique signatures in camera images, it is the light that can be identified as being separate from the EAS air shower that is important. Therefore, DC light of an electron shower was redefined as Cherenkov light produced in the atmosphere above the height of the first pair production of a bremsstrahlung photon.

It was found that a maximum number of DC photons are detected at an impact parameter of 60 m. DC photons are detected in the camera for 35% of events at 100 GeV. This decreases at 1 TeV to 31%. At 100 GeV, the DC light is not overwhelmed by light from the EAS shower, though at 1 TeV it is.

Three sets of variables related to the intensity profile of the shower image were defined as variables capable of separating γ rays, electrons and protons on a statistical basis. They are *Image Slices*, *Quantiles* and *Ratios*.

Chapter 4

Analysis and Fitting of Electron, Proton and γ-ray Components

Although a lot of effort has already been focussed on improving γ-ray identification, distinguishing between different types of incoming particles other than γ rays also has its benefits. Having a multi-component classification rather than suppressing and discarding a general background of events allows measurements of different signals to be carried out. Studies using Monte Carlo simulations suggest that the only types of events passing the most sensitive cuts currently in place are protons, electrons and γ rays with the total contribution from nuclei essentially rejected.

Currently, no analysis in the HAP chain exists to suppress the electron background with the only known identifier previous to this study being X_{max}. X_{max} is already used as a separator when evaluating each event with TMVA HAP (Ohm et al. 2009), though the suppression of the electron background is hardly effected when compared to using another cut set.

Fitting three components simultaneously and identifying the contribution of γ rays in a data sample as well as the contribution of electrons and protons not only allows a better estimate of the γ-ray flux observed, but a better estimate of the electron and proton flux in the *same* data sample. The same sample is an important point because it eliminates the need to have a background region as a reference. As discussed in the introduction, this has significant benefits and provides a new way of making interesting measurements.

The analysis assigns a value describing the probability of a single event belonging to either a γ-ray, electron or proton air shower. Ultimately, depending on the study, the analysis

could be used in two ways: to suppress the two remaining background components by making a cut at a certain classifier value or to fit the entire data set and find the composition of each particle species.

For the analysis to be as accurate as possible, it is crucial to reduce the high proton flux to a point that is comparable with the number of γ rays found in the data. For this reason, a selection of events is first made with TMVA HAP.

Lookup tables were generated for each separator using electron simulations and used to find the corresponding mean scaled value of each event. It should be noted that the scope of this thesis applies to H.E.S.S. I data and therefore only analyses involving the H.E.S.S. I telescopes are discussed. The following chapter outlines the steps taken in the analysis and uses the well studied extragalactic BL Lac PKS 2155-304 to test its performance.

4.1 Three-Component Separation

The sets of multivariates discussed in Chapter 3, namely Image Slices, Quantiles and Ratios, were then fed into a multivariate analysis that uses a large sample of simulated events to evaluate an individual event. The best separation variable and cut value with the most separating power is determined by TMVA (Ohm et al. 2009) and splits the Monte Carlo sample into signal and background. This cycle continues with the next best variable and cut value then chosen until a minimum number of events is reached. A classifying value is assigned to each event, representing the likeliness of it being either a proton, electron or γ-ray event.

This was done for three different decision trees. The first tree was given electrons as the signal and γ rays as the background **(EG classifier)**, the second tree used protons as the signal and electrons as the background **(PE classifier)** and the third used γ rays as the signal and protons as the background **(GP classifier)**. Figure 4.1 shows the distribution of these three classifiers for each primary particle.

An upper energy threshold of 900 GeV was chosen. This simplifies the weighting process as the electron spectrum is expected to turnover at $\approx$ 1 TeV. After making an initial cut on the source position, image amplitude and the standard zeta classifier, events having an energy between 380 to 900 GeV and an impact parameter of up to 280 m were kept. Only events in which all four H.E.S.S. I telescopes participated were chosen.

Figure 4.2 shows how the γ-ray efficiency scales for each particle and classifier, reflect-

ing the amount of electron or proton background that can be rejected after making a cut on the 1D distributions. Making a cut on the first distribution gives the best separation between electrons and γ rays, as one would expect, since TMVA was used to specifically find differences between these two species. Similarly, the best proton rejection comes from the third distribution.

An electron rejection power of 37% is achieved while keeping 80% of the γ-ray signal. In addition, 65% of proton events are rejected while 85% of the γ-ray signal remains. The rejection power stated here applies to all events that are currently accepted as γ-ray events after selection with the standard TMVA HAP analysis, showing that a more sensitive cut and better background suppression can be applied to the most γ-like events with this method.

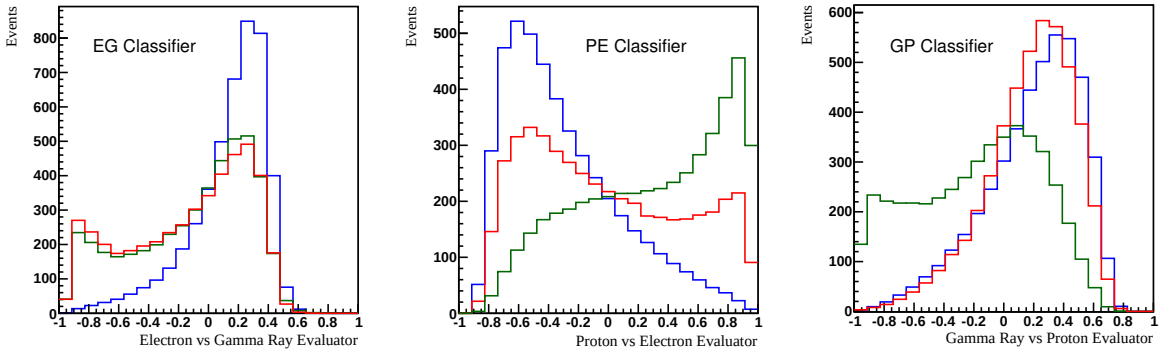

Figure 4.1: Evaluator values of each event found from training three decision trees with TMVA. Events with a telescope multiplicity of 4, a reconstructed energy of 380 to 900 GeV and an impact parameter of less than 280 m are included. Only the H.E.S.S. I telescopes are considered. LEFT: values for each event obtained when training electrons against γ rays. CENTRE: classifier values from training protons against electrons. RIGHT: classifier values for each event found from training γ rays as signal and protons as background. Red represents γ rays, blue electrons and green protons.

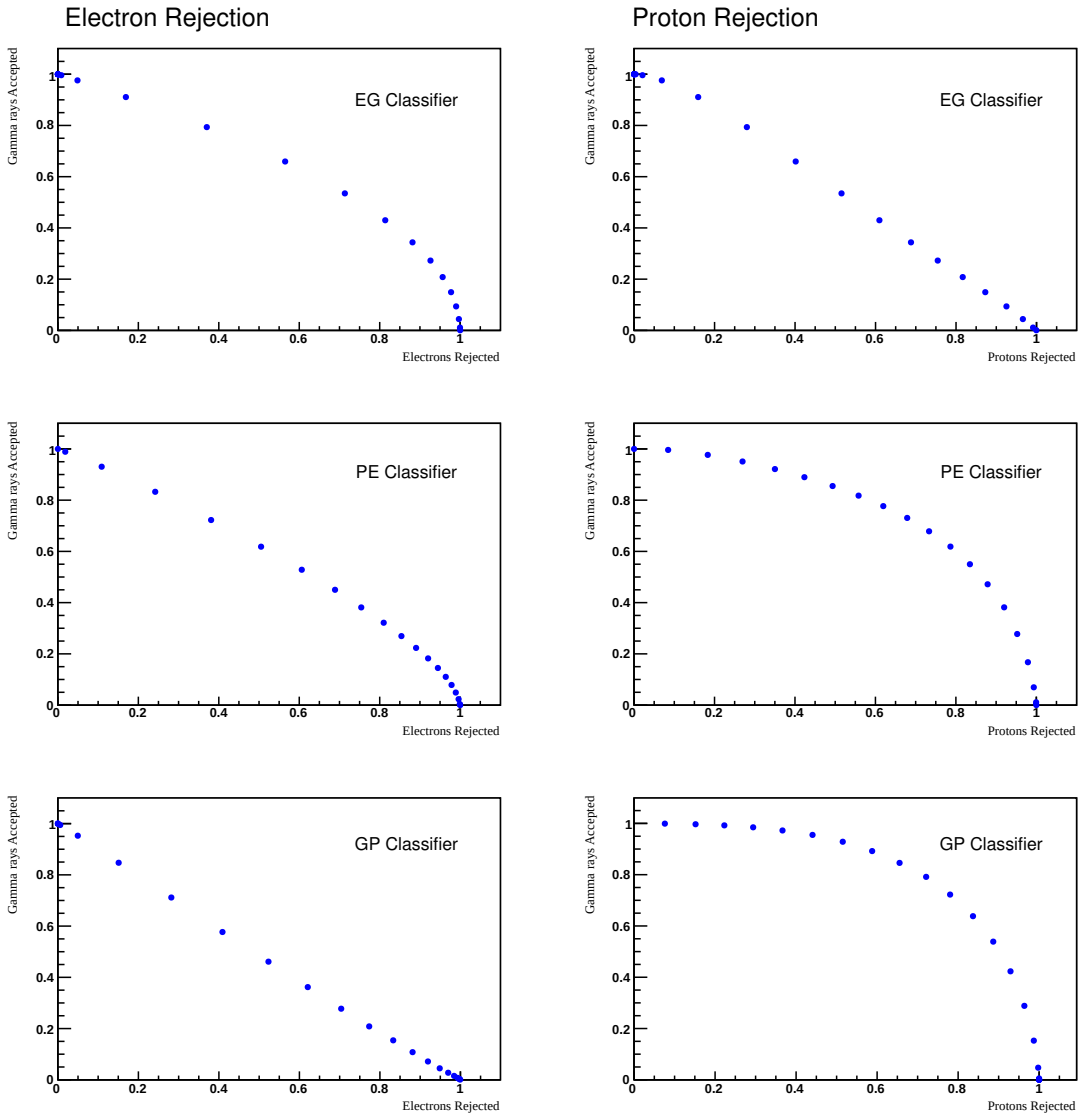

Figure 4.2: The fraction of γ rays left in the sample against the fraction of electrons or protons that would be rejected after making a cut in one of the classifier distributions. Events with a telescope multiplicity of 4, a reconstructed energy of 380 to 900 GeV and an impact parameter of less than 280 m are included. The separation applies to H.E.S.S. I. The left column shows the γ-ray efficiency against the fraction of electrons rejected. The right column is the γ-ray efficiency against the protons rejected. Each row represents different distributions, with the first row corresponding to the EG classifier, the second row the PE classifier and the third row the GP classifier. If no rejection power is achieved, the efficiency curve would be a straight line.

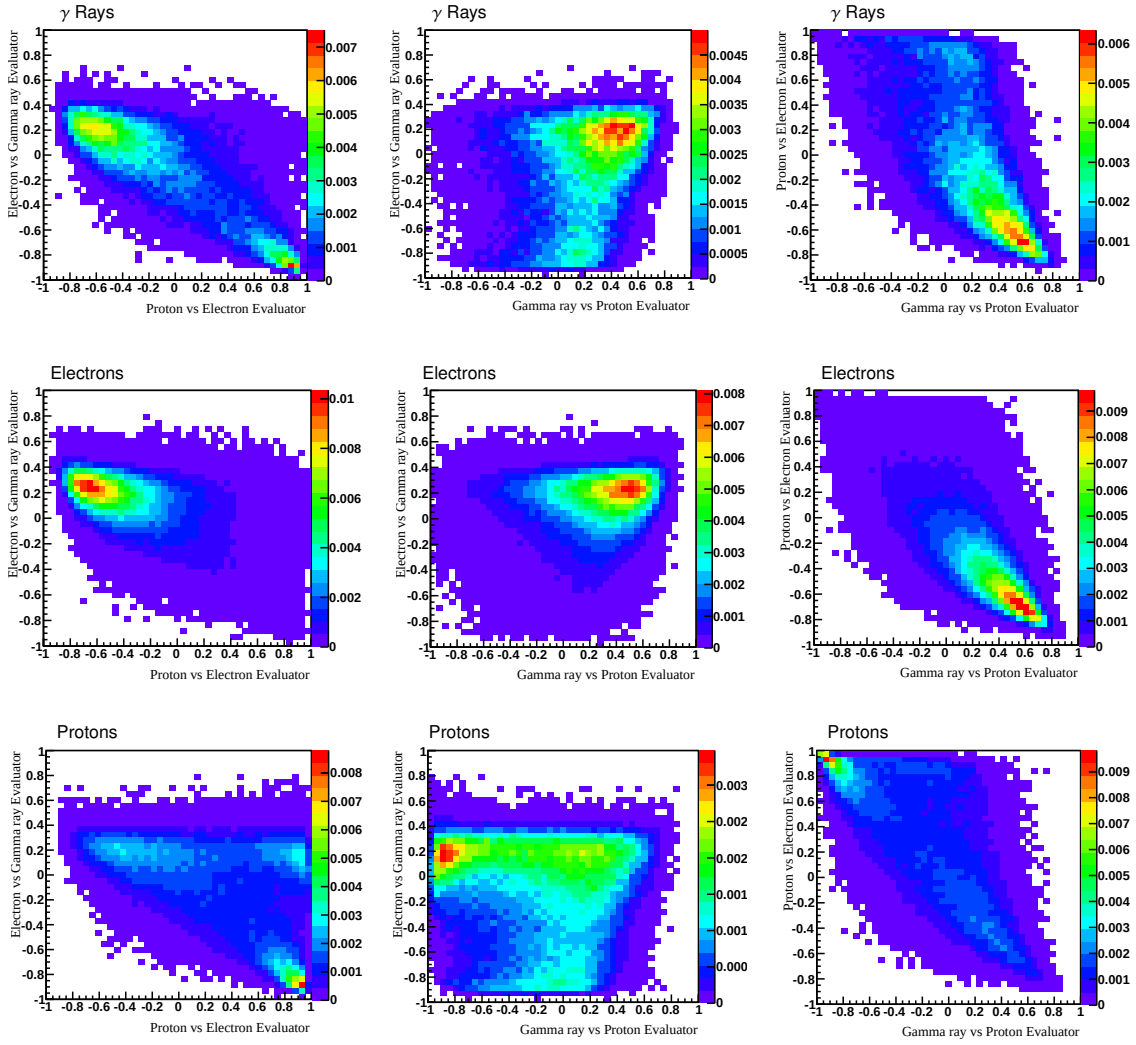

Figure 4.3: The 2D histograms found from combining two classifiers for γ-ray events (top row), electron events (centre row) and proton events (bottom row). Each column represents a different combination of classifiers. LEFT: PE Evaluator against EG Evaluator. CENTRE: GP Classifier against EG Classifier. RIGHT: GP Evaluator against PE Evaluator.

These classifier distributions can be extended to a 2D form by combining classifiers shown in Figure 4.1. There are three classifiers and therefore three combinations used: Electron vs γ-ray classifier against the Proton vs Electron classifier **(EG vs PE)**, Electron vs γ-Ray against γ-Ray vs Proton classifier **(EG vs GP)** and Proton vs Electron against γ-Ray vs Proton classifier **(PE vs GP)**. The histograms representing these combinations are shown in Figure 4.3.

Alternatively, a 3-dimensional cube style analysis can be carried out. This provides a simpler way of simultaneously fitting events.

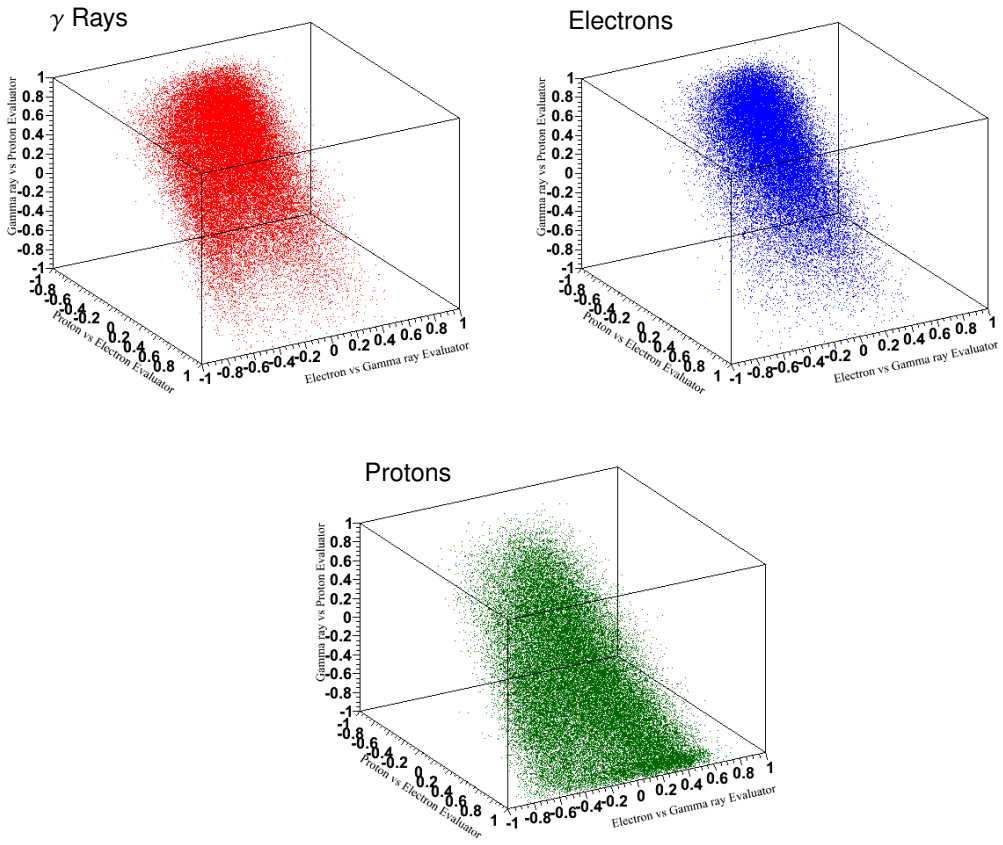

Figure 4.4: The 3D histograms combining all three classifiers for γ-ray events in red, electron events in blue and proton events in green. The x axis represents the EG Evaluator, the y axis the PE Evaluator and the z axis the GP Evaluator.

Figure 4.4 shows how the γ-ray, electron and proton events are spread in the 3D classifier phase space. The electrons are more concentrated than the γ rays, which have a tail that spreads to one corner. The proton events are much less concentrated and more continuous in their shape.

Figure 4.5 shows all three histograms superimposed. What is interesting to see is that, although a large area of the histograms overlap with each other, there is also a large amount of γ-ray and proton events that occupy their own separate phase space. This means that by making a tight cut on events, it would be possible to extract an almost pure γ-ray sample if the statistics allowed for it. A larger number of events is required in order to avoid too many fluctuations and provide a more reliable fit.

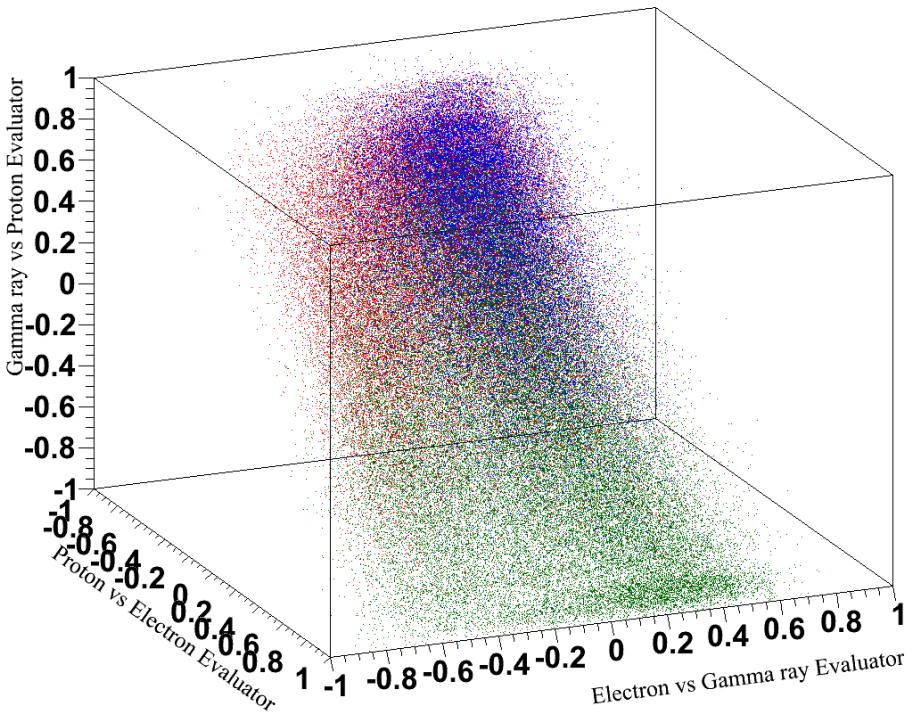

Figure 4.5: The 3D histogram combining all three classifiers. γ-ray events are shown in red, electron events in blue and proton events in green. Events having a reconstructed energy between 380 and 900 GeV and an impact parameter of less than 280 m were selected. Only events involving all four H.E.S.S. I telescopes were considered.

4.2 Fitting Procedure using Test Source PKS 2155-304

4.2.1 Fitting Procedure

The well studied BL Lac PKS 2155-304 was chosen as a test source to compare with simulations. PKS 2155-304 is an ideal source to test as there are many observation runs at low zenith angle. It is an extragalactic point source having an *off* region that is expected to not contain any γ rays coming from the blazar itself. Events with a telescope multiplicity of 4, a reconstructed energy of 380 to 900 GeV and an impact parameter of less than 280 m were selected. In addition, only events with a zenith angle between 10 and 30 degrees were taken, ensuring an average zenith angle of approximately 20 degrees.

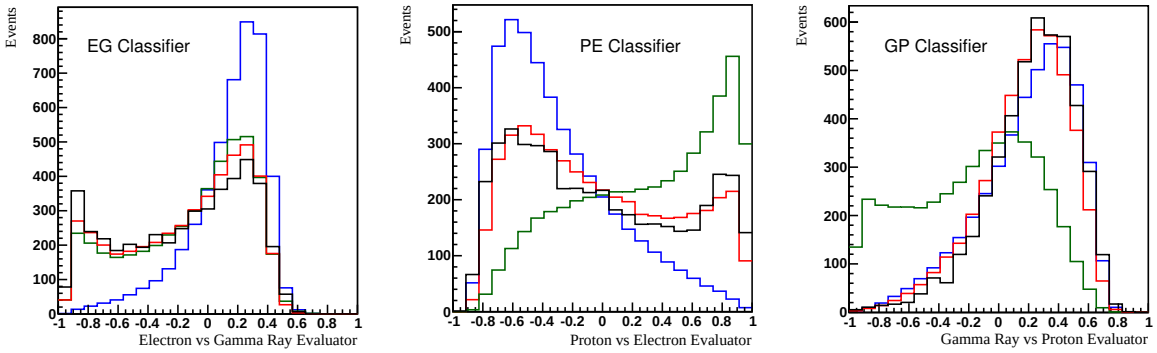

Figure 4.6: The classifier distributions of simulated and data events of PKS 2155-304. EXCESS events of PKS 2155-304 found with the Reflected Background Method are shown as a black line. Both simulated and data events are in the phase1b state. All events with a reconstructed energy between 380 and 900 GeV, a telescope multiplicity of four and an impact parameter of less than 280 m were selected. The red line represents simulated γ-ray events, the blue line electron events and the green line proton events.

The number of Monte Carlo events produced with CORSIKA (Heck 1998) and sim_telarray (Bernlöhr 2008) and used in this analysis follows an index of -2 with simulated energy. As the data is analysed over a large energy band, the index needs to be corrected for by applying the most accurate weighting to the best of our knowledge. When training, the γ-ray events are weighted according to the region being fitted. When comparing excess events, a

spectral index for the quiescent state of Γ = -3.53 (H.E.S.S. Collaboration et al. 2010) was taken. For electrons, an index of Γ = -3.08 (Ackermann et al. 2010a) for the same energy range is used when fitting all three datasets: *excess*, *on* and *off*. Protons are weighted according to the locally measured cosmic ray spectrum of Γ = -2.7 (Olive et al. 2014).

Figure 4.6 shows the 1D classifier distributions and compares them with data taken with H.E.S.S. of PKS 2155-304. As the *excess* events can be assumed to be entirely coming from the source, one would expect the classifying values obtained from these events to follow the γ-ray distribution closely. This is the case, as the best fit value of γ rays is 100% in the *excess* region. The results are summarized in Table 4.1.

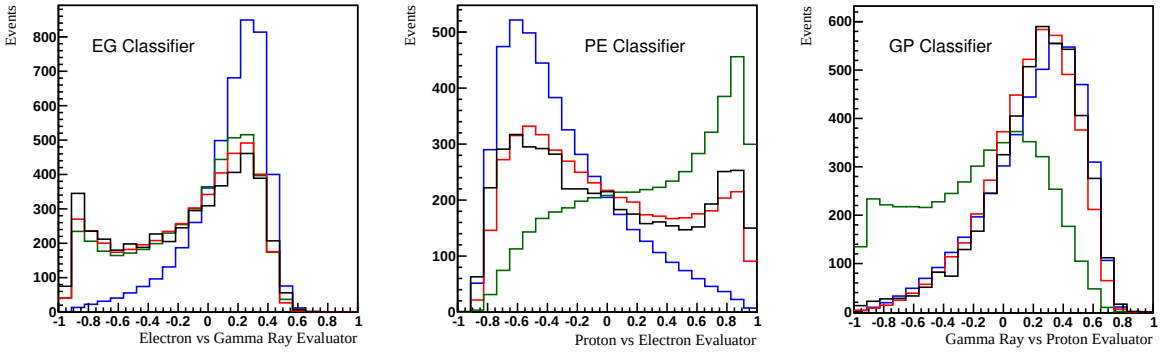

Figure 4.7: Data events from the *on* region of PKS 2155-304 with the Reflected Background Method (black line). All events were observed or simulated in the phase1b state. Classifier values for events with a reconstructed energy between 380 and 900 GeV, an impact parameter of < 280 m and having a telescope multiplicity of four are shown. γ rays are shown in red, electrons in blue and protons in green.

Figure 4.7 shows how the events from the *on* region of data taken of PKS 2155-304 during the quiescent state compares with γ-ray, electron and proton Monte Carlo events. As expected, the *on* region also follows the γ-ray distribution quite closely, although some deviation is expected due to the background contamination of diffuse electrons and protons. Weighting over a large energy band becomes more complex when modelling the diffuse background, as the exact contribution of the isotropic diffuse γ-ray background (IGRB) is unknown. However, as Fermi has measured the IGRB up to 820 GeV (Ackermann et al. 2015a), we can assume the γ-ray flux level is much lower than that of PKS 2155-304 and that weighting according to an index of Γ = -3.53 is a reasonable assumption for the *on*

region.

Due to the sensitive background suppression methods already in place, it is assumed from Monte Carlo studies that heavier nuclei are rejected after selection cuts. Therefore, the remaining contributions in the *off* region are from diffuse cosmic ray protons and electrons. A diffuse γ-ray contribution from the IGRB will also be present. Fermi has fit a power law with an exponential cutoff energy of 279 $\pm$ 52 GeV. The IGRB spectral index up to this cutoff was found to be Γ = -2.32 $\pm$ 0.02. Although this spectral index is found for energies below the threshold of this analysis, it is the current best estimate available and was therefore used to weight the γ-ray events in the *off* region.

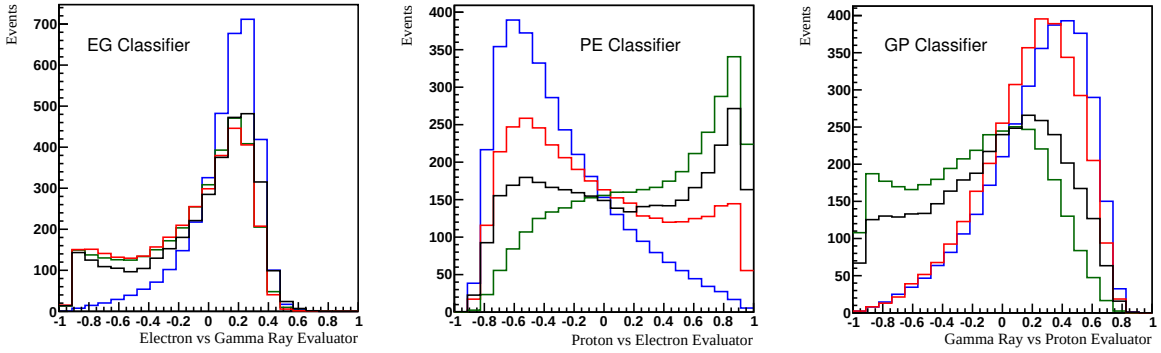

Figure 4.8: Data events from the *off* region of PKS 2155-304 with the Reflected Background Method (black line). All events were taken in the phase1b state. Values for all three evaluators for events with a reconstructed energy between 380 and 900 GeV and having a telescope multiplicity of four. γ rays are shown in red, electrons in blue and protons in green.

Figure 4.8 shows events coming from the background region. Qualitatively, it can be seen that the *off* data seems to have both an electromagnetic contribution as well as a proton component. The fitting procedure is done separately for each region and is outlined below:

- The percentage of γ-ray, electron and proton events are varied between -100 and 100%. A criteria was placed that the sum of contributions must add up to 100%. The fit varied to -100% to allow enough phase space for an accurate minimization while restricting the computational time needed to make the fit.

- A linked fit is performed whereby the χ^2 values of all three classifier distributions is summed. The summed χ^2 value is then minimized to find the best fit. This is done with the Minuit package of ROOT (James 1994).

The best fit model to the data for the *excess*, *on* and *off* events are presented in Figure 4.9. Figure 4.10 details the corresponding γ-ray, electron and proton percentages given by the best fit, which is also outlined in Table 4.1.

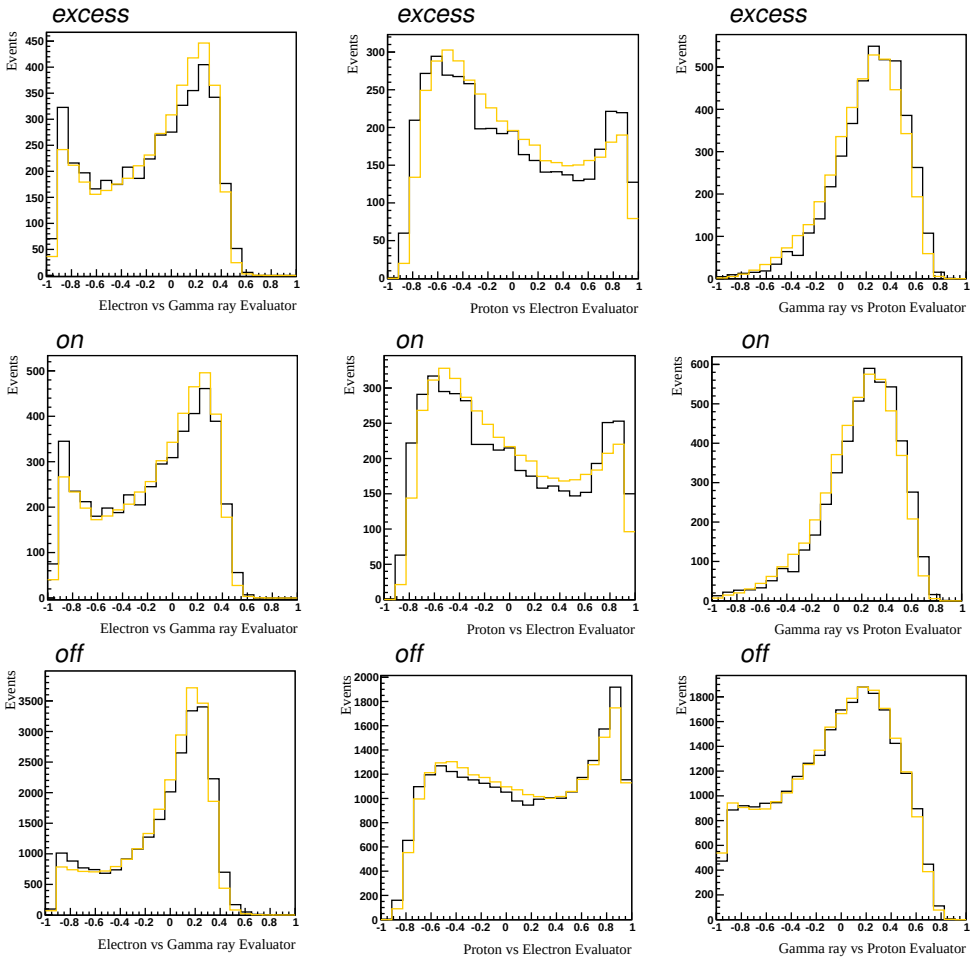

Figure 4.9: The distributions of the three different classifiers used to separate the particle types. The line in black shows the PKS 2155-304 data. The line in yellow shows the best fit. Each row represents a different set of events in the data sample, with the top row showing the *excess* events, the middle row the *on* events and the bottom row the *off* events.

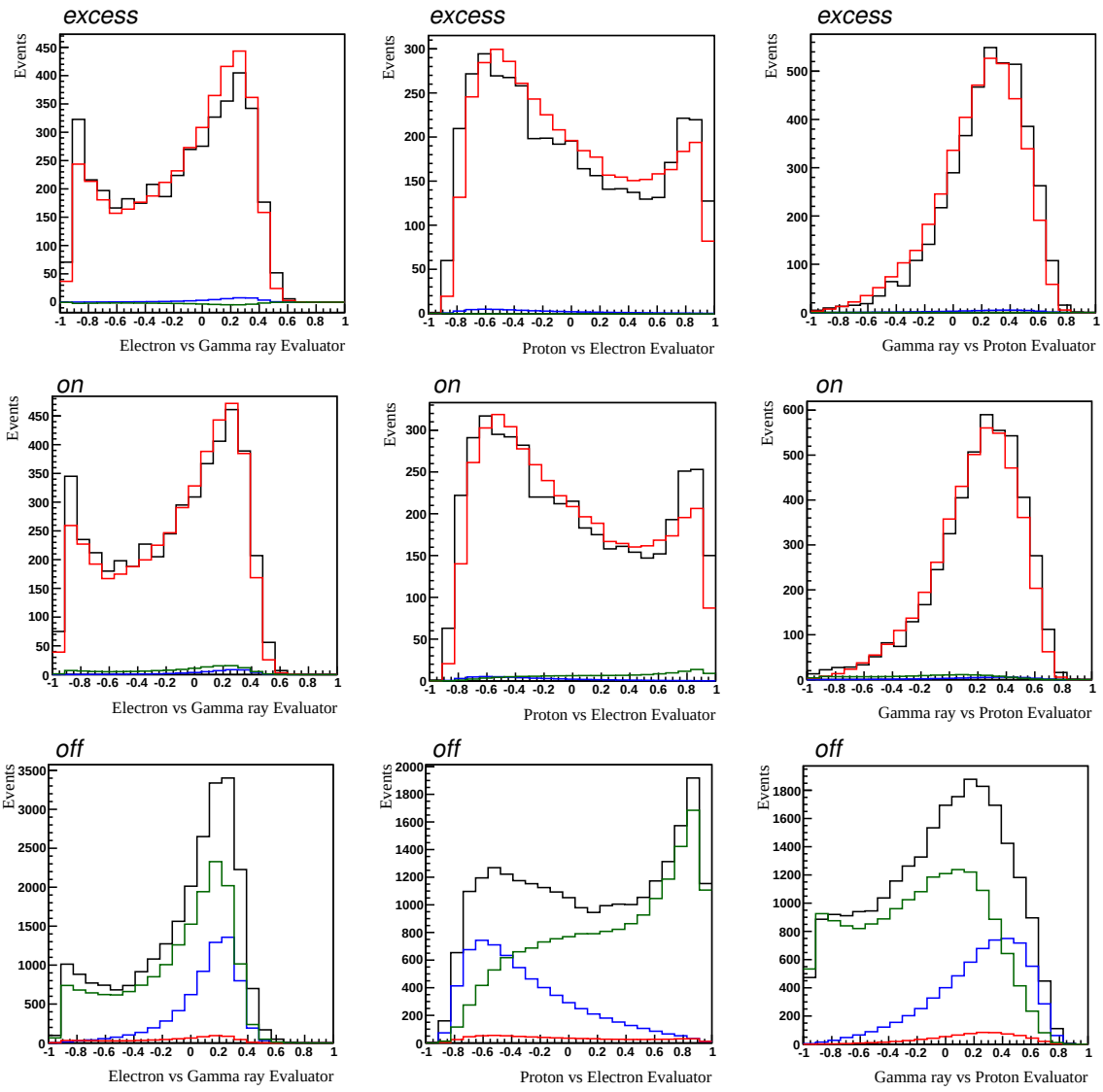

Figure 4.10: The *excess*, *on* and *off* events of PKS 2155-304 observations are shown. The top row represents the *excess* events, the middle row the *on* events and the bottom row the *off* events. Each column shows a different classifier. The best fit amount of γ rays is shown in red, electrons in blue and protons in green.

Region	γ rays	Electrons	Protons
excess	100 ± 1%	1 ± 1%	-1 ± 1%
on	99 ± 5%	-2 ± 4%	3 ± 2%
off	3 ± 4%	30 ± 3%	67 ± 1%

Table 4.1: 1D analysis fit results of the γ-ray, electron and proton percentages for *excess*, *on* and *off* events of PKS 2155-304.

In a similar way, the 2D fit procedure of PKS 2155-304 data includes the same steps outlined above. The 2D histogram of data taken in the phase1b state was compared to the three histograms displayed in Figure 4.3. The summed χ^2 of these three fits, each using two classifiers, is then minimized to find the most accurate combination of electrons, protons and γ rays (Table 4.2). Figure 4.11 shows the 2D histograms for the PKS 2155-304 data for the *excess*, *on* and *off* regions. The best fit model found for each region is shown in Figure 4.12.

Region	γ rays	Electrons	Protons
excess	100 ± 0%	1 ± 1%	-1 ± 1%
on	99 ± 2%	-3 ± 2%	4 ± 1%
off	7 ± 1%	27 ± 1%	66 ± 1%

Table 4.2: Fit results of the γ-ray, electron and proton components for *excess*, *on* and *off* events in the 2D analysis of PKS 2155-304.

The results of the fitting procedure on PKS 2155-304 is compatible with what is expected from Monte Carlo studies. Both the 1D and 2D analyses gave a result of 100% γ rays for the *excess* region. As the region is found from subtracting the background distribution from events detected on source, a 100% estimation of γ rays in the *excess* region is expected. The *off* region fit in the 1D case gives a low estimate for the γ rays that is consistent with zero at 3±4%.

The 2D fit in the *off* region, however, gives a higher estimate of γ rays. Though, as shown in Section 4.3, lower event numbers can cause the fit to behave less accurately.

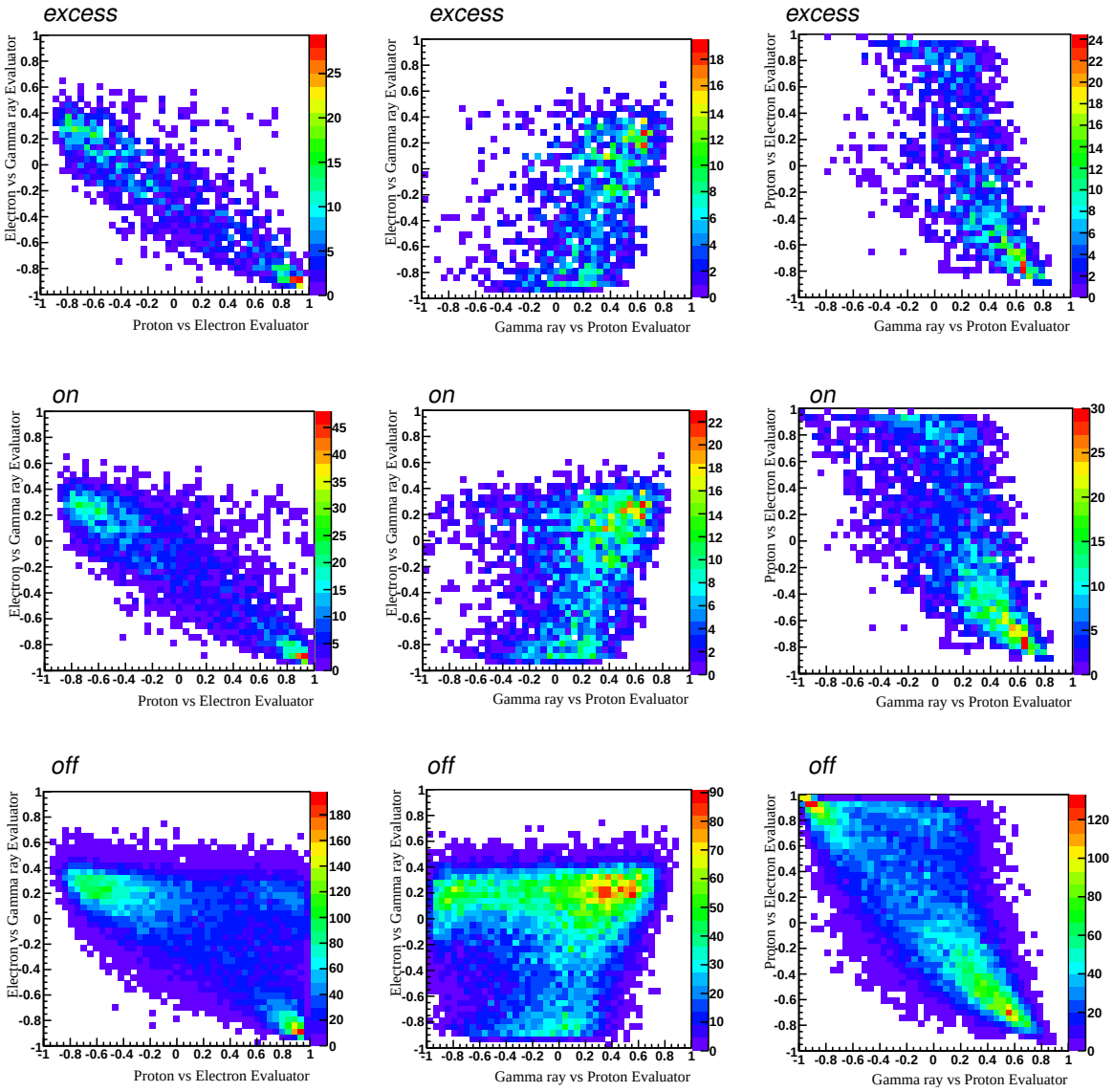

Figure 4.11: The 2-dimensional histograms of PKS 2155-304 observation regions. Different combinations of classifiers for events coming from regions on and near PKS 2155-304 are shown. The top row shows how the shape of the classifiers of events is the *excess* data, the middle row the *on* region and the bottom row the *off* region. Each column represents a different combination of classifiers, denoted by the axes.

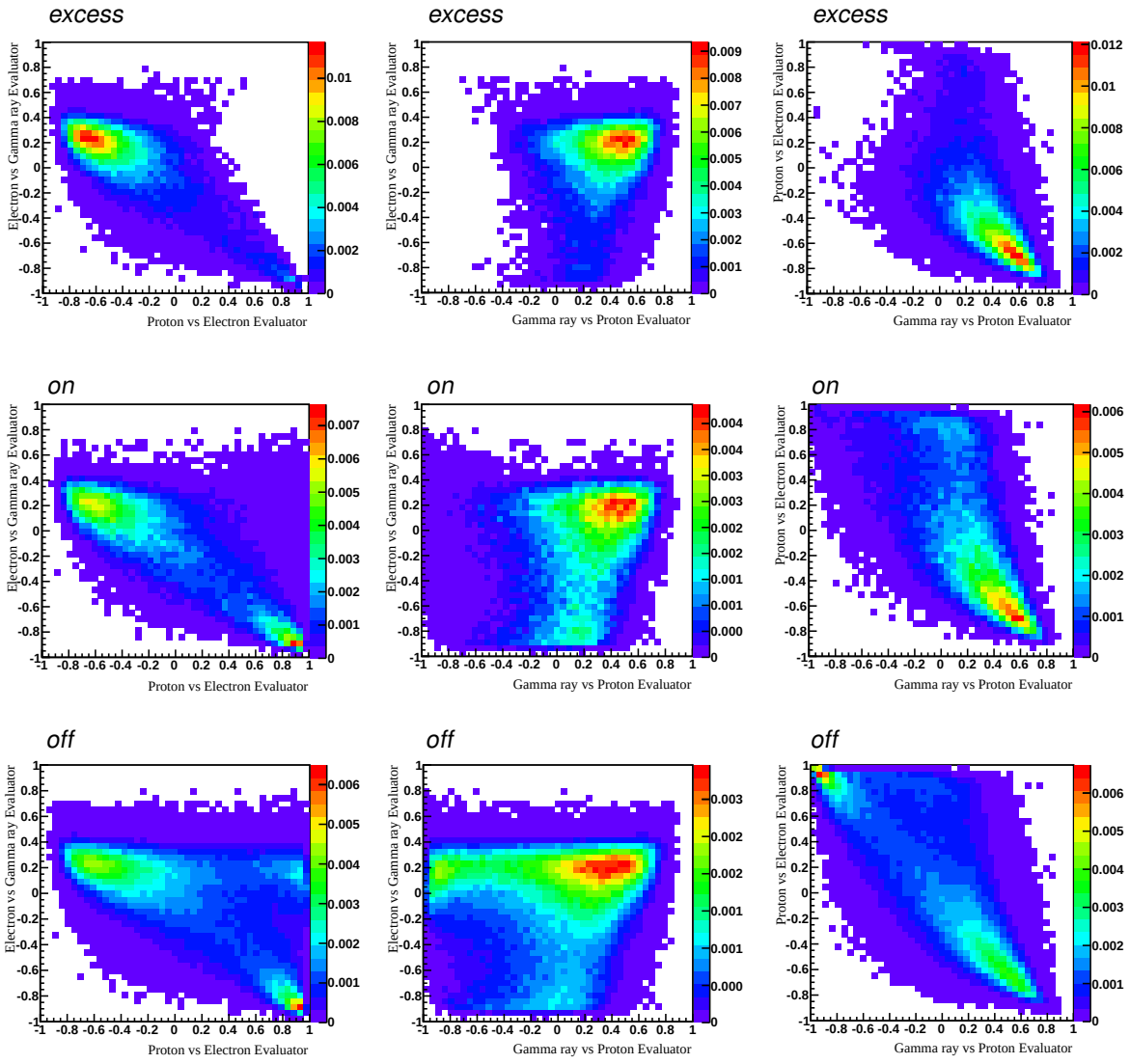

Figure 4.12: The best fit model using simulated events in the 2-dimensional analysis of PKS 2155-304. Each row represents a different sample of events from observations taken of PKS 2155-304. The top row is the *excess* events, the middle row the *on* events and the bottom row the *off* events. Each histograms displays a combination of the γ-ray, electron and proton profiles found in 4.3.

For this reason, the 3D analysis was not included in the test case. The electron to proton ratio in the *off* region was found to be 0.39 for the 1D fit and 0.37 in the 2D analysis.

4.2.2 Zenith Angle Dependence

As simulated events at zenith angles other than 20 degrees were not readily available, the true zenith angle dependence on the fit result is unclear. Although a wide zenith angle range was taken during the fitting of PKS 2155-304 to ensure a large number of events, the range was also carefully chosen so that the zenith angle distribution was centred on 20 degrees. This was to ensure the data represented the simulations as closely as possible.

Zenith Angle	Region	γ rays	Electrons	Protons
0 - 10	*excess*	100 ± 0%	-23 ± 4%	23 ± 4%
	on	100 ± 0%	-25 ± 3%	25 ± 3%
	off	49 ± 7%	-16 ± 4%	67 ± 3%
10 - 20	*excess*	100 ± 0%	-10 ± 3%	10 ± 3%
	on	100 ± 0%	-13 ± 3%	13 ± 3%
	off	32 ± 5%	2 ± 3%	66 ± 2%
15 - 25	*excess*	100 ± 2%	0 ± 3%	0 ± 2%
	on	100 ± 7%	-3 ± 6%	3 ± 3%
	off	9 ± 4%	22 ± 2%	69 ± 2%
20 - 30	*excess*	73 ± 6%	31 ± 6%	-4 ± 2%
	on	66 ± 6%	32 ± 5%	2 ± 3%
	off	-20 ± 4%	48 ± 2%	72 ± 2%
30 - 40	*excess*	4 ± 4%	97 ± 3%	-1 ± 2%
	on	-1 ± 5%	96 ± 3%	5 ± 3%
	off	-72 ± 2%	91 ± 1%	81 ± 2%

Table 4.3: Fitted estimates of the γ-ray, electron and proton components for *excess*, *on* and *off* events of PKS 2155-304. The values were found using the 1D linked analysis. Different zenith angle bins (left column) were chosen in the data sample while the simulations used were at a zenith angle of 20 degrees.

To test the effect of zenith angle on the fit result, observations of PKS 2155-304 were used instead. Table 4.3 shows the estimated γ-ray, electron and proton percentages for different zenith angle bins between 0 and 40 degrees.

The classifiers are very sensitive to the zenith angle range. Only values close to the zenith angle of the simulated events used in the TMVA training should be considered in the analysis. Comparing the fit results, using events with a zenith angle between 15 and 25 degrees is reasonable.

4.2.3 Uncertainty Estimate

The uncertainty on the fitted values of each contribution was taken as the 1σ errors of the χ^2 distribution. The χ^2 values found in the 2D fit for different combinations of γ-ray, electron and proton events in the *excess*, *on* and *off* data are shown in 4.14.

The fit was allowed to range between -100% and 100% for each component, with the requirement that all contributions add up to a total of 100%. The corresponding χ^2 histograms for the 1D fit are shown in 4.13.

To minimize computational time needed for the analysis, the package Minuit (James 1994) implemented into the ROOT framework was used. After defining initial parameters, Minuit estimates the parabolic shape of the χ^2 distribution to determine the minimum position and the corresponding 1σ errors. Systematic studies on simulations are discussed in Section 4.3.

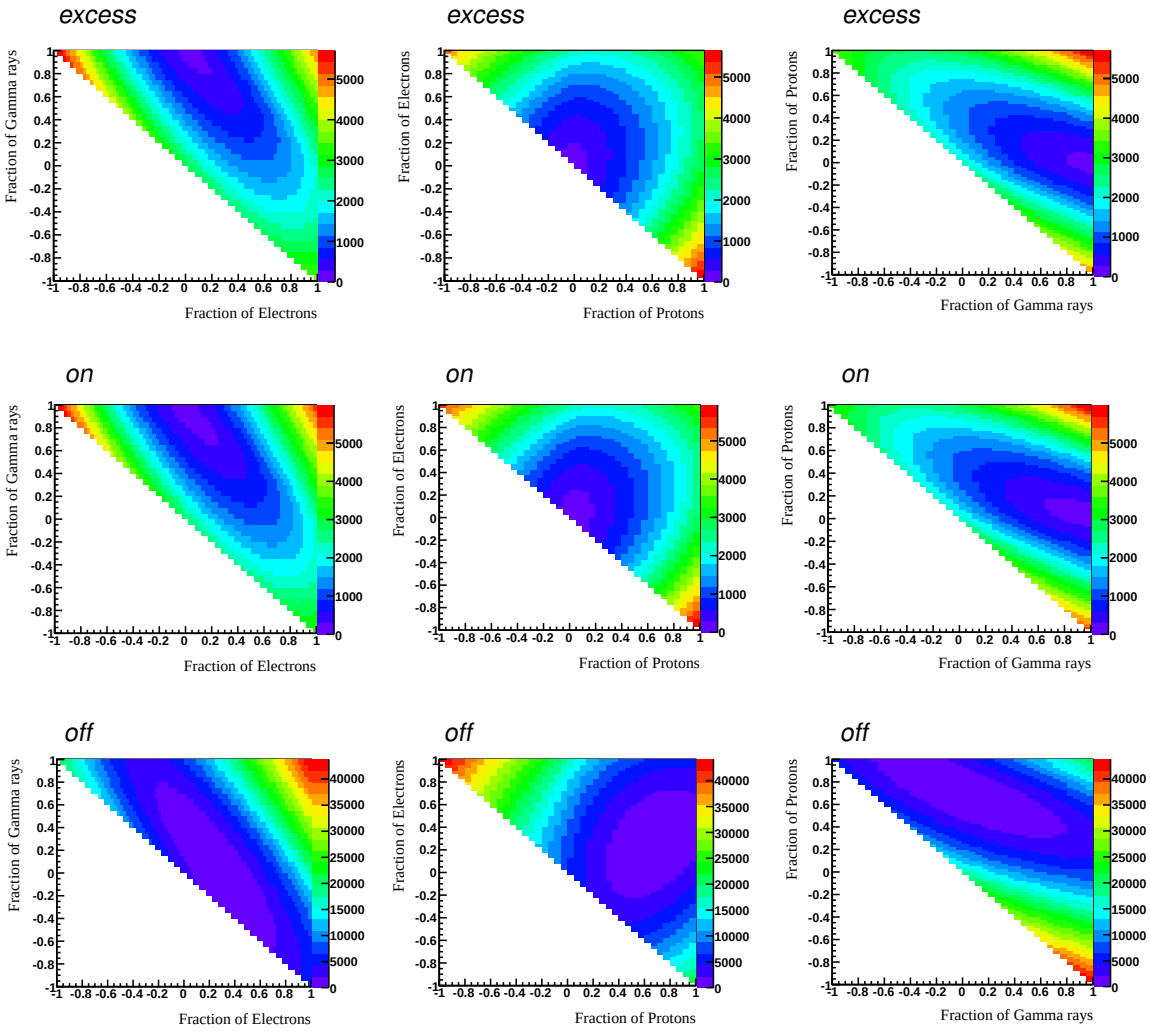

Figure 4.13: Histogram of summed χ^2 values obtained in the linked 1D analysis. The x and y axes represent the fraction of γ rays, electrons or protons used. χ^2 values found from fitting *excess* events (TOP), the *on* region (CENTRE) and the *off* region (BOTTOM).

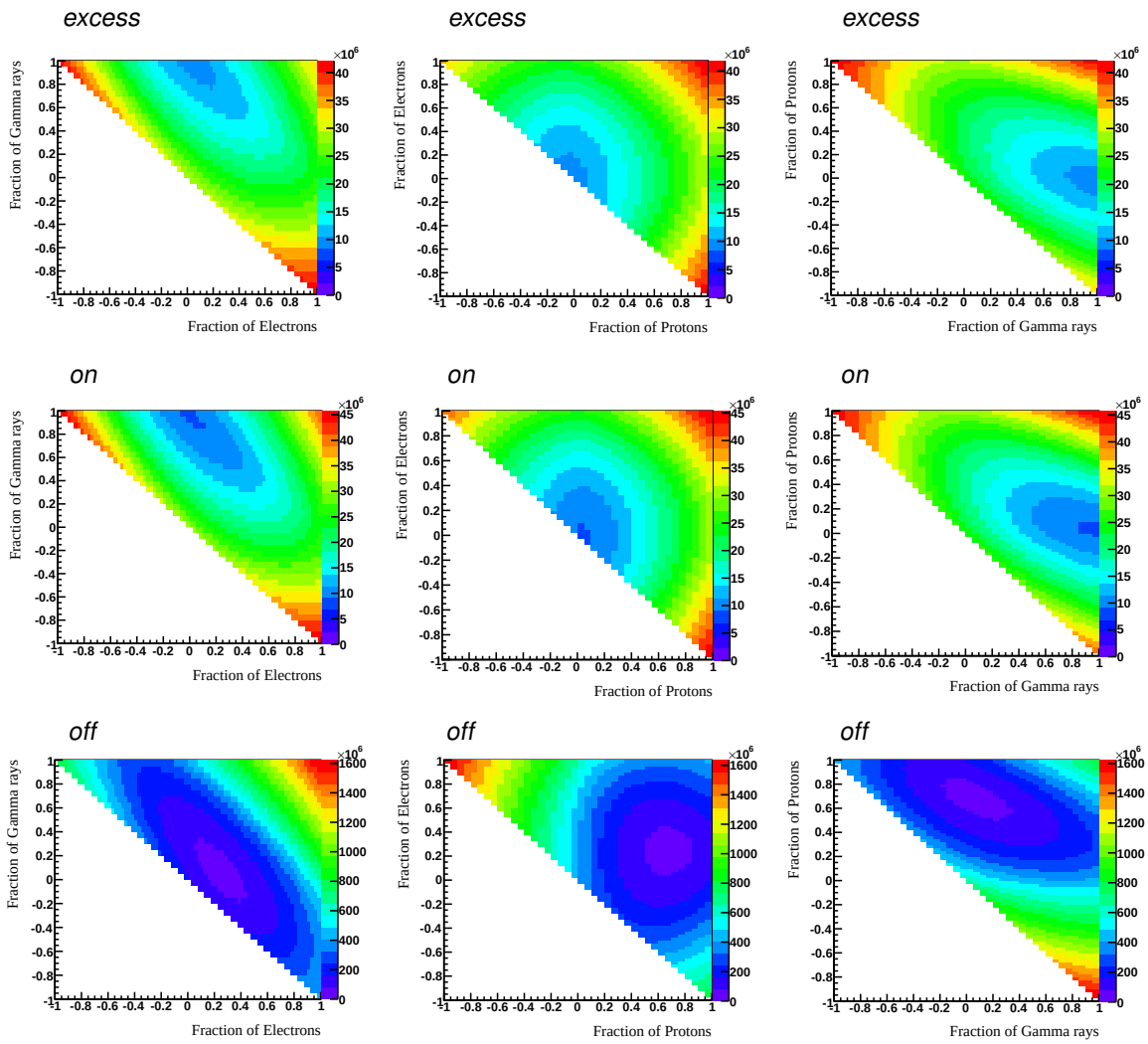

Figure 4.14: Histogram of summed χ^2 values obtained in the linked 2D analysis. The x and y axes represent the fraction of γ rays, electrons or protons used. χ^2 values found from fitting *excess* events (TOP), the *on* region (CENTRE) and the *off* region (BOTTOM).

4.3 Performance

A series of tests using simulations were carried out to investigate the validity of the method and the accuracy of any results obtained. Dependencies on the offset, zenith angle (Section 4.2.2) and the fraction of γ rays were tested to better understand any biases involved. All simulations were in the phase1b state and produced at a zenith angle of 20 degrees. A maximum cut on the offset of 2 degrees was made.

4.3.1 γ Fraction

As this method involves a three component fit, misclassification can occur between any primary particle. The question is how accurate does the fit behave and is the amount of misclassification constant with an increasing contribution of γ rays.

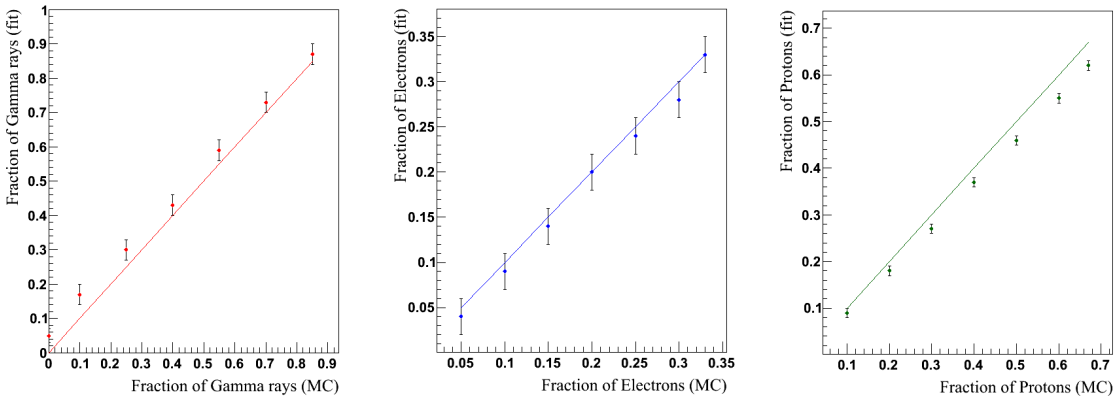

Figure 4.15: The true fraction of simulated γ rays, electrons and protons compared with the estimated fraction from the 1-dimensional analysis. The lines denotes the true fractions and the points show the estimated values and their associated 1σ errors.

Figure 4.15 shows how accurately each particle component is estimated for the 1D linked analysis. The fitted γ-ray, electron and proton fractions are compared to the simulated values. The γ rays are overestimated by ≈4-5% and the protons underestimated by ≈2-3%. The amount of misclassification is approximately constant with increasing γ-ray fraction to within a few percent.

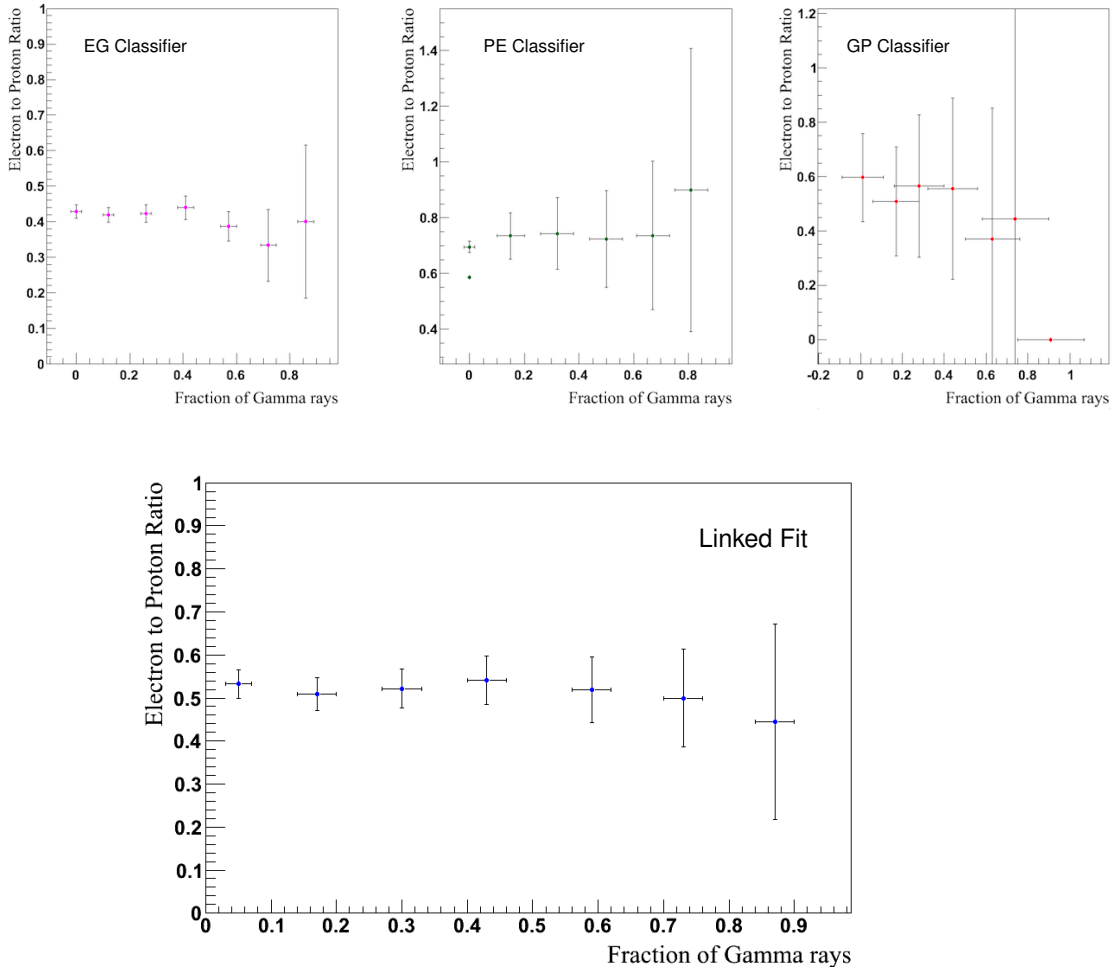

Figure 4.16: The fitted electron to proton ratio against the fitted fraction of γ rays. The simulated electron to proton ratio is 0.5. TOP: The fitted electron to proton ratio found from fitting the 1-dimensional histograms of classifiers EG (left) PE (middle) and GP (right). BOTTOM: The fitted ratio of electrons to protons for the linked 1-dimensional fit - minimizing on the summed χ^2 value of all three classifiers.

Different event types were combined into the same simulation sample with the percentage of γ rays varying between 0 and 85%. The ratio of electrons to protons was kept constant at 0.5. Figure 4.16 shows the electron to proton ratio found with varying γ-ray fractions when using just a single classifier. The effect of any biases present are maximised when fitting with an individual classifier. The ratio of electrons to protons is a common validity check used in Section 4.2 and Chapter 5 and is used to test the stability of the method.

The EG classifier underestimates the electron to proton ratio (Figure 4.16) by underestimating the proton fraction (Figure 4.15). The PE classifier overestimates the number of electrons to protons and the third classifier - GP - overestimates the ratio at lower γ-ray fractions and underestimates it at larger fractions.

The results found using the GP classifier is not expected to be as stable as the other two. As the classifier distribution for γ-rays is almost identical to the one for electrons (Figure 4.1), a high level of misclassification between the two species is expected. This is seen in Figure 4.16, where the GP evaluator has large fluctuations of the electron to proton ratio, and is especially inaccurate when a large γ-ray component is present. However, the proton distribution is well separated and therefore, the GP classifier is more accurate in determining the correct fraction of protons.

The linked fit found from minimizing the summed χ^2 values when fitting the simulated data sample to three 1-dimensional histograms. The linked fit was introduced in order to decrease any biases that might be present when fitting the individual histograms. As shown in Figure 4.16, the effect of the misclassification when fitting with individual classifiers is greatly reduced, with the electron to proton ratio estimated correctly (within errors) for various γ-ray fractions.

Using two classifiers to make a combined fit gives less variation in the fit with changing γ-ray percentage. Figure 4.17 shows the fitted electron to proton ratio for the 2D analysis. A linked fit whereby the χ^2 values for each classifier distribution shown in Figure 4.3 was summed. Reducing this summed χ^2 value gives a result that is consistent with simulations. Details of the fitting procedure are described in Section 4.2. The fit result is steady for all γ-ray fractions.

Figure 4.19 shows the fit results for the 3D analysis. The 3D fit estimates a stable electron to proton ratio for all γ-ray fractions. However, a larger number of events is required.

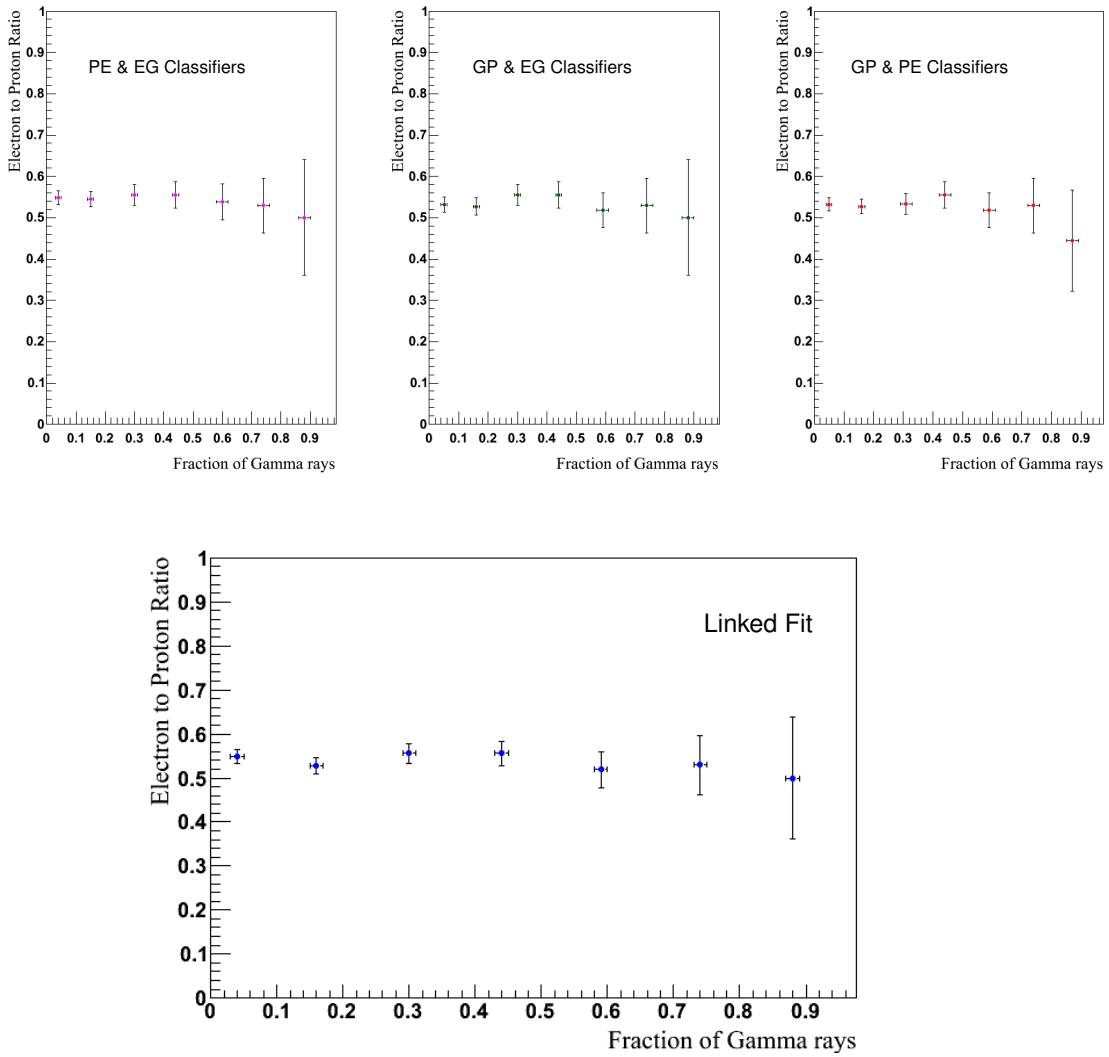

Figure 4.17: The fitted electron to proton ratio against the fitted fraction of γ rays. The simulated electron to proton ratio is 0.5. TOP: The fitted value of electrons over protons in the 2-dimensional fit. Two classifiers were combined for each fit: PE vs EG classifier (left) GP vs EG classifier (middle), and GP vs PE evaluator (right). BOTTOM: The ratio of electrons to protons estimated in the 2-dimensional linked analysis.

The fitted values of the γ ray, electron and proton components in the 2D analysis are compared to the true components in Figure 4.18. The electron values are estimated well, though the proton values have slightly lower values and the γ rays slightly higher. As the γ-ray fraction increases, the fitted values are consistently under- or overestimated and do not tend further way from their true values. Although misclassification is present, the extent of this misclassification is not dependent on how large or small the fraction of γ rays in the data sample is.

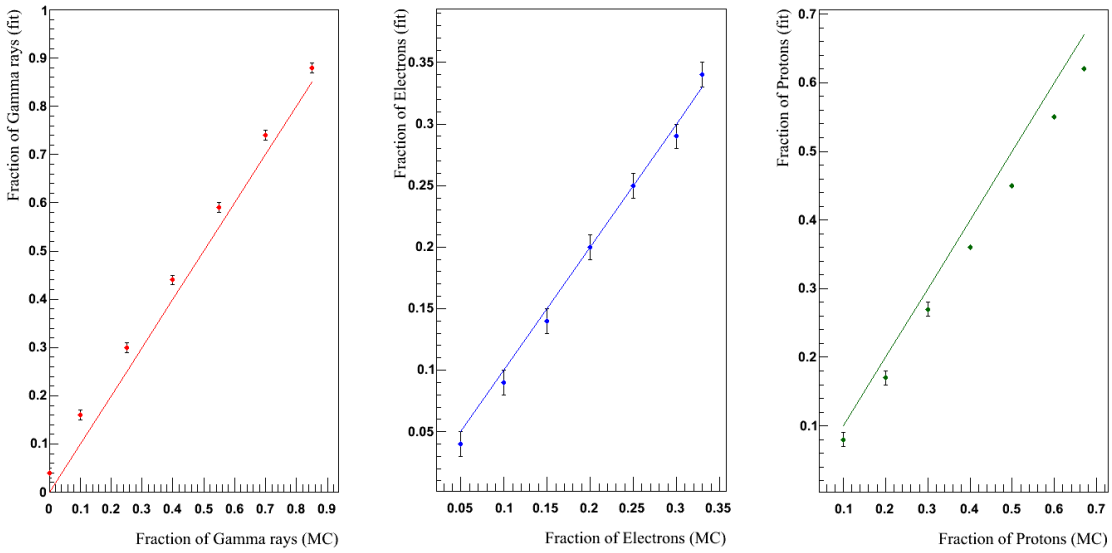

Figure 4.18: The true fraction of simulated γ rays, electrons and protons compared to the fitted fraction in the 2-dimensional analysis. The line shows where the true values lie and the points show the fitted values with their associated 1σ errors.

The uncertainty can be estimated in the 1D fit for γ rays, electrons and protons to be as high as 7%, 1% and 6% respectively. For the 2D fit, the error in the fitting procedure can be estimated as 6%, 1% and 2% respectively.

The fitted values of electron to proton events in the 3D analysis, shown in 4.19, is also consistent with 0.5 and remains constant with different γ-ray fractions. The corresponding fitted γ-ray, electron and proton fractions are consistent with the values obtained in the 1D and 2D analyses and are not dependent on the amount of γ rays present in the data.

The 3D approach, like the 2D fit, has disadvantages when event numbers are low, making the fit less accurate due to a larger number of empty bins. Though the results of the 1D, 2D and 3D fits are compatible, the tests discussed here are done with a large sample of simulated events.

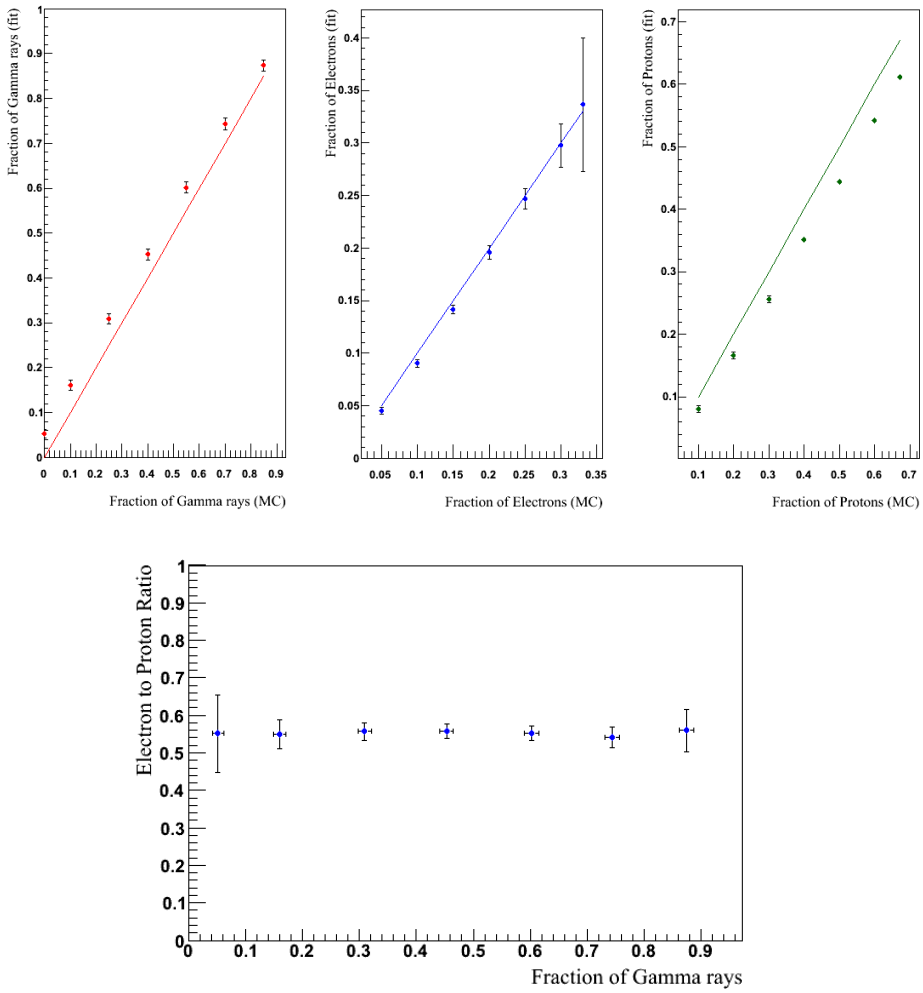

Figure 4.19: TOP: The fitted fraction of simulated γ rays, electrons and protons compared with the true fraction from the 3-dimensional analysis. The line shows the where the true values lie and the points show the fitted values and their 1σ errors. BOTTOM: The electron to proton ratio that was fitted from the 3-dimensional linked analysis. The electron to proton ratio for each mixture of events was at 0.5.

4.3.2 Offset Dependence

As we have seen in the previous section, the electron to proton ratio does not change with a varying γ-ray fraction. Here, the dependence on a varying offset is tested. This offset is the distance of the reconstructed source position to the centre of the nominal camera system, or telescope array.

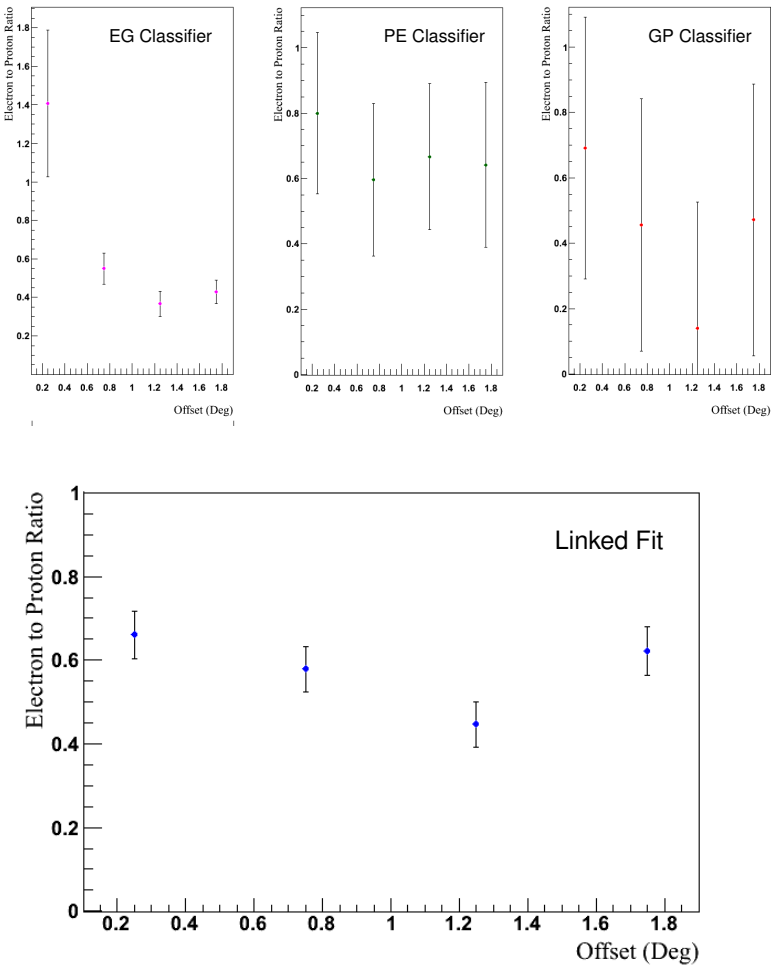

Figure 4.20: The number of electrons to protons from the 1-dimensional analysis, fitted for four offset bins from 0 to 2 degrees. TOP: the electron to proton ratio found from fitting each individual classifier - electrons vs γ rays (left), protons vs electrons (centre), γ rays vs protons (right). BOTTOM: Electron to proton ratio found from fitting all three classifiers simultaneously in the linked analysis.

Simulated events of electrons, protons and γ rays were combined into the same file with 10% of events being γ rays, 30% electrons and 60% protons. This was done for four offset bins: 0 - 0.5 degrees, 0.5 - 1 degrees, 1 - 1.5 degrees and 1.5 - 2 degrees, giving an electron to proton ratio of 0.5 for each offset band.

Figure 4.20 shows the electron to proton ratio estimated in the 1D fit. The electron to proton value from fits using just one classifier varies over a wide range. For both the EG and GP classifiers, the electron to proton ratio is found to be much higher in the lowest offset bin. The ratio decreases at larger offsets with the exception of events between 1.5 and 2 degrees.

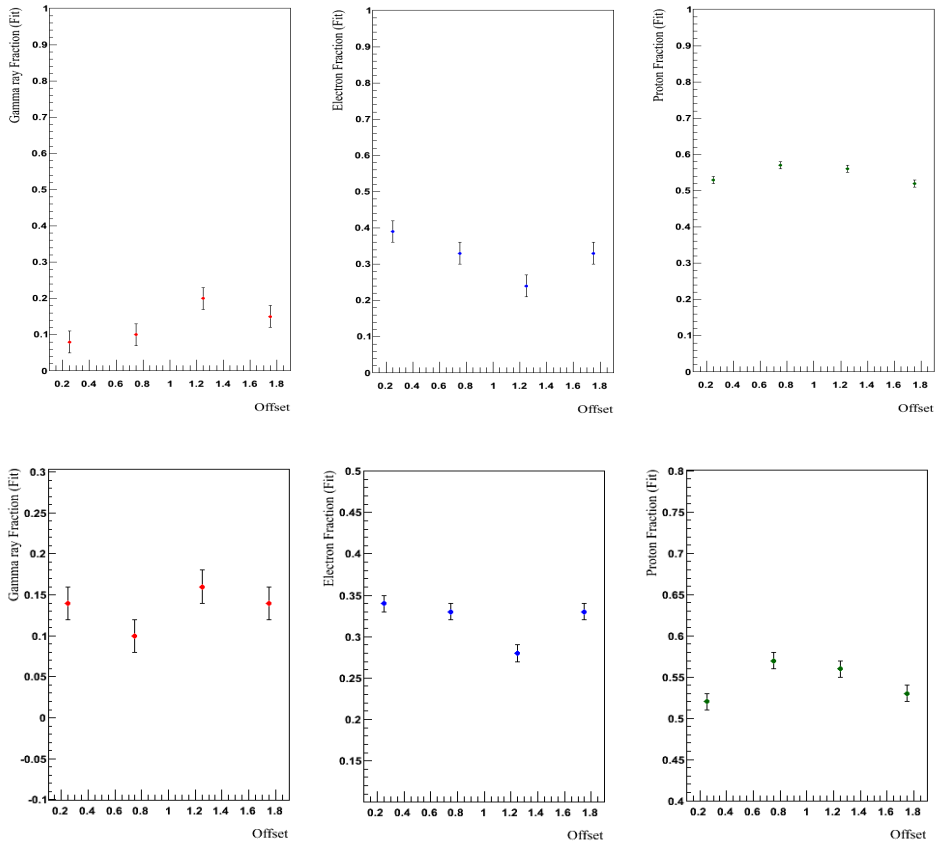

Figure 4.21: The fitted γ-ray, electron and proton fractions for the 1D (TOP) and 2D (BOTTOM) linked analyses. The simulated data files contained 10% γ rays, 30% electrons and 60% protons in each offset band. The γ-ray, electron and proton components were fit in four offset bins: 0 - 0.5 degrees, 0.5 - 1 degrees, 1 - 1.5 degrees and 1.5 - 2 degrees.

The linked fit between all three classifiers over each offset band is shown in Figure 4.20. There is a dependence on the electron to proton ratio with offset. A decreasing ratio is found for the first three offset bins and a higher value for events between 1.5 to 2 degrees. The electron to proton ratio is more stable than the individual fits in the 1D analysis.

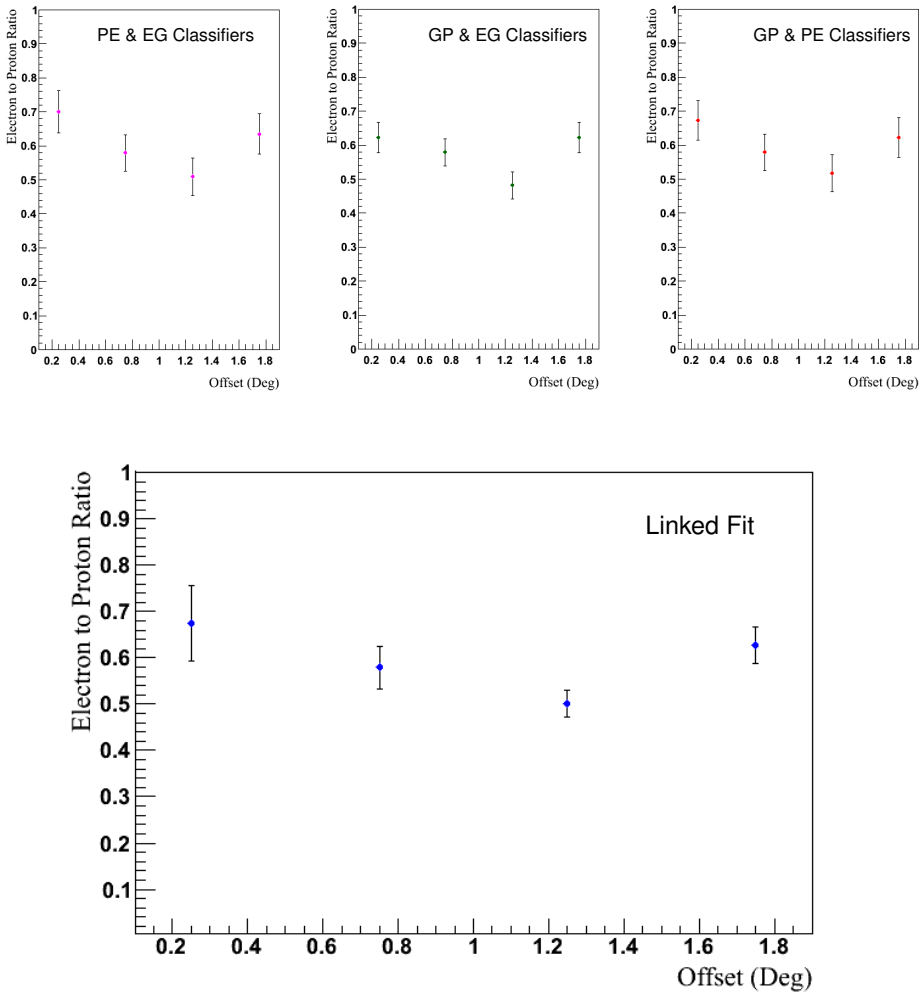

Figure 4.22: Electron to proton ratio from the 2-dimensional analysis, fitted for four offset bins from 0 to 2 degrees. TOP: the electron to proton ratio when combining two classifiers - PE against the EG classifier (left), GP and the EG classifier (centre), GP evaluator and the PE evaluator (right). BOTTOM: Electron to proton value found in the linked analysis by minimizing the summed χ^2 value of these combinations.

The fitted fraction of γ rays, electrons and protons found in the 1D linked analysis is shown in Figure 4.21. The fraction of γ rays is estimated correctly at lower offsets, and overestimated for events above 1 degree. The proton fraction is underestimated at all offset values. The electron fraction, however, decreases with offset with the exception of events between 1.5 and 2 degrees.

Figure 4.22 shows the number of electron to proton events estimated in the 2D analysis. Combining a second classifier improves the result, though the same dependency on offset can be found in all three classifier combinations. The linked fit, making use of these three combinations, behaves in the same way as the 1D linked analysis.

The best fit γ-ray, electron and proton fractions in all offset bins in the 2D analysis is shown in Figure 4.21. The percentage of γ rays and electrons is generally overestimated, while the proton fraction is underestimated. The value of each component varies within a 10% range. It is clear to see that the dependence of the electron to proton ratio in the 1D and 2D analyses comes from the behaviour exhibited in the fitted electron and proton components. In both analyses, the fitted electron fraction slowly decreases for the first three offset bins, and rises again after 1.5 degrees. Dividing this value by the proton fraction, which exhibits approximately the inverse behaviour, exaggerates this trend.

With large event numbers, the value of electrons to protons found in the 3D analysis is compatible with the results found in the 1D and 2D fit (Figure 4.23). Similarly, a decrease in the ratio is found with increasing offset, with a larger value found at 1.5 to 2 degrees.

Additionally, the number of electrons to protons in each offset bin with increasing γ-ray fraction was also found. Figure 4.24 shows the values found for four offset bins between 0 and 2 degrees. The true electron to proton ratio is 0.5 for each offset bin. The value is shown to be constant with varying γ-ray fractions for all offsets, with the value being overestimated except for events between 1 and 1.5 degrees.

Tests using Monte Carlo events do show a dependency of the estimated γ-ray, electron and proton fractions on the offset distribution. Therefore, this dependency should be taken into account when analysing real data. However, this value is neither over nor underestimated once the full offset range is included. When the full range of diffuse events between 0 and 2 degrees is selected (Section 4.3.1), the estimates are consistent with the true values.

This suggests analysing diffuse emission over the full field of view will give a more accurate estimate of the contribution of each component to the data sample. When analysing diffuse data within smaller offset bins, however, an offset dependence might be seen depen-

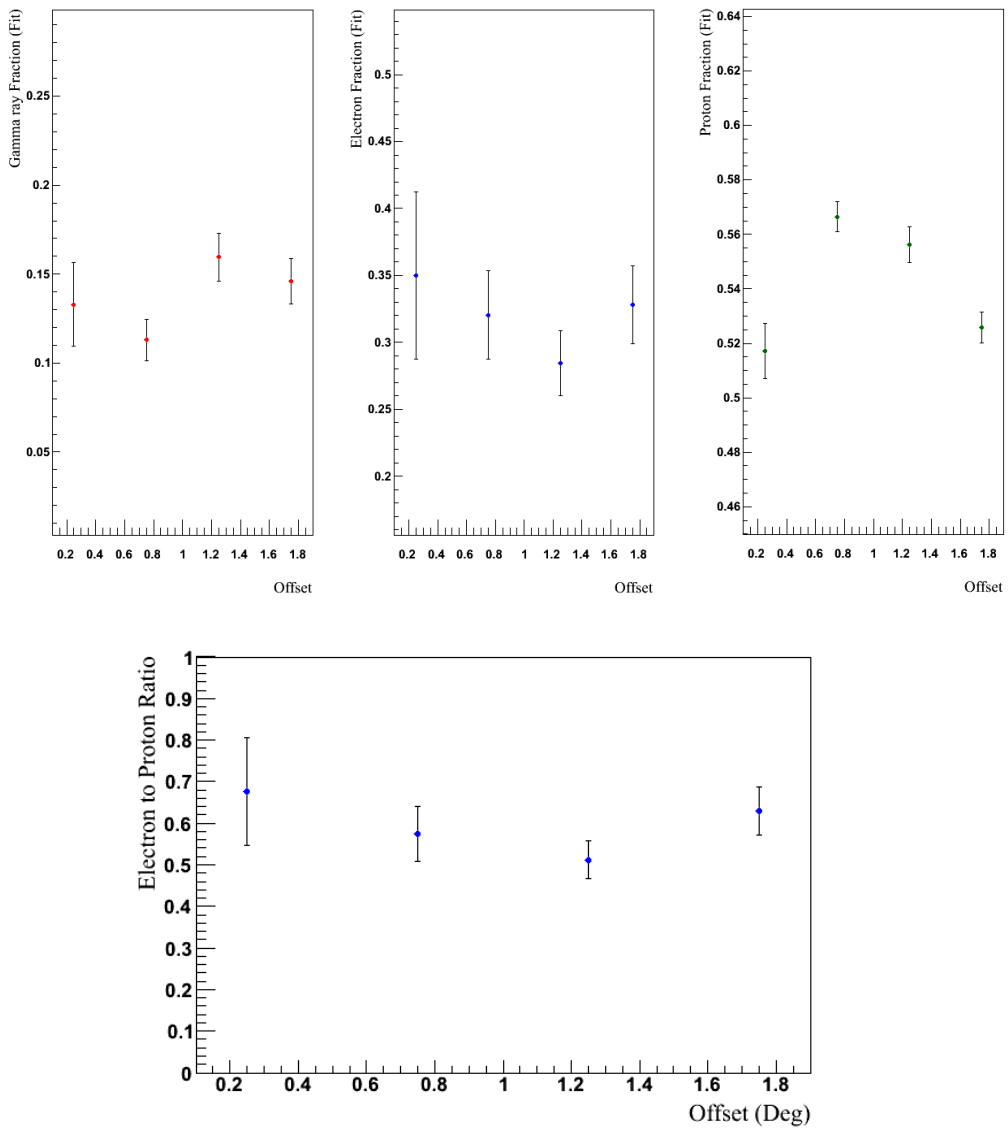

Figure 4.23: Electrons to protons ratio from the 2-dimensional analysis, fitted for four offset bins from 0 to 2 degrees. TOP: The estimated γ-ray, electron and proton fractions for the 3-dimensional linked analysis. The simulated data files contained 10% γ rays, 30% electrons and 60% protons in each offset band. The γ-ray, electron and proton components were fit in four offset bins: 0 - 0.5 degrees, 0.5 - 1 degrees, 1 - 1.5 degrees and 1.5 - 2 degrees. BOTTOM: Electron to proton value found for each offset bin in the 3D linked analysis. The true value is at 0.5.

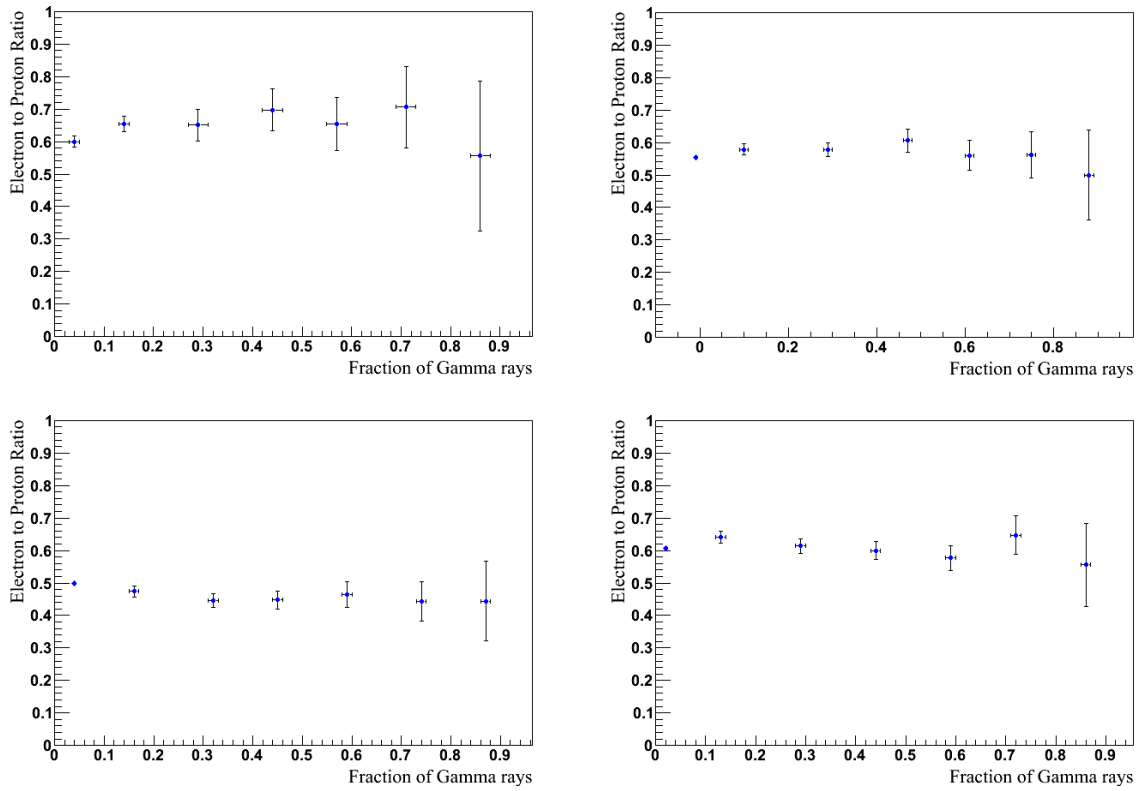

Figure 4.24: The fitted number of electron to proton events for all events taken in four different offset bins: 0 - 0.5 degrees (TOP LEFT), 0.5 - 1 degrees (TOP RIGHT), 1 - 1.5 degrees (BOTTOM LEFT), 1.5 to 2 degrees (BOTTOM RIGHT). The electron to proton ratio was fit for varying values of γ-ray fraction, shown on the x axis. In each offset bin, the true value of electron to proton events is 0.5.

pending on the exact variation in offset and the average of the distribution. With an increasing average offset, a decreasing electron to proton ratio will be fit with the exception of events between 1.5 and 2 degrees. This would also be the case if fitting values for extended sources at different offsets. When analysing point sources, non-diffuse γ-ray events coming from the source could be overestimated when analysing *on* regions due to the lower offset distribution of these events.

The uncertainty in the fitting procedure can be approximated in the 1D fit when limiting the range of offsets. For γ rays, electrons and protons this uncertainty is $\approx$ 10%, 7% and 6% respectively. In the 2D case this can be estimated as 6%, 4% and 7% respectively.

4.4 Conclusion

The three component fitting analysis described in this Chapter aimed to estimate the total contribution of γ ray, electron and proton events to simulated and real data. A background rejection of 65% is achieved for very γ-like proton events while keeping a γ-ray signal efficiency of 85%. Additionally, 37% of electrons are rejected while keeping 80% of the γ ray signal.

The method was tested on observations of the BL Lac PKS 2155-304. The method was performed as a 1D and 2D fit and in the energy range of 380 to 900 GeV. Values of the γ ray contribution in the *excess* distribution for both dimensions was found to be 100$\pm$1%. This is in agreement with the expected value, as the excess distribution is considered as representing the distribution of events coming directly from the source.

The fit was applied to observations taken off the source. The result was 3$\pm$4% of γ ray events in the 1D case and 7$\pm$1% in the 2D approach. The electron to proton ratio in the 1D (2D) approach is 0.45$\pm$0.05 (0.41$\pm$0.02).

Tests were performed on simulations to assess the accuracy of the method. Tests on the zenith angle range, fraction of γ ray contribution and offset range were carried out. The behaviour of the fit results performed better when selecting events in a zenith angle range of $\pm$5 degrees from the simulated value. The method is also dependent on the offset distribution and care would need to be taken when using this method to ensure data and simulations represent similar offset distributions. No trend in the variation of the fit result was found with an increasing γ-ray fraction.

An estimate on the systematic effect arising from the fitting procedure due to these

dependencies was given for γ rays, electrons and protons as 6%, 1% and 2% respectively. These values apply to the 2D approach. When limiting the offset, the uncertainty in the fit increases to 6%, 4% and 7% respectively and suggests that errors in measurements will be dominated by systematic effects.

Chapter 5

Scientific Results

The separation analysis discussed in Chapter 4 was applied to three scientific studies. As the method estimates the contribution of protons, electrons and γ rays, it is ideal for studies on diffuse emission where the FoV and the need for a separate background region are no longer limiting factors. The further suppression of the hadronic background and increased identification of electrons from γ rays enables measurements of weaker signals on large scales.

A study was performed on the latitude profile of the diffuse emission in the Milky Way. Two additional studies on the isotropic γ-ray background and cosmic electron spectrum were carried out.

5.1 Galactic Diffuse γ-ray Emission

A study on the γ-ray emission profile, including emission from known sources, was carried out. The fraction of the γ-ray contribution in two energy bands at 380 to 900 GeV and 1 to 3 TeV was determined. Previous measurements of the diffuse γ-ray emission in the galaxy is discussed in Section 5.1.2 and the motivation for this study is outlined in Section 5.1.3. The results are described in Section 5.1.7.

5.1.1 Origins

The origin of the Galactic diffuse γ-ray emission (independent of known sources) in the VHE regime is still unclear. Three processes are thought to contribute to the overall observed emission:

- **Hadronic cosmic ray interactions with target material** in the galaxy result in p-p collisions. Neutral pions are produced which then decay into two VHE γ-rays. The material with which the hadronic cosmic rays interact is made up mostly of atomic and molecular hydrogen.
- **Inverse Compton scattering of cosmic ray electrons** with radiation fields also result in VHE γ-ray emission. The cosmic ray electrons transfer energy to optical photons emitted from stars, the cosmic microwave background and infrared radiation from dust. It is expected that the radiation field density correlates to a certain extent with the matter distribution of the galaxy.
- **Unresolved sources** could contribute as a third component of diffuse VHE emission in the galaxy. Galactic sources can pass undetected either due to their extended emission being too large for the FoV of H.E.S.S. while other sources are not detected at the 5σ level because of their low flux.

The energy dependent level of each contribution to the overall observed VHE γ-ray flux is not well understood. This was a central question for a previous study done with H.E.S.S. (Abramowski et al. 2014) and is discussed further in Section 5.1.2.

5.1.2 Previous Measurements

The Galactic diffuse γ-ray emission has been probed before. Measurements in the HE and VHE regime have been made by EGRET (Hunter et al. 1997) and Fermi LAT (Ackermann et al. 2012b) among others. A previous measurement at TeV energies has also been carried out with H.E.S.S. (Abramowski et al. 2014).

In the previous H.E.S.S. study, the flux level of the Galactic diffuse emission from $\approx$100 GeV to a few TeV was determined. The predicted hadronic flux was compared to the latitude profile of the total γ-ray flux to find the relative contribution. It was concluded that the flux predicted from p-p interactions with the interstellar medium constituted $\approx$ 25% of the observed flux. This suggests that a large proportion of the signal stems from undetected γ-ray sources and / or inverse Compton scattering from CR electrons.

Additionally, the peak flux of the H.E.S.S. study was found to be centred on a latitude of b = -0.25°. Emission above a baseline of 1.2° in latitude was used to model the background. However, large scale emission might exist at $|b| > 1.2°$. Due to this limitation in background estimation, finding a true profile of the diffuse γ-ray emission was not possible.

Diffuse emission in the Galactic plane was also studied in the H.E.S.S. Galactic Plane Survey (HGPS), which used the standard H.E.S.S. analysis with an adaptive ring background to study the diffuse γ-ray emission (H.E.S.S. Collaboration 2016) (Deil 2011). Within each band of longitude, a Gaussian function was fit to the latitude profile of emission. The width found for longitudes of -30° < l < 40° varied between ≈ 0.2 and 0.45°. Due to the limited FoV and background subtraction method used, these values can be assumed as a lower estimate. The diffuse emission was studied in an energy range of 100 GeV to a few TeV in the HGPS and was carried out with the TMVA HAP analysis using the $hard\_zeta$ cut criteria (Ohm et al. 2009).

5.1.3 Motivation

How far in latitude the diffuse γ-ray emission in the galaxy extends provides an insight into which contribution might be the dominant process: hadronic, leptonic or unresolved sources.

The γ-ray emission originating from a hadronic scenario ($\pi^0 \rightarrow 2\gamma$) should be closely related to the distribution of atomic and molecular hydrogen target material in the galaxy. If we assume that the locally observed cosmic rays are isotropic, then the arising diffuse VHE emission should follow the target material with which the cosmic rays interact. The distribution of H_I within our galaxy has been measured in the Leiden/Argentine/Bonn (LAB) Survey (Kalberla et al. 2005) and more recently by the Effelsberg-Bonn Survey (Winkel et al. 2016). An overview of the H_I gas distribution in the Milky Way was presented in (Kalberla & Kerp 2009).

The mass distribution is dominated by gas in the plane of the Milky Way (Figure 5.1), though a proportion of gas flares to latitudes of $|b|$ > 20°. The flaring of the H_I gas extends higher at larger distances (R) from the Galactic Center, along the longitudinal direction. The average flaring half width half maximum (HWHM) rises from 0.1 to 2.6 kpc for 5 < R < 40 kpc (Kalberla & Kerp 2009). An exponential function and a mass model (Kalberla et al. 2007) can be used to describe the average flaring (Kalberla & Dedes 2008). The inner region of the galaxy (-30° < l < 40°) is studied in this Chapter, where there is a much less pronounced flaring in H_I than at the outer regions of the Milky Way.

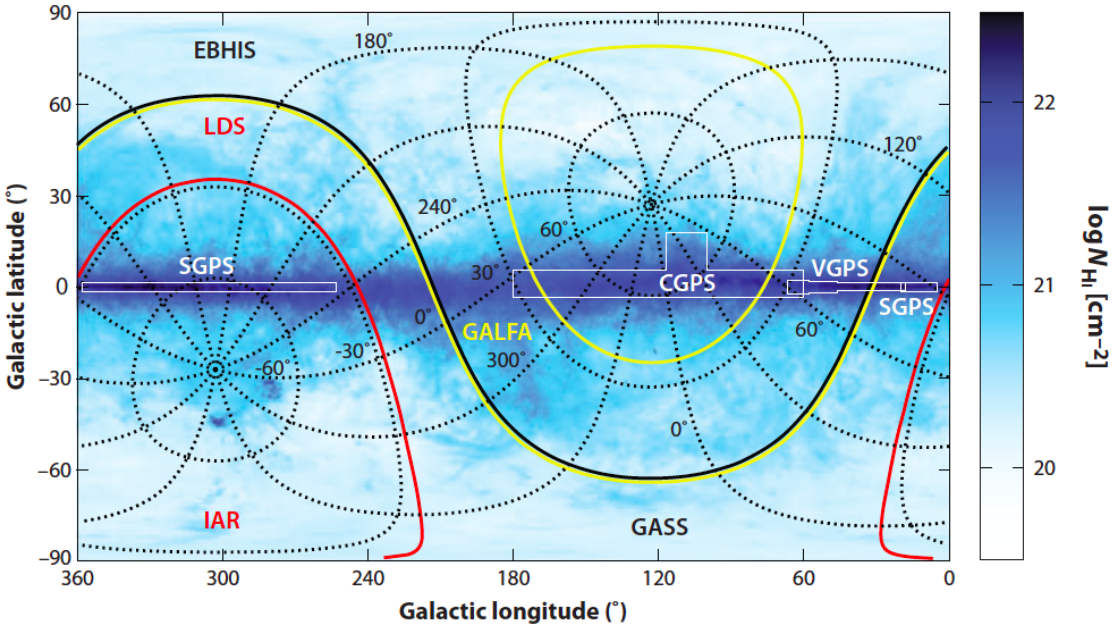

Figure 5.1: 21-cm line emission in the Milky Way, taken from the Leiden-Argentine-Bonn (LAB) survey. Several surveys cover different regions of the sky, depicted by coloured lines. The Leiden-Argentine-Bonn (LAB), Leiden-Dwingeloo Survey and Instituto Argentino de Radioastronom coverage is shown by the red lines. The Effelsberg-Bonn H_I Survey and Galactic All-Sky Survey cover the regions separated by the black line. Arecibo Galactic ALFA survey (yellow), Southern Galactic Plane Survey (SGPS), Canadian Galactic Plane Survey (CGPS), and VLA Galactic Plane Survey (VGPS) are also shown. This figure was taken from (Kalberla & Kerp 2009)

A previous estimate of the H_I column density distribution was found as a function of latitude and found to have a full width at half maximum (FWHM) of 4° (Dickey & Lockman 1990). The variation can be seen in Figure 5.2. This column density was measured over the entire Galactic plane.

As seen in Figure 5.2, molecular hydrogen is more concentrated along the plane of the Milky Way. A comprehensive overview of the H_2 distribution can be found in (Dame et al. 2001). A Gaussian having a FWHM of 87 pc ((Dame et al. 2001) Figure 12) - fit parallel to the plane of the Milky Way - was comparable to the H_2 distribution in latitude (Figure 5.2).

The γ-ray emission arising from a leptonic process should not necessarily correlate with the H_I and H_2 distribution. Although the density of photons within the galaxy is related to the distribution of matter, the photon fields extend to larger latitudes.

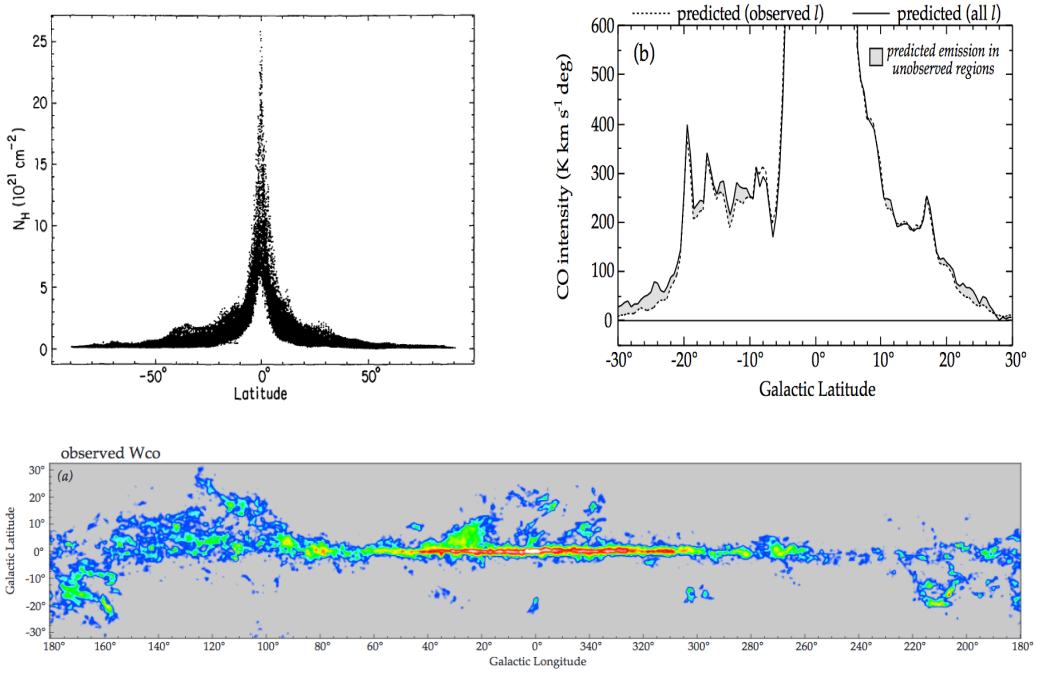

Figure 5.2: TOP LEFT: Variation of H_I column density with Galactic latitude (Dickey & Lockman 1990). TOP RIGHT: The CO intensity, used to trace Galactic H_2 regions, as a function of latitude within a longitude range of $0 < l < 360°$ (Dame et al. 2001). BOTTOM: The distribution of molecular hydrogen in the Milky Way (Dame et al. 2001).

The distribution of unresolved sources emitting VHE photons is, of course, unknown. Though, from the previous measurement made with H.E.S.S., it is expected that unresolved sources make a significant contribution.

The aim of this study is determining the width of the γ-ray emission in Galactic latitude and interpreting any implications. Essentially, this study aims to answer: What is the width in Galactic latitude of the γ-ray emission?

If the VHE γ-ray emission is found to correlate with the distribution of H_I and H_2 in the galaxy, then this is a strong indication that the emission in these regions is dominated by a

hadronic origin. In the case that emission is measured at larger latitudes, a leptonic scenario through inverse Compton scattering is likely at high latitudes.

As sources are included in this study, the γ-ray emission profile is compared to the known source distribution studied in the HGPS (Deil 2011). The γ-ray emission profile is also compared to studies of the diffuse emission in the HGPS. It is important to note that a different energy range was used in this study. The analysis was done on events falling in two energy ranges: 380 to 900 GeV and from 1 to 3 TeV.

This study provides an advantage in terms of background determination. The background and signal are estimated in the *same* region, allowing a more accurate determination of the hadronic and leptonic components involved. This is particularly useful in regions of extended and fully diffuse emission, as discussed further in Section 5.1.5.

The current analysis still faces challenges, however. Much less events are available to analyse than have been utilized in other studies with the H.E.S.S. telescope. The main reason for this is due to the strict zenith angle cut applied to the data, which was necessary as the simulated events were at one zenith angle of 20°. Another challenge is misclassification of events, which could potentially modify the results if the measured signal is weak in comparison the the background.

5.1.4 Data Selection

5.1.4.1 Latitude

Events were chosen for the analysis of the Galactic latitude according to selection criteria defined in Table 5.1. Events with a reconstructed energy of 380 < E < 900 GeV were were chosen for the lower energy band. A higher energy band of 1 to 3 TeV was also analysed and the same selection criteria applied. The energy bands were chosen to minimize any effects of the event weighting, as the electron spectrum is expected to have a cutoff energy of $\approx$ 1 TeV.

Only events having a telescope multiplicity of 4 were included. This was to ensure a more accurate energy and direction reconstruction and hence, a better background separation. Impact parameters of 0 to 280 m for all four H.E.S.S. I telescopes were considered. The impact parameter was restricted to improve the accuracy of the event reconstruction. Additionally, simulations were generated with an impact parameter of less than 300 m to minimize computational time.

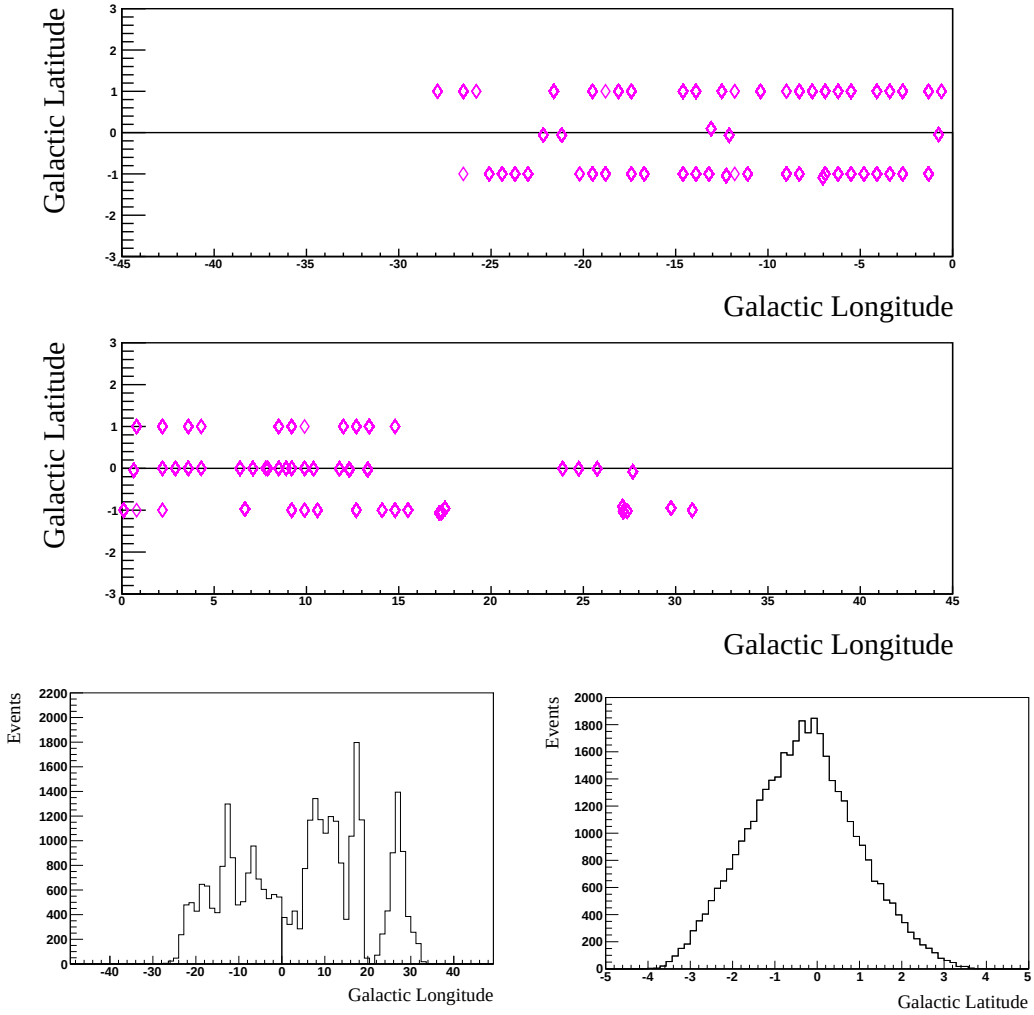

Figure 5.3: The position in Galactic longitude and latitude of observation runs used to study the latitude profile of the diffuse γ-ray emission. BOTTOM: Data events used in the latitude profile study after selection cuts as a function of Galactic longitude (LEFT) and Galactic latitude (RIGHT). Data passing TMVA HAP *standard_zeta* cuts were selected on their energy, impact parameter, telescope multiplicity and zenith angle, summarized in Table 5.1.

The reconstructed zenith angle of events is restricted to values of 10° to 25°. Runs were included if their observation position was at three distinct latitudes (b): -1±0.1°, 0±0.1°, 1±0.1°. This is discussed further in Section 5.1.7. As almost all events were contained within a region of -30° < l < 40°, a cut was placed to ensure no events outside of this region were included.

This criteria greatly reduced the number of available observation runs, shown in Figure 5.3. The event distributions are also shown, with data events confined to latitudes of -4° < b < 4°. Further criteria for the latitude and longitude analysis is outlined in the relevant sections.

Analysis	Parameter	Cut Value
Latitude	Impact Parameter	< 280 m
	Telescope Multiplicity	4
	Offset	< 2°
	Zenith Angle	10° - 25°

Table 5.1: The parameter cuts used in the analysis of the latitude profile of the diffuse γ-ray emission in the Milky Way. The cut criteria apply to both energy bands - 380 to 900 GeV and 1 to 3 TeV - used in the latitude analysis.

5.1.4.2 Longitude

Figure 5.4 shows the runs and events selected for the analysis of the longitude emission profile. The events shown are after the event selection is made, with the cut criteria summarized in Table 5.2.

More runs were selected for the longitude analysis as the selection was not restricted to runs with a specific position in latitude, as was the case in the latitude analysis. A specific position in Galactic longitude was not necessary, as large bin widths were chosen to minimize the effect of the offset dependence.

The event simulations used in the fitting procedure were produced at one zenith angle of 20°. Therefore, a cut in zenith angle of 16 to 24° was made. This range is different to the one stated for the latitude analysis in order to keep the average zenith angle at 20±1°. Only events that passed the cut on the $standard\_zeta$ variable of the TMVA HAP analysis (Ohm et al. 2009) were fit to ensure a high level of hadron rejection while still keeping a good γ-ray signal efficiency. This was important to ensure the background components were at a comparable level, improving the fit.

All data and simulations used in this study were taken in the phase1b state, corresponding to data taken from May 2004 to July 2007 and an optical efficiency of 70%. Only the

H.E.S.S. I telescopes were involved in this study.

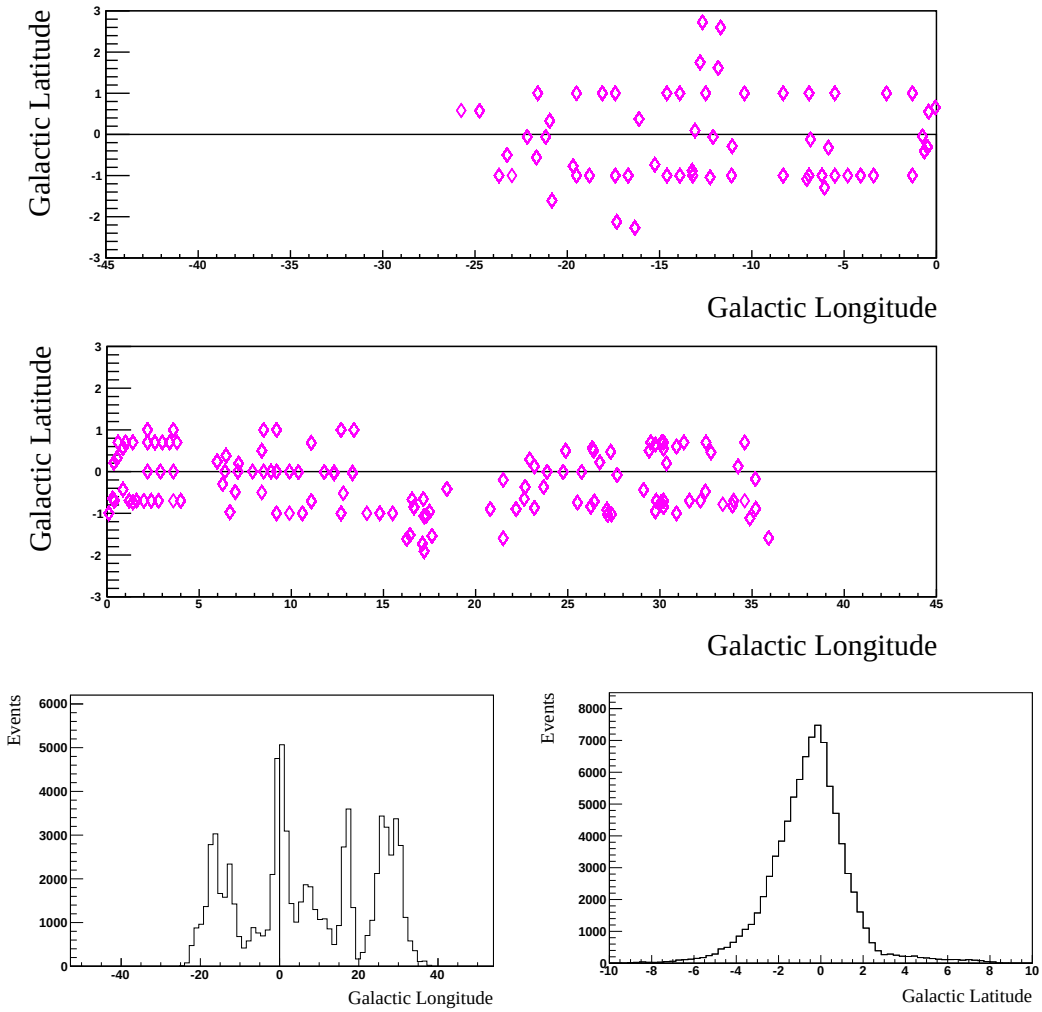

Figure 5.4: TOP: The position of observation runs used to study the longitude profile of the Galactic diffuse γ-ray emission. BOTTOM: Data events used in the longitude analysis as a function of Galactic longitude (LEFT) and Galactic latitude (RIGHT). Data events have passed TMVA HAP *standard_zeta* cuts and the selection criteria outlined in Table 5.2.

Analysis	Parameter	Cut Value
Longitude	Impact Parameter	< 280 m
	Telescope Multiplicity	4
	Offset	< 2°
	Zenith Angle	16° to 24°

Table 5.2: The parameter cuts used in the analysis of the longitude profile of the diffuse γ-ray emission in the Milky Way. The cut criteria apply to energies of 380 to 900 GeV.

5.1.5 Background Determination

Measurements of diffuse and extended emission is difficult to analyse with IACTs. This is due to the high level of background contamination from both protons and electrons and the limited FoV. The background separation method discussed in Chapter 4 was used to determine the background and to estimate the γ-ray contribution of the diffuse γ-ray emission in the galaxy. The advantages of using this method are outlined below:

- **Better γ-hadron separation** to extract a weak signal. Diffuse γ-ray emission has a weak signal compared to the background contribution of cosmic rays. Hence, a more powerful separation is needed to improve the γ-ray detection. Figure 4.2 shows the further separation power achieved of proton events currently accepted as γ rays. This extra separation enables a weaker signal to be detected.
- **Separation of γ rays and electrons** (Figure 4.2) provides identification of the remaining background component. After current hadronic rejection cuts, the remaining electron component becomes comparable to the hadronic background. No identification of electrons is currently made.
- **All contributions are estimated in the *same* region at the *same* time**. To detect a signal with current background methods, a background region should be defined within the FoV. If the diffuse emission is not fully contained in the FoV, then a defined background region could potentially contain part of the diffuse signal. The advantage of the method presented in Chapter 4 is that having a background region is not necessary, as the γ-ray and the two remaining background components - electrons and protons - are directly estimated in the *same* region. This simplifies the background estimation and provides a non-region dependent estimate of the γ-ray signal.

These advantages apply to studies on diffuse emission. When carrying out studies on sources contained within the FoV, a determination of the background using an *off* source region - as with current background estimation methods - has a superior performance.

The background technique was applied to events that pass TMVA HAP *standard_zeta* cut criteria, so that the fitting procedure could be applied to similar levels of each contribution. The PMBg Background Method (Marandon 2010) was used in this study to ensure the full distribution of offsets within the FoV were kept.

5.1.6 Galactic Sources

As discussed in section 4.3, the results found from testing the analysis on simulated data showed a strong dependence on the offset distribution. It is very important that, firstly, the offset distribution of the simulated events accurately represents the event offsets in the data.

Although including known sources in the data would shift the offset distribution of the γ-ray component, the electron and proton contributions should not be effected. If sources were excluded, the offset distributions from all three contributions - γ rays, electrons and protons - would change. For this reason, no exclusion of Galactic sources was applied in this analysis.

Fortunately, this does not implicate the weighting of the diffuse emission, as the average spectral index of known H.E.S.S. sources (Γ = 2.3) is the same index used to model the diffuse emission (H.E.S.S. Collaboration 2016).

Although exclusion regions were not applied to this dataset, HESS J1825-137 and HESS J1826-148 were excluded due to their strong signal at high latitudes. To ensure the offset distribution was not effected, every event detected between 16 < l < 19° was removed. As a result, sources HESS J1826-130 and HESS J1813-126 were also excluded.

5.1.7 Latitude Analysis

Properties of Data

When analysing the latitude emission, a criteria was chosen that each bin in latitude must have a minimum number of events of N_{events} > 500. Along with other cut criteria (Table 5.1), this further limited the latitude region analysed to -2.7 < b < 2.1° where b denotes the Galactic latitude. A binning was chosen as a compromise between the number of events and the fit accuracy, resulting in a binning of 0.3° in latitude.

The strong dependence of the analysis method on the offset distribution has to be considered. This dependence makes it an important factor in deciding two points in the analysis:

- Exclusion of known sources will effect the offset distribution if applied to the data. For this reason, only one exclusion *band* was applied. Excluding a *band* rather than a *region* preserves the range of offsets for the electron and proton contributions. Therefore, all events between 16 < l < 19°, at all latitudes, were not included. This particular *band* was excluded as it contained the sources HESS J1825-137 and HESS J1826-148 that are known to have significant γ-ray emission at latitudes b < -1°.
- The observation position should be fixed in latitude. To ensure as many events as possible were included, three fixed observation positions were used: -1°, 0° and 1° in Galactic latitude.

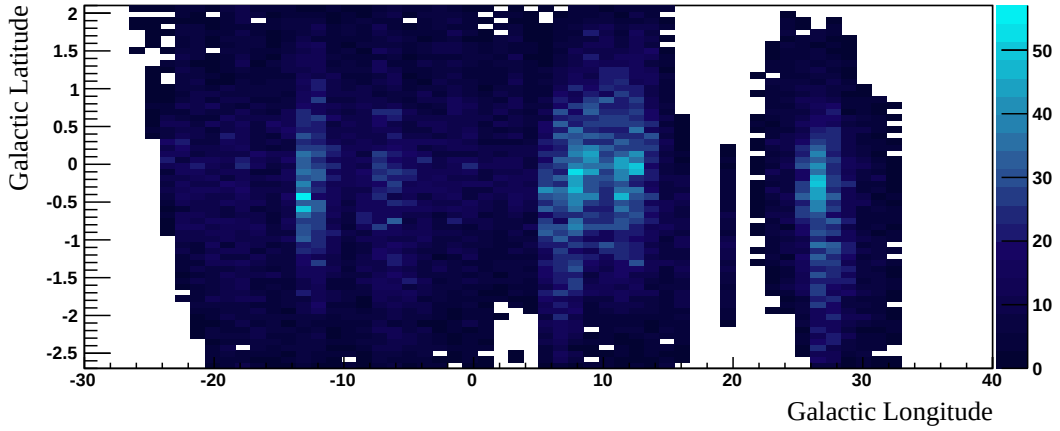

Figure 5.5: Events included in the analysis of the Galactic latitude profile. Events were taken over a region of -30° < l < 40° and -2.7 < b < 2.1°. Events between 16 < l < 19° were excluded due to strong emission of sources far from b = 0°.

Both of these points could severely limit the number of events or change the offset distribution. Though the added γ-ray emission from known sources could still effect the offsets observed from diffuse events, the advantage of not excluding source regions is so the offsets observed from electron and proton events are not effected, assuming their emission is truly diffuse. Selecting observation runs according to fixed latitude positions enables similar distributions of offset for simulated and real events to be chosen.

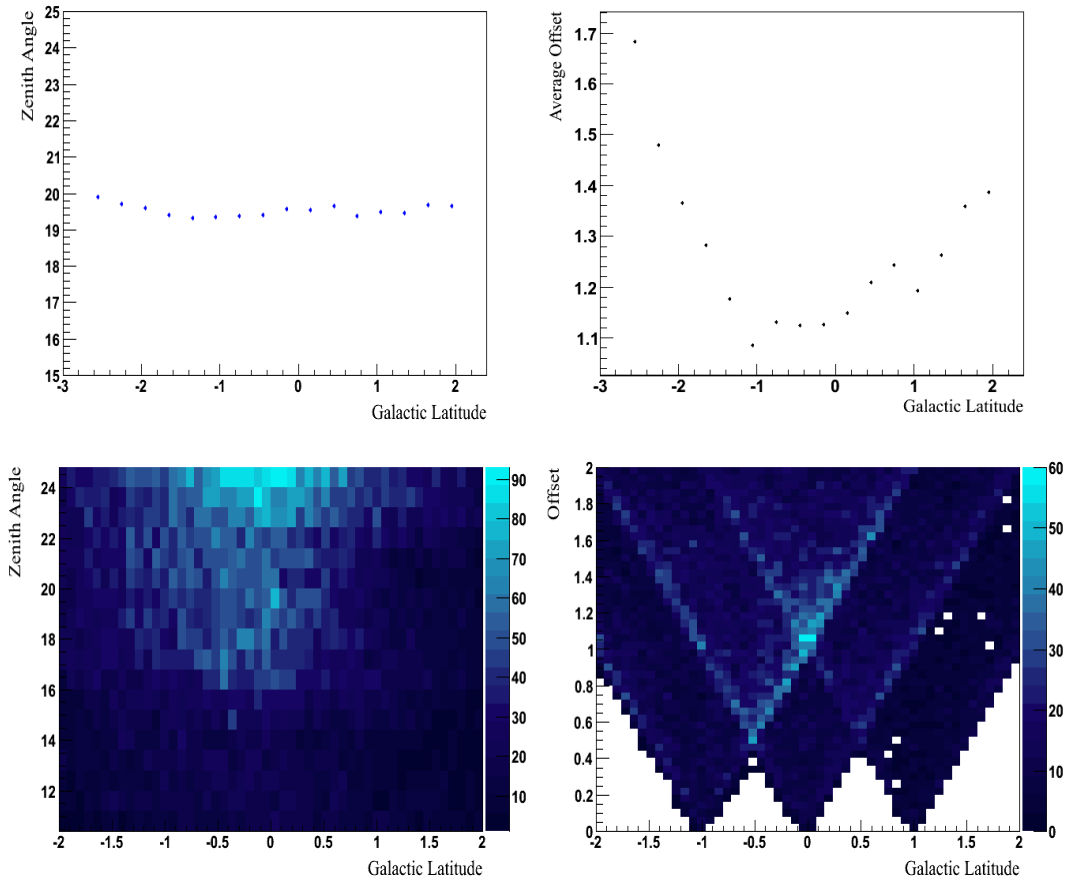

Figure 5.6: BOTTOM LEFT: The reconstructed zenith angle distribution used in the analysis as a function of Galactic latitude. TOP LEFT: The average reconstructed zenith angle of the Galactic dataset found within each latitude bin. BOTTOM RIGHT: The offset distribution as a function of Galactic latitude. TOP RIGHT: The average offset for each bin in latitude.

The analysis uses a large energy band and so care should be taken when weighting the different contributions, as minor changes in one of the spectral indices can lead to a higher inaccuracy in the fit. The simulated electron events are weighted according to the electron spectrum. Similarly, the simulated proton events are weighted to the same spectral index as the cosmic ray spectrum.

The weighting of events is especially important when considering the γ-ray component. Emission from resolved sources as well as the total diffuse component both contribute to the

observed γ-ray emission. Hence, choosing the correct spectral index in the case of γ-rays is more complex, as different types of emission have different levels of contribution. However, the average spectral index of known sources in the Galactic disk is $\Gamma = 2.3$ (H.E.S.S. Collaboration 2016) and the diffuse emission in the central part of the galaxy has been determined as $\Gamma = 2.3 \pm 0.1$ (Lemiere et al. 2015). This value is used to model the overall γ-ray emission in this analysis.

Two Types of Fitting

For this study, the separation technique outlined in Chapter 4 was used. The 2D method was used to fit the observational data. The dataset was fit in two different ways, outlined below:

- Approach 1: The γ-ray, electron and proton components were each allowed to vary between -100% and 100%. A condition was placed that the total sum of the γ-ray, electron and proton fractions must be equal to 100%.
- Approach 2: The values of each of the three components were limited to between 0% and 100%. This was to minimize any misidentification of events that might be present. Again, only combinations of fractions that added up to 100% were fit.

Due to the known source population in the inner part of the galaxy, at high latitudes the γ-ray fraction should tend to lower values than at $b = 0$. As all three components - γ-ray, electron and proton events - are fitted simultaneously, it is very difficult to predict where any misclassification occurs and the degree to which it occurs. The effect of the wide range of zenith angle and confounding variables from analysing real data cannot be accounted for.

As there are many similarities between electron and γ-ray events, one would expect a certain amount of γ-ray events being categorized as electron events or conversely, electrons as γ rays. For this reason, taking Approach 2 and limiting the possible fractions being fit to between 0% and 100% allows a lesser degree of potential misclassification and a more accurate estimate at higher latitudes. Therefore, the discussion in this section applies to results obtained with Approach 2.

γ-ray Profile

380 to 900 GeV

The γ-ray fraction found across the Galactic latitude is shown in Figure 5.7. The profile was fit with a Gaussian function plus an offset, which was left as a free parameter. The γ-ray fraction tends to zero at higher latitudes. It is important to keep in mind that the γ-ray contribution may be under or overestimated due to existing biases.

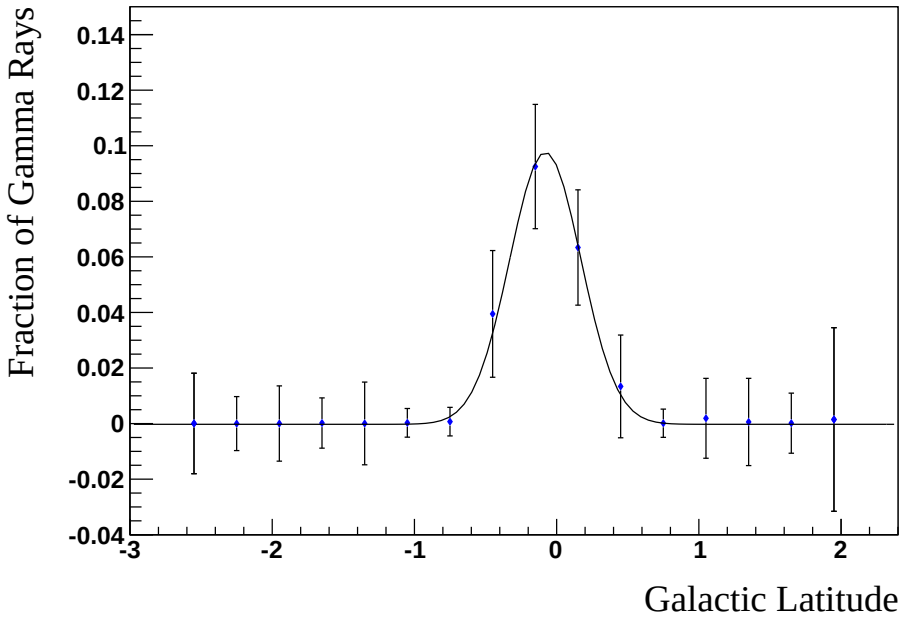

Figure 5.7: The fraction of γ-ray events across the Galactic latitude. The 1σ errors are also shown. Data were analysed at Galactic longitudes of -30 < l < 40°, with the exception of events between 16 < l < 19°.

The standard deviation of the fit is 0.25±0.05° and the χ^2 value is 0.29. The full width at half maximum (FWHM) is 0.59±0.12. The fit results are summarized in Table 5.3. The mean of the emission is not centred at b = 0 but rather at b = -0.08±0.06. This is not surprising as the known sources (H.E.S.S. Collaboration 2016) are not homogeneously distributed, with more sources detected at negative latitudes.

An energy range of 380 < E < 900 GeV was used. In addition, the selected runs are in the inner part of the Galactic plane (-30 < b < 40°). The distribution of the H_I target material is less flared in this region and a narrower γ-ray profile expected.

1 to 3 TeV

The latitude profile was analysed in an energy range of 1 - 3 TeV. The cut criteria applied to the data is summarized in Table 5.1. No criteria for the number of events were defined. The average zenith angle was restricted to 20±1° for each bin in latitude. The weighting applied to this energy range differed as the cosmic electron spectral index changed. As in the lower energy range of 380 to 900 GeV, proton events were weighted according to the locally measured cosmic ray spectrum, Γ = -2.7, γ-rays according to the average index of Galactic sources, Γ = -2.3 and electrons with a index of -4.1 (Aharonian et al. 2009).

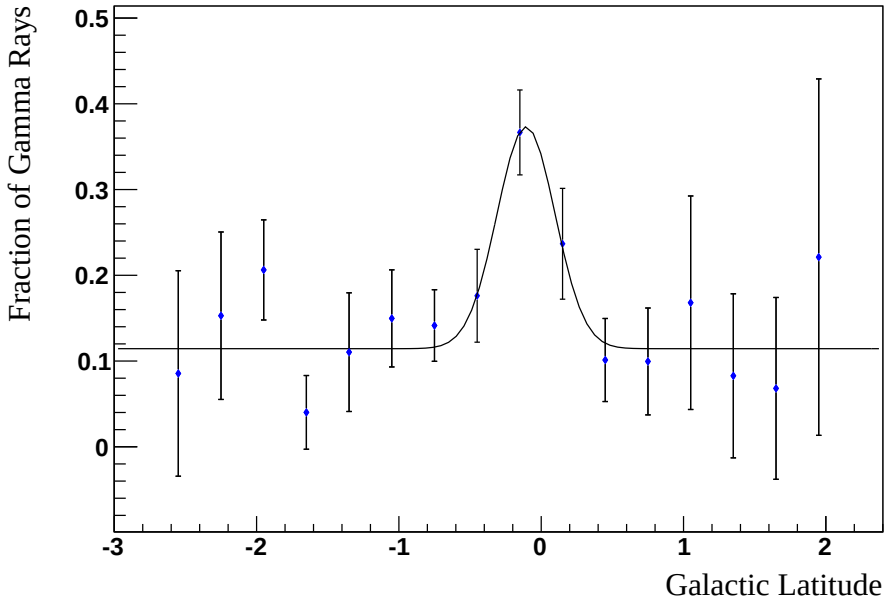

Figure 5.8: The fraction of γ-rays as a function of Galactic latitude for events between 1 and 3 TeV. Data were analysed at Galactic longitudes of -30° < l < 40°, with the exception of events between 16 < l < 19°.

Figure 5.8 shows the γ-ray profile in Galactic latitude. As expected, the γ-ray fraction increases towards latitudes of b = 0. The values of the γ-ray fraction are higher than those found at 380 to 900 GeV (Figure 5.7). This is expected as the background rejection increases at higher energies. The profile was found to have a Gaussian width of σ = 0.20±0.06° and a χ^2 value for the fit of 7.4. The FWHM is 0.47±0.14°. This is compatible within errors with the width of σ = 0.25±0.05° for events between 380 and 900 GeV. Details of the fit results are shown in Table 5.3.

Profile	Energy (TeV)	mean (°)	σ (°)	FWHM (°)	Offset	χ^2
γ-ray	0.38 - 0.9	-0.08±0.06	0.25±0.05	0.59±0.12	-2.6±27.2×10^{-4}	0.29
	1 - 3	-0.11±0.07	0.20±0.06	0.47±0.14	0.11±0.02	7.4

Table 5.3: Summary of the widths (σ) of the γ-ray latitude profile. The profile was fit with a Gaussian plus an offset or shift. The FWHM of the profile, mean latitude and χ^2 value of the fit are also shown.

Electron, Proton and e/p Profiles

380 to 900 GeV

Electron and Proton Latitude Profiles

The estimated fraction of electrons and protons across the Galactic latitude can be seen in Figure 5.9. As the γ-ray fraction increases towards $|b|$ = 0, the percentage of background in the dataset is expected to decrease. This correlation can be seen in the decreasing proton fraction towards smaller latitudes. The electron fraction shows no tendency to decrease at smaller latitudes. However, this decrease should not necessarily be noticeable if it is comparable to the 1σ or systematic errors. The systematic errors are not taken into account.

If the electron estimate is, in fact, higher than the true value, there could be two possibilities. Either the estimated γ-ray fraction is not high enough (γ-ray to electron misidentification) or that the proton fraction estimate is too low (proton to electron misidentification).

Comparing results of the two approaches (see Section 5.1.7) gives an indication of where biases may exist. Both estimates of the proton fraction are similar in Approach 1 and 2. The estimated electron fractions, however, are different. If the allowed fractions for each component are restricted to positive values (Approach 2), the γ-ray fraction increases at latitudes $|b| > 0.75$. Subsequently, the electron fractions are estimated at lower values. This indicates that there is a certain amount of misclassification between γ-ray and electron events.

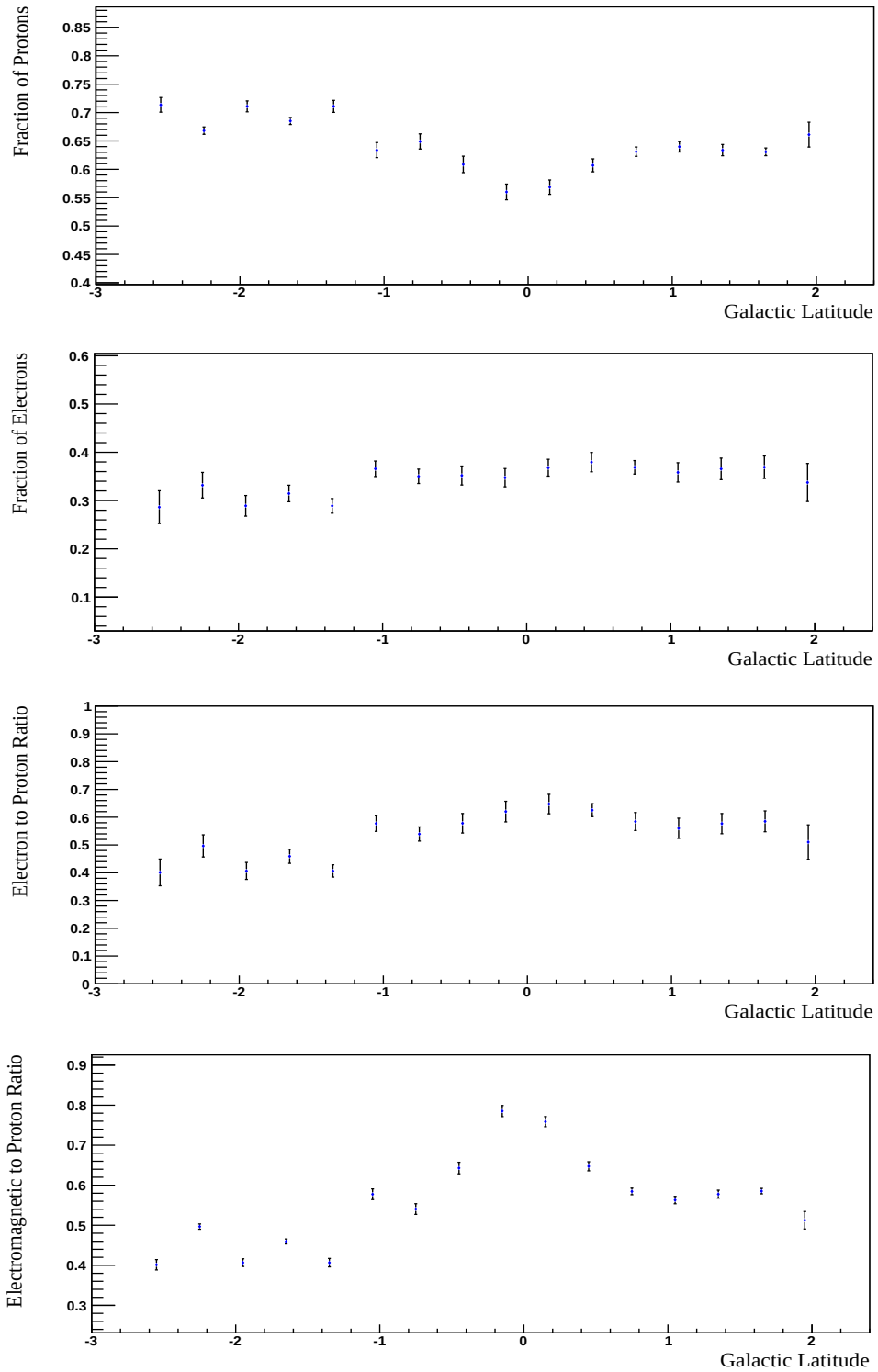

Figure 5.9: Estimated fraction of protons (first panel) and electrons (second panel) as a function of Galactic latitude. The corresponding e/p ratio (third panel) and the ratio of electromagnetic (electrons and γ rays) to proton events (fourth panel) are also shown. The estimates were obtained using the 2D analysis. Events between longitudes -30° < l < 40° were included, except for events that fell between 16 and 19° in Galactic longitude.

Electron to Proton Ratio

If we assume the cosmic electron and proton flux is truly isotropic within this energy band, then the electron to proton ratio should remain constant at all latitudes. Figure 5.9 shows the electron to proton ratio as a function of Galactic latitude.

Another factor to consider is the misidentification of one particle species as another. At smaller latitudes towards b = 0, the γ-ray flux increases, along with a potential for misclassification.

The e/p ratio does not vary much throughout the latitude profile, although the averaged value ($\approx$ 0.54) from all latitude bins is higher than that fitted in the larger region of -30 < l < 40° and -10 < b < 10° of 0.49±0.02. The value found is higher than the electron to proton ratio found in the 2D analysis of PKS 2155-304 (Section 5.2) of 0.41±0.02.

The higher value of e/p shown may be due to an overestimation of the electron fraction. If there is misclassification between electron and γ-ray events, as the γ-ray fraction increases towards b = 0 so will the potential misidentification. This could lead to an overestimation of the electron component at smaller latitudes and a higher prediction of the e/p ratio.

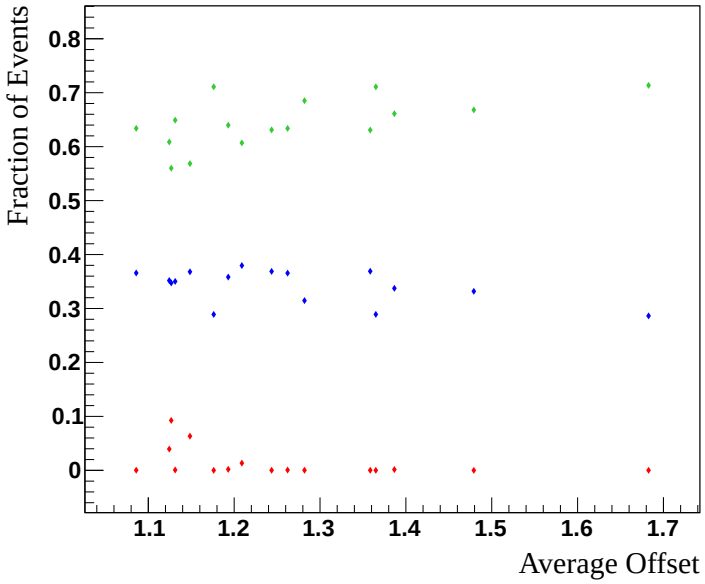

Figure 5.10: The average offset per latitude bin against the fitted fraction of γ-rays (red), electrons (blue) and protons (green).

Another factor to consider is whether the fit results correlate with offset. The correlation factors between offset and fitted fraction (Figure 5.10) was found. The fraction of γ rays has a negative correlation factor of -0.49, electrons have a correlation factor of -0.14 and protons are positively correlated with offset at 0.64. The consistent value of e/p found in the latitude profile also concludes that no anisotropy of electrons or protons was found on a 0.3° scale in this energy range.

Electromagnetic to Proton Ratio

Due to the potential misidentification of events, including misclassification between γ-ray and electron events, the ratio of electromagnetic induced events to proton initiated events eliminates the necessity of distinguishing between all electron and γ-ray induced air showers.

The number of electromagnetic (γ-ray and electron events) to proton events is shown in Figure 5.9. As the electron to proton ratio is shown to be constant between 380 and 900 GeV, the latitude profile of all electromagnetic to proton events gives a further estimate of the width of the γ-ray emission profile.

A Gaussian with an offset was fit to the profile of electromagnetic to proton events. The offset was found to have a value of 0.52±0.004. The width is σ = 0.44±.02° and the FWHM is 1.04±0.05. This is larger than the width of the γ-ray profile (σ = 0.25±0.05).

1 to 3 TeV

Electron and Proton Latitude Profiles

The fraction of protons and electrons across the Galactic latitude is shown in Figure 5.13. The proton fraction between 1 and 3 TeV decreases at latitudes closer to b = 0, while the electron fraction remains constant, within errors.

Electron to Proton Ratio

The electron to proton ratio is shown in Figure 5.12. The values of e/p at lower latitudes is high compared to the extragalactic value found in the analysis of PKS 2155-304 (e/p=0.41±0.02) and Centaurus A (e/p=0.39±0.07). This might be due to the γ-ray composition being underestimated and the electron one overestimated when fitting large contributions from three, rather than just two, components. The resulting electron to proton ratio

shows a rising e/p value towards b = 0. Assuming electrons and protons enter the atmosphere isotropically, the expected electron to proton ratio should have the same value at all Galactic latitudes. There are several reasons that could lead to the symmetric profile seen in this higher energy band:

- **Misclassification** of γ-ray events as electron events. If this was the case, the electron profile should follow the γ-ray profile closely. The width of the e/p profile is σ = 1.4±0.67° and the fitted offset value is 0.21±0.03. The χ^2 of the fit is 5.3. More details on the fit results are found in Table 5.4.

  The different values for the width of the γ-ray and e/p profile does not indicate that the structure seen in e/p arises from misclassification between electron and γ-ray events. However, the changing electron fraction between Approach 1 and Approach 2 at 380 to 900 GeV does suggest that misidentification between the EM events does occur to some degree.

  Another possible channel is proton images being misclassified as electron images. If so, the proton fraction should correlate with the e/p profile. The width of the proton profile is 0.65±0.15, which is consistent with the estimated width of the electron to proton ratio, and so, this channel is not ruled out.

  Misidentifying proton events as γ-ray events is a third channel that could lead to the structure seen. An increasingly underestimated fraction of protons towards b = 0 would cause the increase seen in e/p. The γ-ray and proton profiles have been fit with widths of σ_γ = 0.20±0.06 and σ_p = 0.65±0.15 respectively, which are not consistent. Of course, a similar width is naturally expected as the background component of protons should decrease with increasing γ-ray fraction, therefore this type of misidentification can not be excluded.
- The **Offset dependence** of the fit result is discussed in Chapter 4. The electron to proton ratio decreases with increasing offset and rises again for events between 1.5 and 2°. As events with a reconstructed source position falling on a certain $slice$ of the camera were selected, the full range of events between 0 and 2° in offset were not used in the analysis. As the limited offset range could skew the result, events taken at three different observation positions were used to minimize the effect on the fit.

  The average offset for each latitude bin is shown in Figure 5.11. The correlation factors between offset and each component were found, with the fraction of γ rays having a negative correlation factor of -0.36. Electrons are also negatively correlated

with offset at -0.35 and protons positively correlated at 0.65. Although each component shows some degree of correlation with offset, the average offset value varies with latitude (Figure 5.11). The average offset is not symmetric at zero, making this an unlikely reason for the variation seen in the e/p profile.

- **Anisotropy** of electrons in the Galactic latitude may be considered as a possible origin of the structure in the e/p profile. Due to the interstellar magnetic fields, the directions of travel of cosmic rays are randomized by the time they reach Earth. If electron anisotropy were observed, an accelerator would have to be in the local vicinity of Earth. However, this inconsistency in arrival directions would be measured as dipole anisotropy. Models predict very small values of asymmetry - out of the scope of this analysis. Furthermore, no dipole anisotropy within the uncertainty range at energies of 60 to 480 GeV was measured with Fermi LAT (Ackermann et al. 2010b).

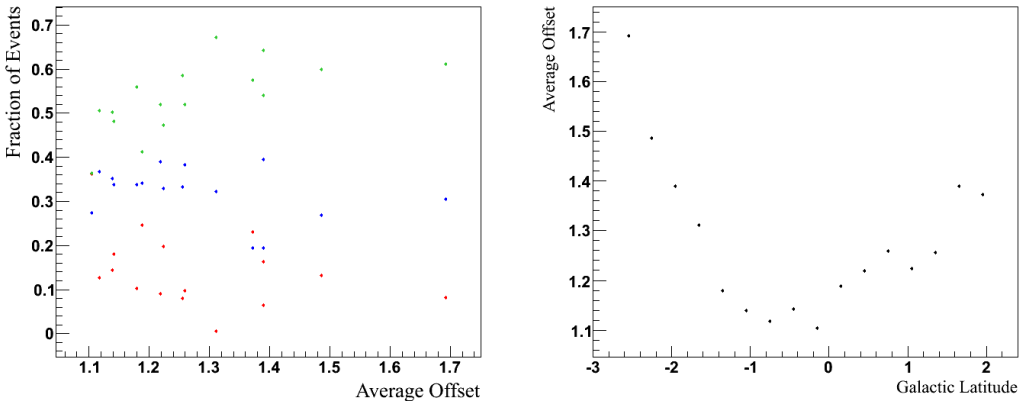

Figure 5.11: LEFT: The average offset per latitude bin against the fitted fraction of γ-rays (red), electrons (blue) and protons (green). RIGHT: Average offset within each latitude bin against latitude.

Electromagnetic to Proton Ratio

The ratio of electromagnetic (γ ray and electron) events to proton events (em/p) is shown in Figure 5.12. The profile has a width of σ = 0.30±0.03 and a FWHM of 0.71±0.07. The width is larger than the γ-ray profile. The offset of the Gaussian is at 0.77±0.02.

Profile	Energy (TeV)	mean (°)	σ (°)	FWHM (°)	Offset	χ^2
γ-ray	0.38 - 0.9	-0.08±0.06	0.25±0.05	0.59±0.12	-2.6±27.2×10^{-4}	0.29
	1 - 3	-0.11±0.07	0.20±0.06	0.47±0.14	0.11±0.02	7.4
e/p	0.38 - 0.9	-	-	-		
	1 - 3	0.19±0.24	1.4±0.67	3.30±1.58	0.21±0.30	5.3
em/p	0.38 - 0.9	0.05±0.01	0.44±0.02	1.04±0.05	0.52±0.004	860.6
	1 - 3	-0.09±0.01	0.30±0.03	0.71±0.07	0.77±0.02	227.4

Table 5.4: A summary of the widths (σ) found when fitting the γ-ray latitude profile and the electromagnetic to proton (em/p) latitude profile with a Gaussian function. The width of the electron to proton ratio (e/p) is also shown.

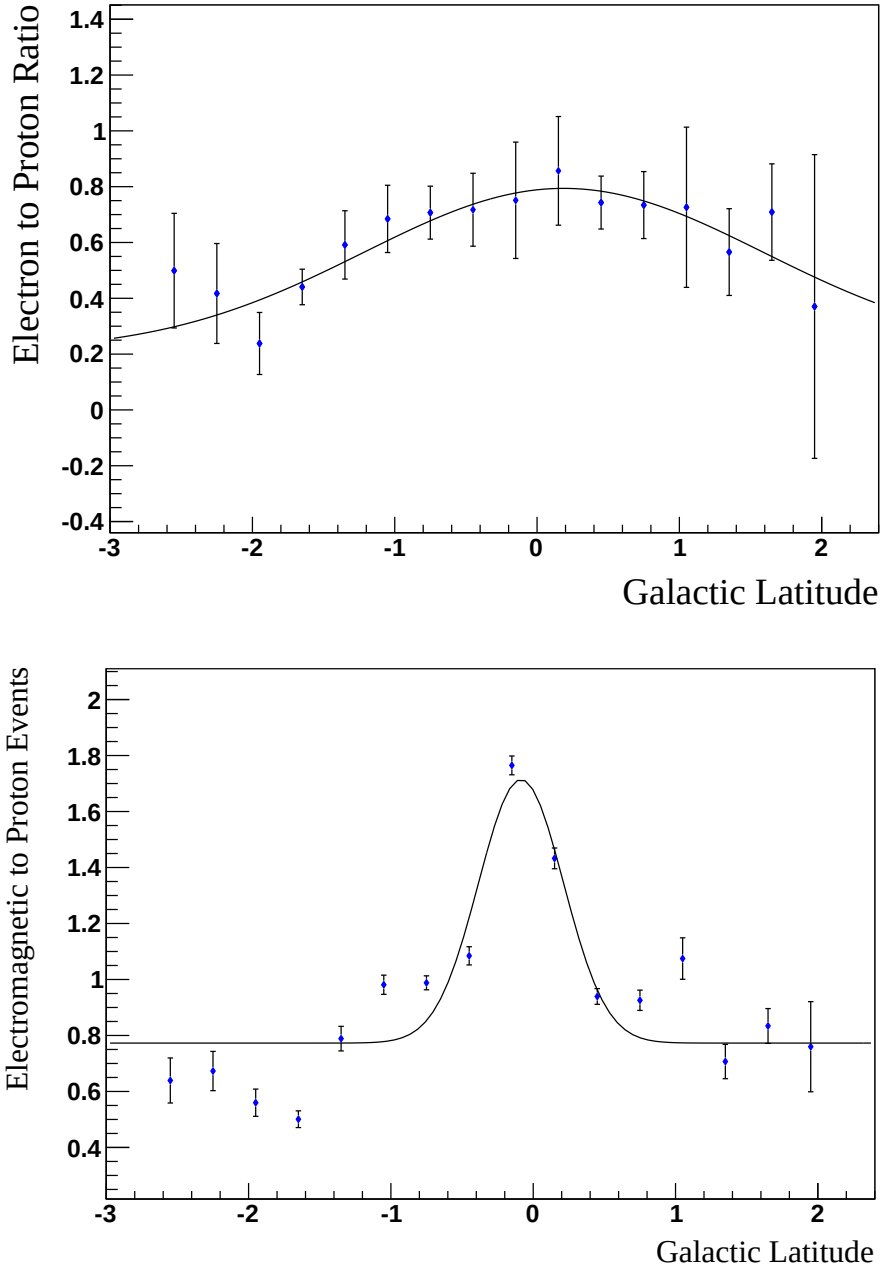

Figure 5.12: TOP: The number of electron to proton events for each bin in Galactic latitude. BOTTOM: The number of electromagnetic to proton events as a function of Galactic latitude. All events were contained within a longitude range of -20 < l < 16° and 19 < l < 30°.

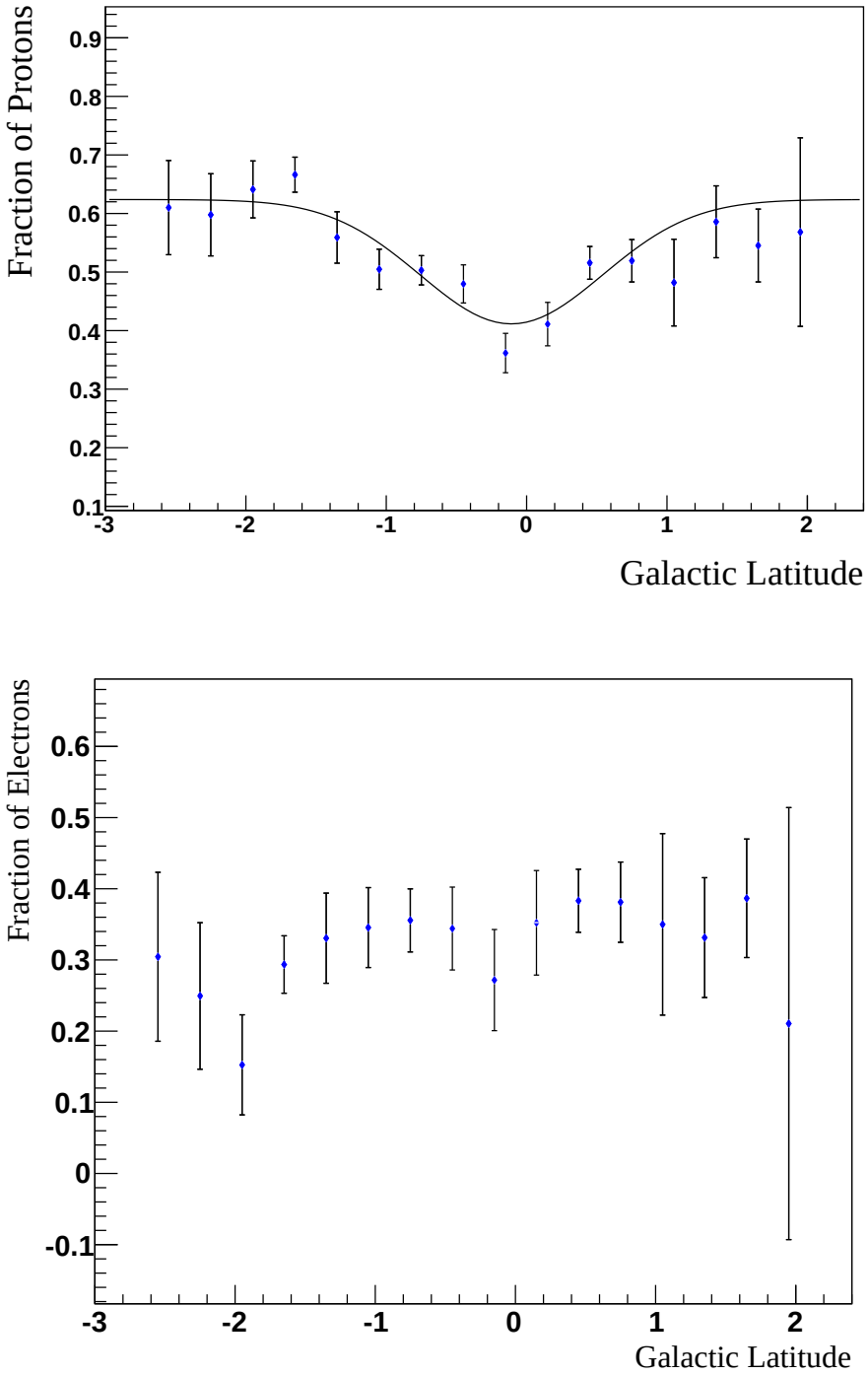

Figure 5.13: Estimated proton (top) and electron (bottom) fractions with Galactic latitude. All profiles included events in the longitude range of -20 < l < 16° and 19 < l < 30°.

5.1.8 Longitude Analysis

Applying the analysis to the longitudinal direction provides a further insight into the behaviour and accuracy of the method. All fractions of γ-ray, electron and proton components stated represent the fraction of events that pass the cut criteria. No exclusion regions were applied.

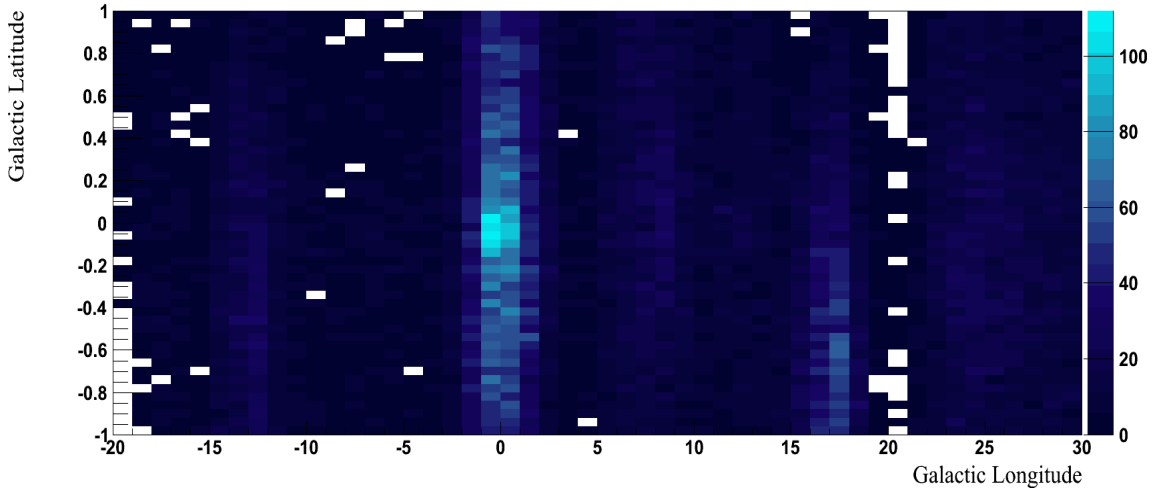

Figure 5.14: Events included in the longitudinal analysis of the Galactic diffuse γ-ray emission. Events were taken over a region of -20 < l < 30° and -1 < b < 1°.

One of the challenges involved in the analysis is the limited number of events left after the strict zenith angle cut. Figure 5.14 shows the distribution of events in the Galactic plane. Events were analysed between -20° < l < 30°. No criteria for the position of observation runs were applied. Table 5.2 summarizes the parameter cuts placed on the dataset.

As the simulations available are at a zenith angle of 20 degrees, the zenith angle cut for each longitudinal bin was varied to ensure the data had an average zenith angle of 20±1°. The lowest (highest) zenith angle angle is at 14° (26°). The distribution and average of the zenith angle for each bin is shown in Figure 5.15. Also shown is the offset distribution and average offset for each bin.

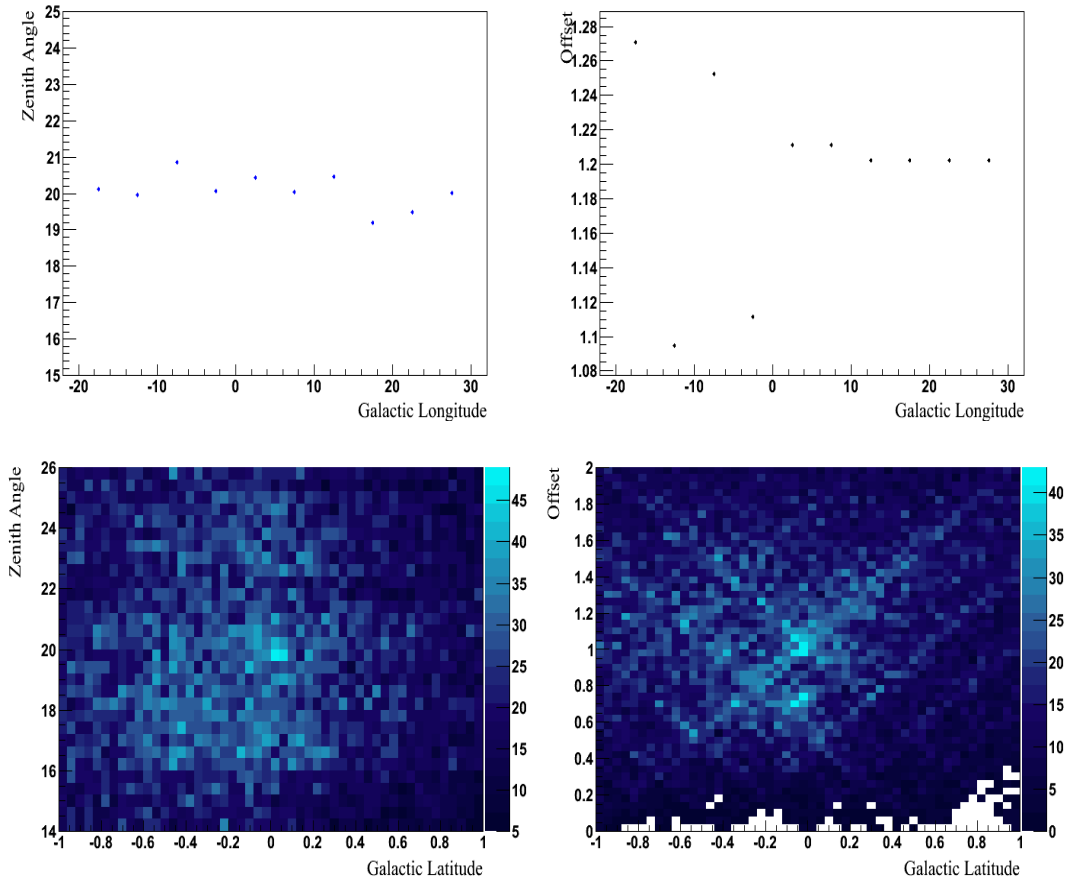

Figure 5.15: BOTTOM LEFT: The reconstructed zenith angle distribution used in the analysis as a function of Galactic longitude. TOP LEFT: The average reconstructed zenith angle of the Galactic dataset found within each longitude bin. BOTTOM RIGHT: The offset distribution as a function of Galactic longitude. TOP RIGHT: The average offset for each bin in longitude.

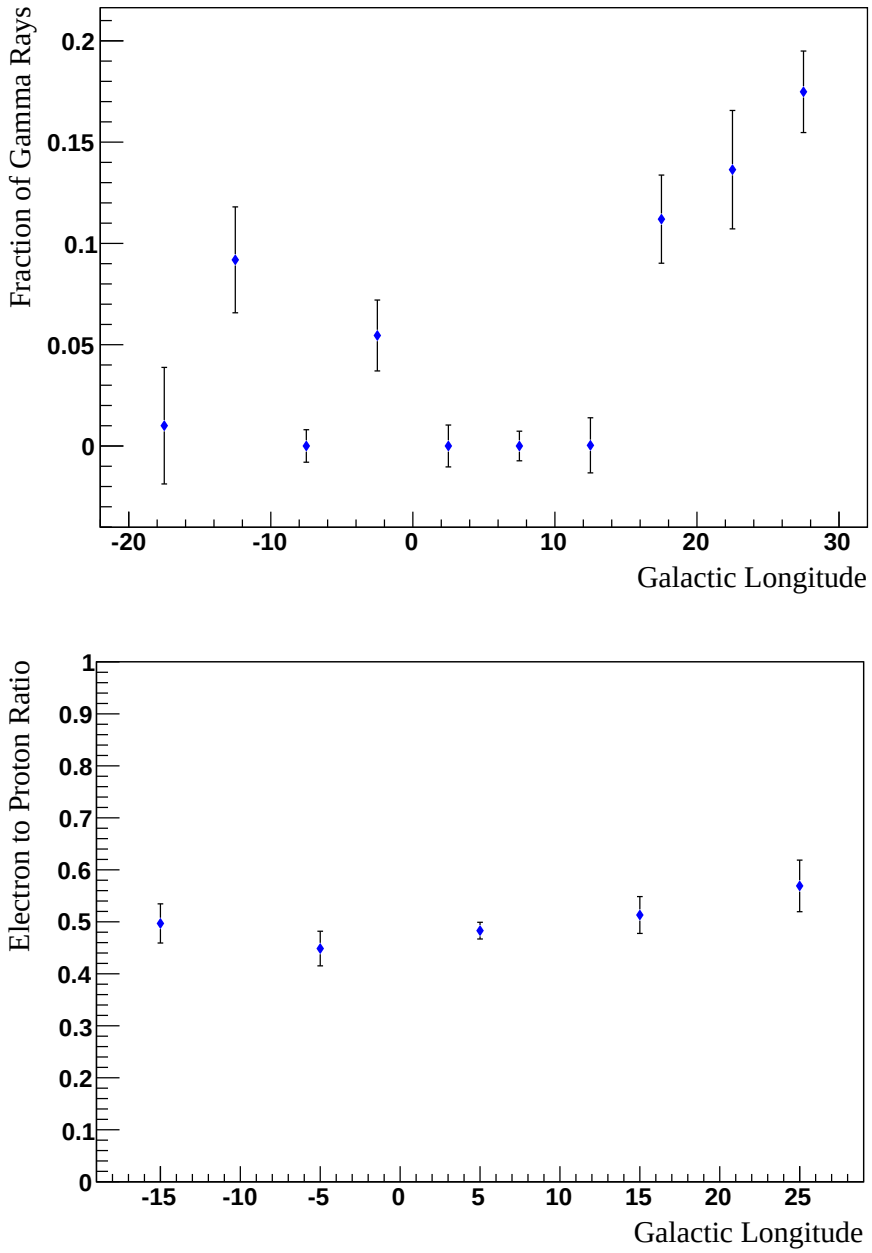

Figure 5.16: TOP: Fraction of γ rays in the Milky Way as a function of Galactic longitude. The latitude range was limited to -1 < b < 1°. BOTTOM: The electron to proton ratio shown as a function of Galactic longitude. The latitude range was limited to -1° < b < 1°.

It is important to note that, unlike the latitude analysis, the events are not chosen according to their offset value. Therefore, observation runs at the edge of the longitudinal bins may not replicate the offset values found in the data. To decrease any systematic effects, a large bin size of 5° was chosen to ensure that the majority of runs within the region being analysed represented the correct offset distribution.

Figure 5.16 shows the Galactic longitudinal profile of the estimated γ-ray fraction for a latitude range of -1 < b < 1°. The profile shows a varying γ-ray fraction, with strong emission regions of -10 > l > -15°, 0 < l < -5° and 15 < l < 30°. These correspond to known strong emission regions such as the Galactic centre, HESS J1825-137 and HESS J1713-397 (Carrigan et al. 2013).

The number of electron to proton events along the Galactic longitude was found to be centred around ≈ 0.5 for latitudes of -1 < b < 1°, as seen in Figure 5.16. This ratio is higher than that found in the analysis of the extragalactic *off* source region of 0.41±0.02. This could be due to only two components dominating the diffuse extragalactic regions - electrons and protons. Observations of the Milky Way are more complex to analyse as it involves three components of comparable flux levels. Misclassification between one or more components could contribute to the higher estimation of electron to proton events as discussed earlier in Section 5.1.7.

5.1.9 Conclusion

The Galactic diffuse γ-ray emission as a function of latitude was determined. This was achieved using a new analysis method that distinguishes between γ-ray, electron and proton events. The emission profile includes emission from known sources. No exclusion regions of sources were applied to minimize biases that may be caused by a differences in the offset distributions of simulations and data.

The emission profile was studied between latitudes of -2.7 < b < 2.1°. This range of latitudes was chosen due to criteria on the number of events required for each bin in latitude. The study was carried out in a longitude range of -30° < l < 40°, due to the cut criteria placed. An exclusion band was applied for all events between 16° < l < 19°, to prevents known source emission at high latitudes.

The profile of the fraction of γ rays after selection cuts was studied. The width (σ) of the emission profile is 0.25±0.05° for energies between 380 and 900 GeV. The width for events between 1 and 3 TeV is 0.20±0.06°. Both results are consistent with each other and there

is no indication of a wider emission profile in the higher energy band. This is consistent with widths found in the HGPS, which varied between $\approx$ 0.2 and 0.45° for the same region in longitude.

As there may be evidence for misidentification between γ rays and electrons, certain validity tests were carried out. The profile of the ratio of electromagnetic to proton events was found. The width of this profile for events between 380 to 900 GeV is 0.44±0.02°. For energies of 1 to 3 TeV, the width is 0.30±0.03°. This is slightly larger than the width of the γ-ray emission profile and indicates that the γ-ray profile might be underestimated due to potential misclassification.

The mean of the emission is not centred on zero but rather at a latitude of -0.08±0.06°. The peak of emission at a negative latitude is consistent with the result found in the previous H.E.S.S. study where the peak was also found at $b < 0°$ (Abramowski et al. 2014).

In addition, the emission profile in Galactic longitude was studied. Strong source regions corresponded to peak emission regions found in the profile. However, the γ-ray contribution was fit in large regions of longitude and a more detailed study should be carried out to make a comparison on smaller scales.

The analysis of the γ-ray emission in both Galactic latitude and longitude could be improved further with looser selection criteria. In order to achieve this, more simulations of diffuse γ rays and electrons at different zenith angles is needed. Furthermore, simulations generated in different telescope phases would allow a larger data sample to be analysed.

5.2 Isotropic γ-Ray Background

Measuring the Isotropic γ-Ray Background (IGRB) is challenging for ground based Cherenkov telescopes as the flux is very low in comparison to the background. As the electron component is far more dominant than the γ-ray one, a separation of the two is necessary. This is especially challenging as the expected γ-ray flux is small, making the weak IGRB signal hard to extract.

The fitting method discussed in Chapter 4 was used for this study. Upper limits were placed in two energy bands of 380 to 900 GeV and 1 to 6 TeV, with the results of the low energy band compared to measurements made with Fermi (Section 5.2.5).

5.2.1 Origins

The total γ-ray emission observed in the extragalactic sky can be described as the total sum of emission arising from resolved sources, any Galactic diffuse γ-ray emission (DGE) that might exist at high Galactic latitudes and the Isotropic γ-Ray Background (IGRB). Their total emission is referred to as the extragalactic γ-ray background (EGB).

The origins of the IGRB are unclear. It is thought to comprise of undetected sources of different phenomena including blazars, radio/γ galaxies, star forming regions, galaxy clusters and gamma ray bursts (Dermer 2007). More recently, the Fermi collaboration showed that the intensity of the IGRB compares well with the predicted intensity of unresolved sources such as Active Galactic Nuclei and star forming regions (Di Mauro 2016).

Additionally, VHE photons emitted from sources, such as AGNs, interact with the extragalactic background light (EBL) (Venters 2010) to produce electromagnetic cascades. The diffuse γ ray signal is attenuated at higher energies and increased at lower energies by this process.

5.2.2 Previous Measurements

Previous measurements of the IGRB have been made using the Fermi Large Area Telescope (Fermi LAT). The IGRB spectrum was determined between 200 MeV and 100 GeV (Abdo et al. 2010), with the measurement later extended to energies of 100 MeV to 820 GeV (Ackermann et al. 2015b).

The total EGB comprises of the IGRB, the DGE foreground and resolved sources. In order to correctly identify the IGRB, Fermi LAT studied the total EGB and DGE components.

Resolved Fermi LAT sources were subtracted from the spectrum, while the DGE component was less straight forward to analyse and contributed the most to the uncertainty of the IGRB measurement. Three models of the DGE were used to test the effect of its modelling on the spectrum.

The energy spectrum follows a power law with an index of 2.32±0.02 and has a cutoff energy of 279±52 GeV. An upper limit of 2.3×10^{-12} cm^2 s^1 sr^1 was determined between energies of 580 and 820 GeV.

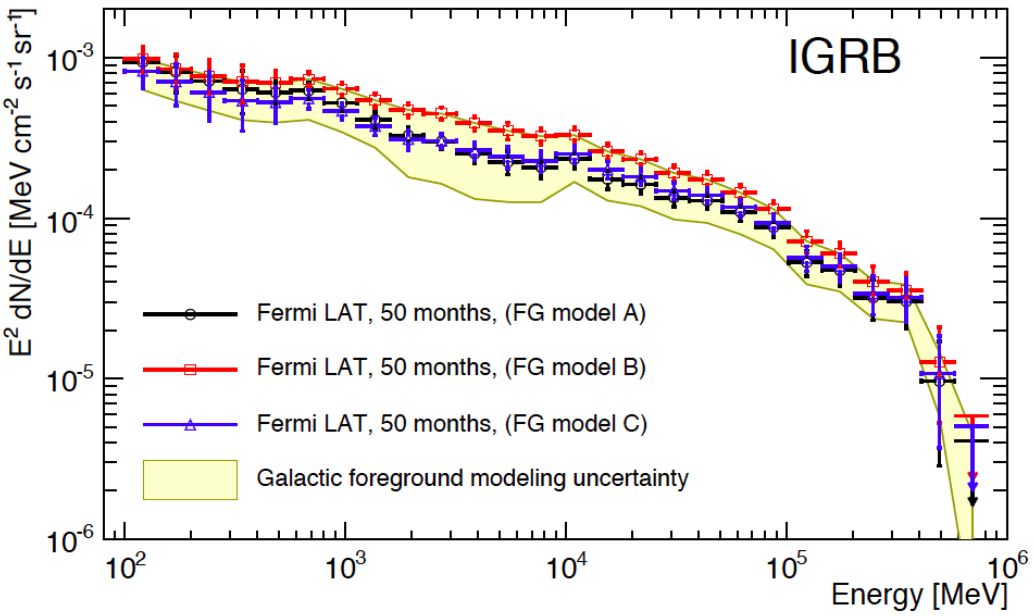

Figure 5.17: The Isotropic γ-Ray Background measured with Fermi LAT between 100 MeV and 820 GeV. Taken from (Ackermann et al. 2015b).

5.2.3 Motivation

Although a large amount of background is rejected in the HAP analysis, a proportion of protons and electrons are still misidentified as γ-ray events. The contribution of γ rays in the data sample becomes more prominent after a cut on the standard zeta variable of the TMVA HAP analysis is made, making the signal easier to extract. However, significant contributions from electrons and protons are still present and there is a necessity to first separate these

events. A second criteria is that the separation power has to be strong enough to correctly identify the weak IGRB signal.

The three component separation method outline in Chapter 3.3 satisfies the first criteria by identifying between electron, proton and γ-ray events on a statistical basis. However, there is still a large statistical error when fitting each contribution. Furthermore, the systematic uncertainty is not taken into account in this study but is estimated to be more dominant than the statistical error.

The aim of this study is not to put constraints on source models of the IGRB, as the upper limits do not compare with the upper limit placed by Fermi between 580 and 820 GeV. Rather, the limits placed here are useful in understanding the maximum γ-ray contribution for energies of $E >$ 820 GeV. One application of this is a background estimation in studies of the cosmic ray electron spectrum (CRE).

As previous studies on CREs have distinguished between electron and proton events, an estimate of the maximum amount of contamination was made in a previous study with H.E.S.S. (Egberts & H.E.S.S. Collaboration 2011). It was concluded that the γ-ray contamination could be as high as 50%.

It should be mentioned that the γ-ray emission measured here is the emission of the IGRB plus any DGE component that might exist at high Galactic latitudes. The DGE component arises from CR interactions with the H_I and H_2 gas of the galaxy that may also extend to high latitudes.

5.2.4 Data Selection

An off source region at a high Galactic latitude was selected to ensure that any contributions from the DGE are minimized. The background regions taken during observations of PKS 2155-304 were used, as the observation position was at a Galactic latitude of -52.25°.

Only runs that were taken in the phase1b state (optical efficiency of ≈70%) were included. Observation runs that included participation from all four H.E.S.S. I telescopes were chosen, while CT5 was not included in this study. Runs were selected if they had a mean zenith angle between 17 and 23°. A total of 40 runs with a livetime of 17.5 hrs were used in the analysis.

5.2.5 Results

The contribution of γ-rays, electrons and protons were determined for observation regions of the source PKS 2155-304.

Events were taken in regions *off* the source and *on* the source. The *excess* distribution was determined from subtracting the *off* events from the distribution of *on* events. It represents events coming from the source and is expected to follow the simulated γ-ray events closely.

A validity check was performed on the electron to proton ratio *e/p* in the *off* regions of two sources: PKS 2155-304 and Centaurus A. The *e/p* ratio is expected to be constant within one energy band if the local CRs are assumed to be isotropic. Therefore, comparing the e/p ratio for different positions gives an indication of the stability of the method. Table 5.5 shows the values of e/p for the *off* source regions at the two different target positions.

Source	Region	Analysis	e/p Ratio
PKS2155-304	*off*	1D	0.45 ± 0.05
		2D	0.41 ± 0.02
Centaurus A	*off*	1D	0.56 ± 0.24
		2D	0.39 ± 0.07

Table 5.5: Fit results of the electron to proton (e/p) ratio for the *off* region in the 1D and 2D analysis (Chapter 4) of PKS 2155-304 and Centaurus A.

The e/p values for both dimensions and target positions are compatible within errors. The estimated fraction of each component in each observation region for the 1D and 2D analyses of PKS 2155-304 are shown in Table 5.6 and are discussed in more detail in Section 4.2.

The fraction of γ rays found in the *off* region for the 1D analysis is 3±4% and for the 2D analysis is 7±1% for energies of 380 to 900 GeV. This translates to a flux of 5×10^{-3} MeV cm^{-2} s^{-1} sr^{-1}. For higher energies of 1 to 6 TeV, an upper limit flux of 4×10^{-3} MeV cm^{-2} s^{-1} sr^{-1} was found (Table 5.7).

This is high compared to the Fermi upper limit of $\approx 6 \times 10^{-6}$ MeV cm^{-2} s^{-1} sr^{-1} and larger than the flux at the cutoff energy, E^2 dN/dE $\approx 4 \times 10^{-5}$ MeV cm^{-2} s^{-1} sr^{-1}. However, due

to the much higher background than signal, reaching a statistical and systematic accuracy to achieve a lower limit is not possible here. Also, as the estimate obtained from the 1D analysis is consistent with 0%, the flux values quoted here are upper limits.

Dimension	Region	γ rays	Electrons	Protons
1D	*excess*	100 ± 1%	1 ± 1%	-1 ± 1%
	on	99 ± 5%	-2 ± 4%	3 ± 2%
	off	3 ± 4%	30 ± 3%	67 ± 1%
2D	*excess*	100 ± 0%	1 ± 1%	-1 ± 1%
	on	99 ± 2%	-3 ± 2%	4 ± 1%
	off	7 ± 1%	27 ± 1%	66 ± 1%

Table 5.6: Fit results of the 1D and 2D analyses for the γ-ray, electron and proton percentages for *excess*, *on* and *off* events of PKS 2155-304.

Energy	Flux (MeV cm^{-2} s^{-1} sr^{-1})
0.38 - 0.9	5×10^{-3}
1 - 6	4×10^{-3}

Table 5.7: Upper limits on the flux of the IGRB values for two energy bands: 380 to 900 GeV and 1 to 6 TeV.

5.2.6 Conclusions

Upper limits on the IGRB in two energy ranges of 380 to 900 GeV and 1 to 6 TeV were determined. An upper limit has not been previously possible at TeV energies with an IACT array due to the low flux level of the IGRB and, therefore, the overwhelming background of electrons and protons. Using a new analysis method outlined in Chapter 4, studies on diffuse emission such as the IGRB are now possible as both backgrounds of electrons and protons are estimated in the same region as the diffuse γ-ray emission. However, though a further suppression of the hadronic background has been achieved and the remaining electron component identifiable, the weak signal of the IGRB is still challenging to measure with the accuracy achieved.

The upper limit place at energies of 380 to 900 GeV is 5×10^{-3} MeV cm^{-2} s^{-1} sr^{-1}. This is three orders of magnitude higher than the upper limit placed with Fermi between 580 and 820 GeV of $\approx 6{\times}10^{-6}$ MeV cm^{-2} s^{-1} sr^{-1} (Ackermann et al. 2015b). The limit placed at energies of 1 to 6 TeV is 4×10^{-3} MeV cm^{-2} s^{-1} sr^{-1}.

Although these upper limits may not be constraining for models of the IGRB, it is a determination of an upper limit in the TeV regime, demonstrating that the tools needed to provide such an upper limit are being improved. Furthermore, this measurement allows a determination of the maximum γ-ray contribution from the IGRB at TeV energies, which is useful for other studies in the same energy domain. An example of this is studies on the CRE flux, where the amount of background contamination from diffuse γ rays is still unknown. Moreover, the measurement has the potential to be improved with more sensitive telescopes such as H.E.S.S. II or a next generation Cherenkov telescope such as CTA.

5.3 Electron Spectrum

A measurement of the electron plus positron spectrum between energies of 0.38 and 14 TeV is presented. The spectrum was determined using an independent analysis than previously used with ground based Cherenkov telescopes. The separation technique discussed in Chapter 4 was utilized in this study to estimate the cosmic ray electron contribution. In this section, the term electrons refers to both electrons and positrons. If a distinction in their charge is made, the terms negative electrons (e^-) and positrons (e^+) are used.

The origin of cosmic ray electrons in the TeV regime is discussed in Section 5.3.1. Previous measurements of the spectrum are described in Section 5.3.2 and the motivation for this study is outlined in Section 5.3.3. The fit results are described in Section 5.3.7.

5.3.1 Origins

This study measures the sum of two distinct populations of cosmic ray electrons (CREs), namely negative electrons and positrons. Therefore, sources of both populations are introduced. Firstly, the origin of negative electrons is discussed and the astrophysical processes related to positrons are discussed in Section 5.3.1.

CREs can be categorized as having either a direct or indirect origin. Electrons can be accelerated to TeV energies in supernova remnants (SNR) and micro-quasars. Both positrons and negative electrons could be produced in interactions of CRs with the ISM, from dark matter (DM) processes or accelerated in pulsars.

SNR are left after highly energetic astrophysical events known as supernovae, in which a star undergoes its last stage of stellar evolution. The SN could be the core collapse of a massive star or a type Ia explosion of a white dwarf. A SNR can accelerate particles to high energies through Diffusive Shock Acceleration (Reynolds 1997) (Reynolds 2008). X-Ray observations confirm populations of electrons in SNR while proton signatures have also been detected (Ackermann et al. 2013).

A supernova (SN) can result in the formation of a fast rotating neutron star with extreme magnetic field strengths of 10^{10} - 10^{13} G, known as a $pulsar$. Pulsars can have fast rotation periods on the order of milliseconds. The fast rotation of the magnetic field generates very strong electric fields where particles are accelerated. Pulsars are known to accelerate electrons to high energies. There are three models describing different acceleration zones: the Polar Cap (Zhang & Harding 2000), Slot Gap (Muslimov & Harding 2003) and Outer Gap

(Chiang & Romani 1994) model.

Annihilation of dark matter could also result in the formation of leptonic pairs. This process would manifest itself as a decrease in the CRE flux level above the DM particle mass. Although this is expected to have a contribution to the overall CRE flux, the predicted flux is orders of magnitude smaller than the observed level. However, two processes are thought to increase the DM contribution - sub-halos within the galaxy (Berezinsky et al. 2014) and an elevated decay rate (Panov 2013).

Electrons are thought to be accelerated to high energies in the jets of Micro-quasars. Micro-quasars are binary systems in which stars transfer material to a compact object, thought to be a black hole with a mass comparable to stellar masses. Particles are accelerated in relativistic jets, though the overall amount of electrons accelerated to TeV energies is not known. Further details of micro-quasars can be found in (Rosswog & Brüggen 2011).

Positrons

The ratio of positrons to the total sum of positrons plus electrons (known as the positron fraction), $N_{e^+}/(N_{e^+} + N_{e^-})$ is approximately 10% at ≈100 GeV. CR positrons arise from interactions of hadronic CRs with the ISM.

The injection spectra of CR positrons is expected to be steeper than that of CR negative electrons (Serpico 2009). This would result in a decrease in the positron fraction with energy. However, studies by PAMELA (Adriani et al. 2009), Fermi LAT (Ackermann et al. 2012a) and more recently by AMS-02 (Aguilar et al. 2014) have measured an increase in the positron fraction at energies of ≈ 10 to 250 GeV. As this excess cannot be explained by current CR propagation models, the excess is attributed to possible sources of electron positron pairs, namely pulsars and dark matter (DM) processes. An overview of possible origins of the positron excess is given in (Serpico 2012).

Local pulsars such as Geminga and Monogem could provide a high enough flux of accelerated positrons and negative electrons, generated in their strong magnetic fields, to explain the excess (Linden & Profumo 2013). Another possible origin is from DM annihilation producing electron positron pairs. This would result in an excess in the positron flux and could explain the observed increase in the positron fraction.

5.3.2 Previous Measurements

A measurement of the CRE spectrum from 1 to 14 TeV was made by the H.E.S.S. collaboration (Aharonian et al. 2008) in 2008. Full details of the analysis can be found in Kathrin Egberts' thesis (Egberts 2009). A power law with an exponential cutoff was fit to the data and an index of 3.05±0.02 and cutoff energy of 2.1±0.3 was found when combined with measurements at lower energies. The analysis used in the 2008 study has been applied to a much larger dataset by David Kolitzus (Kolitzus 2015). A measurement by VERITAS (Staszak & for the VERITAS Collaboration 2015) using the same analysis was made and the MAGIC collaboration have also carried out a study (Borla Tridon 2011). Measurements of the CRE spectrum are shown in Figure 5.18.

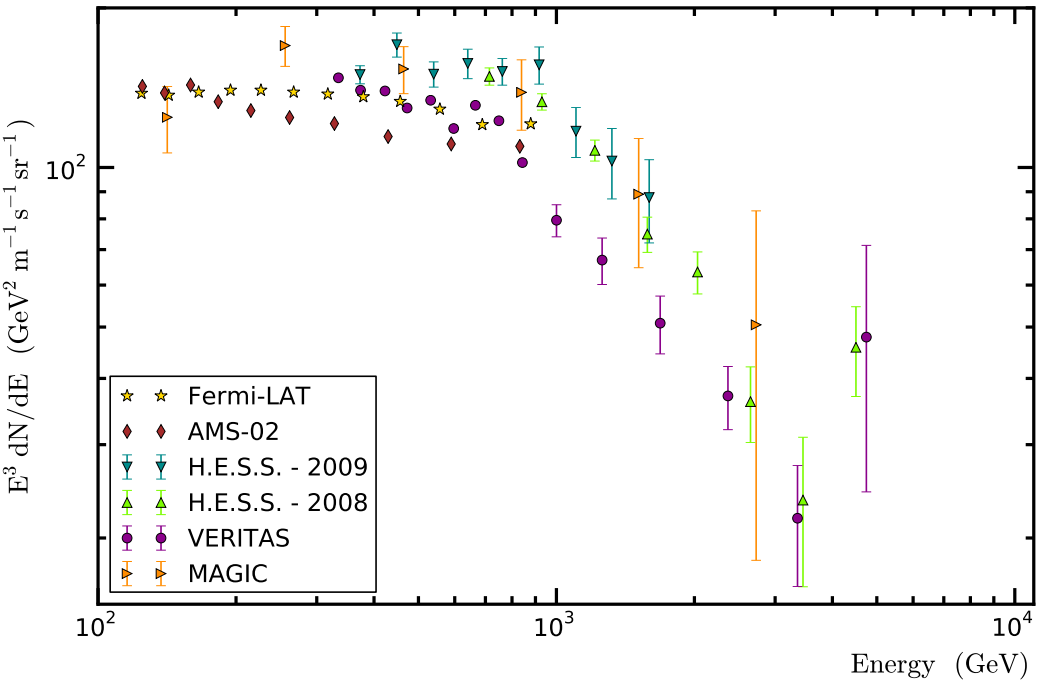

Figure 5.18: The electron spectrum as measured with previous measurements. Data from H.E.S.S. (Aharonian et al. 2009) (Aharonian et al. 2008), Fermi LAT (Ackermann et al. 2010a), AMS-02 (Aguilar et al. 2014), VERITAS (Staszak & for the VERITAS Collaboration 2015) and MAGIC (Borla Tridon 2011) are shown. Error bars for Fermi and AMS-02 are not included.

The H.E.S.S. measurement was extended to energies of 300 to 800 GeV (Aharonian et al. 2009) in order to probe an excess measured in the CRE flux with ATIC (Chang et al. 2008). A peak in the CRE spectrum below 1 TeV could be interpreted as a dark matter signal. However, subsequent measurements with H.E.S.S. and other instruments have not yielded a similar peak in the spectrum. A broken power law was fit to the data, with the spectrum steepening from an index of 3.0±0.1 to 4.1±0.3 at a break in energy of 0.9±0.1 TeV.

The Fermi collaboration (Ackermann et al. 2010a) has measured the CRE spectrum from 7 GeV to 1 TeV. A power law with a spectral index of 3.08±0.05 describes their data well. AMS has also carried out a study on the combined CRE spectrum up to energies of 700 GeV (Aguilar et al. 2014). A rise in the positron fraction was measured by both instruments (see Section 5.3.1).

There is a hint of a rise in the CRE spectrum above energies of ≈ 3.5 TeV with H.E.S.S. and VERITAS (Figure 5.18). A rise in the spectrum could have several origins such as accelerated electrons from a nearby source (Delahaye et al. 2010) (Hinton et al. 2011) or it could be attributed to high level of background contamination from undetected γ-ray sources. Another possible scenario is that a small fraction of hadrons are misidentified as electromagnetic events.

5.3.3 Motivation

An interesting energy region of the CRE spectrum is at energies above a few hundred GeV. A break in the energy spectrum is seen at ≈ 1 TeV and a potential rise in the spectrum above an energy of ≈ 3.5 TeV could be an indication of a nearby accelerator.

Ground based Cherenkov telescopes such as H.E.S.S. can probe this region. The disadvantage is that Cherenkov telescopes capable of making a measurement of the CRE spectrum above a few hundred GeV do not distinguish electrons from γ rays. For this reason, measurements of the electron spectrum made with H.E.S.S. and VERITAS have used the same analysis. The method used in these measurements utilizes a random forest algorithm to identify electrons from hadrons.

The motivation of this study is to measure the CRE spectrum with an independent method. The analysis method outlined in Chapter 4 was used to estimate the flux of cosmic ray electrons between 0.38 and 14 TeV. The method not only provides further identification of the hadronic background but also distinguishes between electron and γ-ray events.

5.3.4 Data Selection

Observation runs having an optical efficiency of 70% (phase1b) were first selected. Simulations for diffuse γ rays, electrons and protons in the same telescope phase were available at a zenith angle of 20°. Therefore, runs with a mean zenith angle between 17 and 23° were chosen. 315 runs having a combined livetime of 134.2 hours were analysed.

The contribution from the total EGB is expected to be very low, only $\approx$ 0.2% when compared to the electron spectrum (Kolitzus 2015). Furthermore, observations taken at a Galactic latitude of $|b| > 7°$ were chosen. This was to minimize the contribution of diffuse γ-ray emission from interactions of cosmic rays with H_I and H_2 gas in the Milky Way. The exact extension of the Galactic γ-ray emission is not known.

Though a separation of contributions from γ rays, electrons and protons could be carried out in the analysis, the average spectral index of sources contained within the data varies. The γ rays are weighted according to a spectral index of Γ = -2.32. To ensure that this represented the γ ray events in the dataset closely, events with an offset of more than 0.4° from a known source position were excluded. The event selection criteria is summarized in Table 5.8.

5.3.5 Event Selection

Firstly, events that pass the TMVA HAP *standard_zeta* selection cut (Ohm et al. 2009) were considered. This was to ensure as many hadrons were rejected as possible before analysing events further. This allowed a comparable fraction of electrons and protons in the remaining data - improving the fit accuracy.

Parameter	Criteria
Impact distance	280 m
Telescope Multiplicity	4

Table 5.8: Event selection criteria used in the determination of the CRE spectrum.

Only events that involved participation from all four H.E.S.S. I telescopes were included. This was to ensure a more accurate direction and energy reconstruction to achieve the best

background separation. Similarly, events with an impact parameter of less than 280 m were chosen. The event selection criteria are summarized in Table 5.8.

5.3.6 Effective Area

To calculate the flux of the cosmic ray electrons, the effective collection area, A_{eff}, is first determined. Selection criteria reduces the number of events used in the analysis. A_{eff} provides a description of this change and is determined using simulations of air showers. The air shower events are simulated over a certain area (A^{MC}) with A_{eff} defined as:

$$A_{eff} = \frac{N_e^{sel}(E)}{N_e^{MC}(E)} \cdot A^{MC} \tag{5.1}$$

Choosing events according to selection criteria reduces the detection efficiency and therefore, the effective area. This reduction in efficiency is found by taking the number of simulated electron events passing the selection criteria (N_e^{sel}), within a given energy bin, and dividing it by the total number of electrons simulated in the same energy range. The effective area is then found by multiplying the cut efficiency by the simulated area, A^{MC}.

A_{eff} is calculated as a function of simulated energy, E_{sim}, while the cosmic electron spectrum is calculated in reconstructed energy, E_{reco}. The relationship between E_{sim} and E_{reco} needs to be understood in order to find the correct effective area. This was done by finding the ratio of the sum of weights of N_e^{sel} as a function of true energy and reconstructed energy:

$$N_{e\_sim}^{sel} = N_{e\_reco}^{sel} \frac{\sum E_{sim}^{\Gamma+\Gamma_{MC}}}{\sum E_{reco}^{\Gamma+\Gamma_{MC}}} \tag{5.2}$$

$N_{e\_sim}^{sel}$ is the number of simulated events that pass selection criteria and have a *simulated* energy within the given energy range. $N_{e\_reco}^{sel}$ is the number of simulated events that pass selection cuts and have a *reconstructed* energy within the given energy range. Γ_{MC} is the power law index that the air shower simulations are generated with. Γ is the expected power law index of each component and is used to weight the simulations in the analysis. The effective area used to determine the electron flux is shown in Figure 5.19.

A weighting is applied to the simulations as the Monte Carlo events are generated with an index of -2, while the electron spectrum is expected to be steeper. To correct for this, the same weighting used to train classifier values during the analysis of PKS 2155-304

(Chapter 4) was applied. Each energy bin was weighted by a factor of $E^{\Gamma+2}$, with Γ being the spectral indices determined by Fermi LAT (Ackermann et al. 2010a) and H.E.S.S. (Egberts & H.E.S.S. Collaboration 2011). The values correspond to Γ = -3.08 for energies $E \leq 1$ TeV and Γ = -4.1 for $E > 1$ TeV.

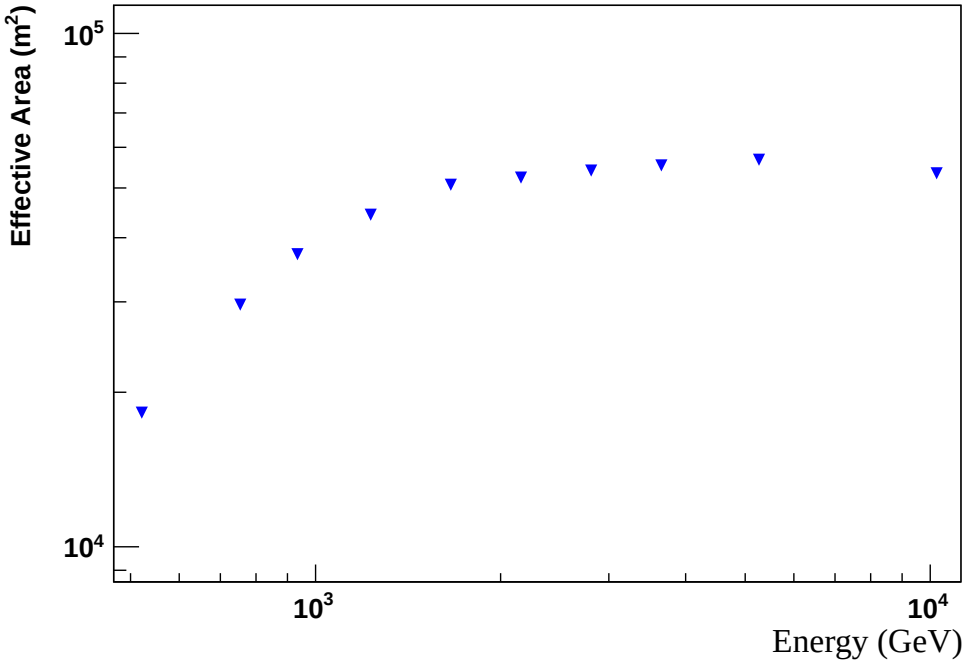

Figure 5.19: The effective area of each energy bin, used in the calculation of the cosmic electron spectrum.

5.3.7 Spectrum

The differential energy spectrum is found by finding the number of electrons per unit area, energy, solid angle and time for each energy bin. The flux is determined as:

$$\frac{dN}{dE} = \frac{N(E)}{A_{eff}(E) \cdot \Delta E \cdot \Omega \cdot T} \tag{5.3}$$

where $N(E)$ is the number of electrons within each energy bin, A_{eff} is the effective collection area, ΔE is the size of the energy bin, Ω is the solid angle and T is the livetime.

$N(E)$ is calculated for each energy bin by multiplying the estimated fraction of electrons by the number of observation events passing the cut criteria. The fraction of electrons was determined using the three component separation analysis discussed in Chapter 4.

The PMBg background method (Marandon 2010) was used to determine *on* and *off* source regions. This method ensured that the offset distributions of the data resembled the simulations. The number of data events was corrected to account for the fraction of area observed in the *off* regions.

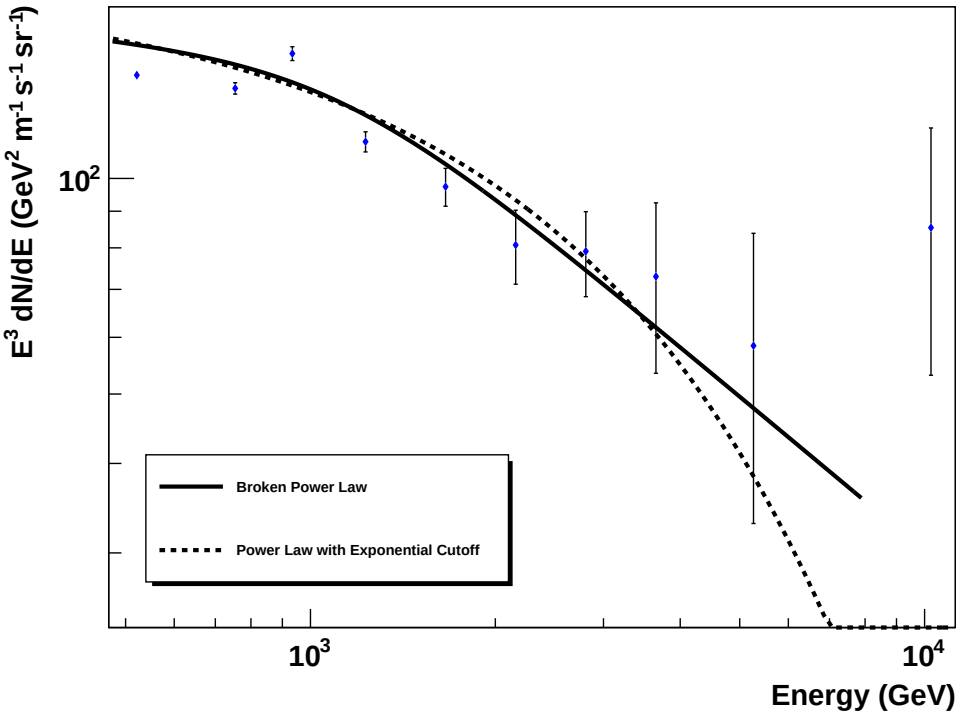

Figure 5.20: The differential energy spectrum of cosmic ray electrons between energies of 380 GeV to 14 TeV. A broken power law was fit to the data and is shown as a solid black line. A power law with an exponential cutoff was fit in addition and is shown as a dashed black line.

The simulated events used in the fitting procedure are weighted by $E^{\Gamma+2}$, where Γ is the expected spectral index of the component. The spectral index used for the γ-ray events was Γ = -2.3. This is the spectral index of the IGRB, determined by Fermi LAT up to a cutoff

energy of 279±52 GeV (Ackermann et al. 2015b). The spectral index past this energy has not been determined, but is expected to be steeper. The proton index was taken as the locally measured cosmic ray spectrum (Γ = -2.7). For the electron events, the power law index was taken as Γ -3.08 for energies E < 1 TeV and Γ = -4.1 for E > 1 TeV. The same weighting was applied during the training procedure to obtain the classifier distributions for γ ray, electron and proton events (Chapter 4).

Figure 5.20 shows the CRE spectrum determined. The differential flux (dN/dE) is multiplied by the middle of the (logged) energy bin cubed, E_i^3. The errors of the cosmic electron flux represent the 1σ errors. The spectrum was fit with two functions. First, a broken power law was fit in the form:

$$\frac{dN}{dE} = k \cdot (\frac{E}{E_b})^{-\Gamma_1} \cdot (1 + (\frac{E}{E_b})^{1/\alpha})^{-(\Gamma_2-\Gamma_1)\alpha} \tag{5.4}$$

where a fixed value of α = 0.3 was chosen. The normalisation factor is $k = 1.08 \pm 0.12 \times 10^{-7}$ and the break energy is E_b = 1.11±0.04 TeV. The spectral index changes from Γ_1 = 3.08±0.06 to Γ_2 = 3.72±0.12. The χ^2 value is 31.6. The last spectral point was not included in the fit. The fit is shown in Figure 5.20. Secondly, a power law with an exponential cutoff was fit to the spectrum in the form:

$$\frac{dN}{dE} = k \cdot E^{-\Gamma} \cdot exp(\frac{E}{E_c}) \tag{5.5}$$

where Γ is the spectral index and E_c is the cutoff energy. An index of Γ = 3.04±0.09 and a cutoff energy of E_c = 3.64±1.35 TeV was found. The χ^2 value of the fit is 34.9 and is shown in Figure 5.20.

5.3.8 Conclusion

The data was fit with a broken power law. The break in energy is at E_b = 1.11±0.04 with the spectrum steepening from Γ_1 = 3.08±0.06 to Γ_2 = 3.72±0.12 at energies E > E_b. The spectrum at E < E_b is in agreement with the previous H.E.S.S. measurement (Aharonian et al. 2009) and Fermi LAT (Ackermann et al. 2010a). However, the index measured above E_b is smaller than the index found previously (Γ_2 = 4.1±0.3). Nevertheless, both indices are compatible within statistical uncertainties.

Additionally, a power law with an exponential cutoff was fit to the spectrum with an index of Γ = 3.00±0.09 and a break in energy of 3.16±0.95 TeV. However, the data is described better by a broken power law. No excess in the CRE flux was found at energies lower than 1 TeV, contrary to the result found with ATIC.

There is a hint of a rise in the spectrum at high energies in the CRE flux determined here. The estimated flux rises above an energy of ≈ 5.2 TeV. This is higher than what has previously been indicated (Aharonian et al. 2008). More investigation into the possible origins of a rise, whether physical or systematic, needs to be carried out.

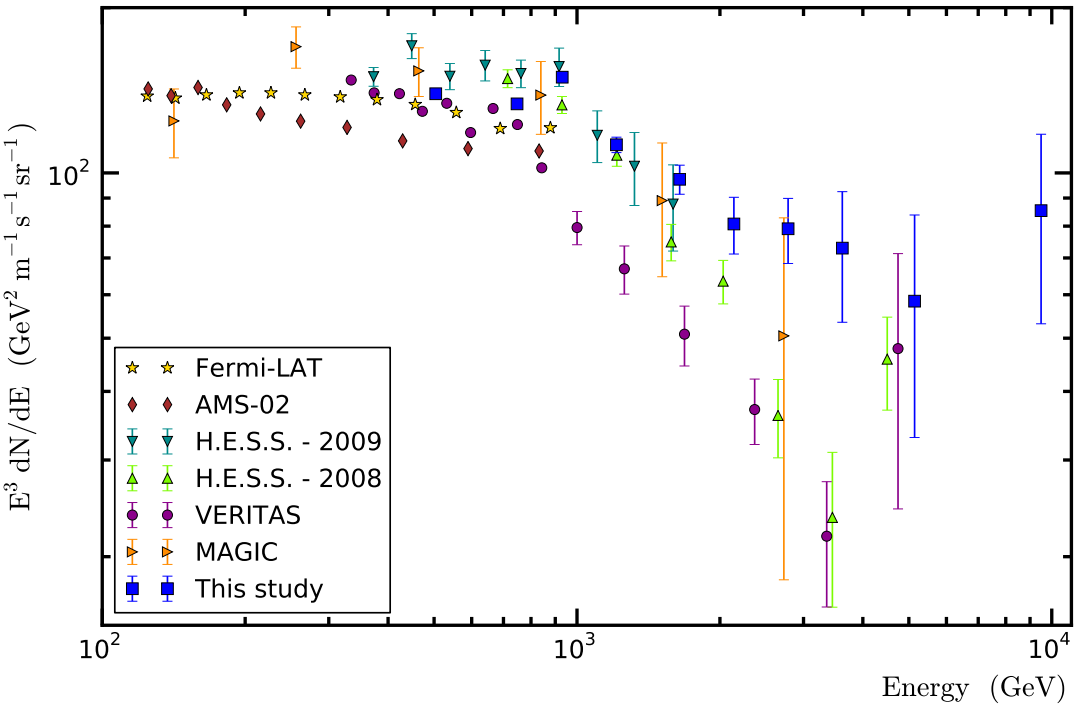

Figure 5.21: The electron spectrum found in this study compared with previous measurements. Data from H.E.S.S. (Aharonian et al. 2009) (Aharonian et al. 2008), Fermi LAT (Ackermann et al. 2010a), AMS-02 (Aguilar et al. 2014), VERITAS (Staszak & for the VERITAS Collaboration 2015) and MAGIC (Borla Tridon 2011) are included. Error bars for Fermi and AMS-02 are not shown.

Towards higher energies there is a lack in statistics as the number of runs was limited by strict selection criteria on the mean zenith angle. This was to minimize the effect of the zenith angle dependence of the analysis method. The dataset could be expanded with more simulations for all diffuse components at different zenith angles.

The same calibration chain and Monte Carlo simulations were used in this study as previous H.E.S.S. studies described in Section 5.3.2. However, the method described in Chapter 4 and used in this estimation of the CRE energy spectrum is independent from previous CRE analyses. A comparison of the measured spectrum in this study with previous measurements is shown in Figure 5.21.

Conclusion and Outlook

The scope of this thesis includes the development of an image analysis technique that separates γ-ray, electron and proton events. The technique is applied to data events passing an initial background rejection cut with TMVA HAP.

The rejection of 65% (37%) of γ-like proton (electron) events that pass existing *standard_zeta* selection criteria is achieved while keeping 85% (80%) of the γ-ray signal.

The BL Lac source, PKS 2155-304, was used to test the accuracy of the method. The estimated contribution of γ rays was 100±1% for the *excess* event distribution, which is the expected value.

Tests were carried out to assess the dependencies of the method on zenith angle and offset. The method was found to be strongly dependent on both, while the percentage of misclassification was found to be approximately constant with an increasing contribution of γ rays. The systematic uncertainty arising from the analysis method was assessed with simulations to be 6%, 1% and 2% for γ rays, electrons and protons respectively. These uncertainties are valid with identical zenith angle and offset distributions of the data and simulations.

The latitude profile of the galactic diffuse γ-ray emission was studied in a longitude range of -30° < l < 40°. A width of σ = 0.25±0.05° was measured for events with a reconstructed energy of 380 to 900 GeV. For events between 1 and 3 TeV, the width of the profile is 0.20±0.06°. Both results are compatible and no evidence of a wider emission profile in the higher energy band was found. This result is consistent with a previous study on the diffuse γ ray emission in the galaxy with the H.E.S.S. Galactic Plane Survey (HGPS).

A measurement of the cosmic ray electron spectrum was made in the energy range 380 GeV to 14 TeV. A broken power law was fit to the data with a spectral index of Γ_1 3.08±0.06 for energies below a break in energy (E_b) of 1.11±0.04 and an index of Γ_2 = 3.72±0.12 above E_b. Within statistical uncertainties, the spectral index is consistent with previous H.E.S.S. measurements. However, the spectral index above E_b measured in the 2008 H.E.S.S. analysis is steeper at Γ_2 = 4.1±0.3. Furthermore, a hint of a rise was previously found above ≈ E = 3.5 TeV, whereas the measured spectrum of this study increases above an energy of ≈ E = 5.2 TeV.

An upper limit on the Isotropic γ-Ray Background (IGRB) was made for two energy bands. An upper limit of 5×10^{-3} MeV cm^{-2} s^{-1} sr^{-1} was determined for energies of 380 to 900 GeV and 4×10^{-3} MeV cm^{-2} s^{-1} sr^{-1} for an energy range of 1 to 6 TeV. The flux of the lower energy band was compared to a previous measurement made with Fermi LAT, which is more constraining. The measurement is not constraining for models on the IGRB but does provide an estimate of the maximum contribution of isotropic γ rays in the extragalactic sky.

The analysis method could also be utilized in CR composition studies. As the method makes use of direct Cherenkov light, one would expect there to be potential for separation of similarly charged nuclei.

The scope of this thesis covers the realm of H.E.S.S. I. The analysis technique could be improved by applying it to H.E.S.S. II and incorporating the fifth telescope (CT5). The increased sensitivity of CT5 will improve the detection of the weak direct Cherenkov signal that the analysis technique is dependent on.

The method could also prove useful for the next generation of Cherenkov telescopes. The Cherenkov Telescope Array (CTA) is a planned array of IACTs expected to be completed by 2024. The southern array will cover an area of ≈ 4 km^2 and is made up of telescopes of varying sizes. The increased area of CTA will improve the background suppression of hadronic showers, making the electron background increasingly more important. As no distinction of the electron background is made, the discussed analysis technique could be utilized in the CTA framework.

Acknowledgements

I would like to thank Prof. Werner Hofmann for suggesting the topic of my thesis and for the discussions and scientific guidance of my PhD. Thank you for giving me this amazing opportunity. I would like to thank Prof. Jim Hinton for the suggestions on improvements in my analysis and scientific approach. Thank you to Prof. Stefan Wagner for being on my thesis committee and for ensuring progress on my thesis.

Thank you to Christian Fendt for the support, especially in starting my PhD in a new country. Thank you to the H.E.S.S. collaboration for providing the foundation of this thesis and for the welcoming environment at collaboration meetings.

I would like to thank Dan for the many suggestions and guidance. I would like to thank Vincent for always being available for discussions, whether scientific or technical, and for proof reading. Thank you to Aion for taking an interest in my work and giving useful suggestions. I would like to thank the H.E.S.S. group at MPIK for the many memories. Thank you to my officemate Peter for the countless discussions on possible *Game of Thrones* endings and for the practice in Namibian English. Thanks to my officemate Faical for all the laughs. We finally have fuel for our office heating.

I would like to thank Simon for always supporting and encouraging me no matter what. Thank you to my family in South Africa for your unwavering support. I would like to thank my twin, Eddie, for always believing in me. To my parents, words cannot describe how grateful I am for all the sacrifices you have made. Your unconditional support and love gives me strength every day. Thank you!

Bibliography

Abdo, A. A., Ackermann, M., Ajello, M., et al. 2010, Spectrum of the Isotropic Diffuse Gamma-Ray Emission Derived from First-Year Fermi Large Area Telescope Data, Physical Review Letters, 104, 101101

Abramowski, A., Aharonian, F., Ait Benkhali, F., et al. 2014, Diffuse Galactic gamma-ray emission with H.E.S.S., Phys. Rev. D, 90, 122007

Ackermann, M., Ajello, M., Albert, A., et al. 2015a, The Spectrum of Isotropic Diffuse Gamma-Ray Emission between 100 MeV and 820 GeV, ApJ, 799, 86

Ackermann, M., Ajello, M., Albert, A., et al. 2015b, The Spectrum of Isotropic Diffuse Gamma-Ray Emission between 100 MeV and 820 GeV, ApJ, 799, 86

Ackermann, M., Ajello, M., Allafort, A., et al. 2012a, Measurement of Separate Cosmic-Ray Electron and Positron Spectra with the Fermi Large Area Telescope, Physical Review Letters, 108, 011103

Ackermann, M., Ajello, M., Allafort, A., et al. 2013, Detection of the Characteristic Pion-Decay Signature in Supernova Remnants, Science, 339, 807

Ackermann, M., Ajello, M., Atwood, W. B., et al. 2010a, Fermi LAT observations of cosmic-ray electrons from 7 GeV to 1 TeV, Phys. Rev. D, 82, 092004

Ackermann, M., Ajello, M., Atwood, W. B., et al. 2012b, Fermi-LAT Observations of the Diffuse γ-Ray Emission: Implications for Cosmic Rays and the Interstellar Medium, ApJ, 750, 3

Ackermann, M., Ajello, M., Atwood, W. B., et al. 2010b, Searches for cosmic-ray electron anisotropies with the Fermi Large Area Telescope, Phys. Rev. D, 82, 092003

Adriani, O., Barbarino, G. C., Bazilevskaya, G. A., et al. 2009, An anomalous positron abund-

ance in cosmic rays with energies 1.5-100GeV, Nature, 458, 607

Aguilar, M., Aisa, D., Alvino, A., et al. 2014, Electron and Positron Fluxes in Primary Cosmic Rays Measured with the Alpha Magnetic Spectrometer on the International Space Station, Physical Review Letters, 113, 121102

Aharonian, F., Akhperjanian, A. G., Anton, G., et al. 2009, Probing the ATIC peak in the cosmic-ray electron spectrum with H.E.S.S., A&A, 508, 561

Aharonian, F., Akhperjanian, A. G., Aye, K.-M., et al. 2004, Calibration of cameras of the H.E.S.S. detector, Astroparticle Physics, 22, 109

Aharonian, F., Akhperjanian, A. G., Barres de Almeida, U., et al. 2008, Energy Spectrum of Cosmic-Ray Electrons at TeV Energies, Physical Review Letters, 101, 261104

Aharonian, F., Akhperjanian, A. G., Bazer-Bachi, A. R., et al. 2006, Observations of the Crab nebula with HESS, A&A, 457, 899

Aharonian, F., Akhperjanian, A. G., Bazer-Bachi, A. R., et al. 2007, First ground-based measurement of atmospheric Cherenkov light from cosmic rays, Phys. Rev. D, 75, 042004

Berezinsky, V. S., Dokuchaev, V. I., & Eroshenko, Y. N. 2014, Small-scale clumps of dark matter, Physics Uspekhi, 57, 1

Berge, D. 2002, Master's thesis, Humboldt University of Berlin

Bernlöhr, K. 1999, Air Showers

Bernlöhr, K. 2008, Simulation of imaging atmospheric Cherenkov telescopes with CORSIKA and sim_ telarray, Astroparticle Physics, 30, 149

Borla Tridon, D. 2011, Measurement of the cosmic electron spectrum with the MAGIC telescopes, International Cosmic Ray Conference, 6, 47

Carrigan, S., Brun, F., Chaves, R. C. G., et al. 2013, Charting the TeV Milky Way: H.E.S.S. Galactic plane survey maps, catalog and source populations, ArXiv e-prints

Chang, J., Adams, J. H., Ahn, H. S., et al. 2008, Resolving electrons from protons in ATIC, Advances in Space Research, 42, 431

Chiang, J. & Romani, R. W. 1994, An outer gap model of high-energy emission from rotation-powered pulsars, ApJ, 436, 754

Dame, T. M., Hartmann, D., & Thaddeus, P. 2001, The Milky Way in Molecular Clouds: A New Complete CO Survey, ApJ, 547, 792

de Naurois, M. 2006, Analysis methods for Atmospheric Cerenkov Telescopes, ArXiv Astrophysics e-prints

de Naurois, M. & Rolland, L. 2009, A high performance likelihood reconstruction of γ-rays

for imaging atmospheric Cherenkov telescopes, Astroparticle Physics, 32, 231

Deil, C. 2011, PhD thesis, Ruperto-Carola University of Heidelberg

Delahaye, T., Lavalle, J., Lineros, R., Donato, F., & Fornengo, N. 2010, Galactic electrons and positrons at the Earth: new estimate of the primary and secondary fluxes, A&A, 524, A51

Dermer, C. D. 2007, in American Institute of Physics Conference Series, Vol. 921, The First GLAST Symposium, ed. S. Ritz, P. Michelson, & C. A. Meegan, 122–126

Di Mauro, M. 2016, Isotropic diffuse and extragalactic γ-ray background: emission from extragalactic sources vs dark matter annihilating particles, Journal of Physics Conference Series, 718, 042019

Dickey, J. M. & Lockman, F. J. 1990, H I in the Galaxy, ARA&A, 28, 215

Egberts, K. 2009, PhD thesis, Ruperto-Carola University of Heidelberg

Egberts, K. & H.E.S.S. Collaboration. 2011, The spectrum of cosmic-ray electrons measured with H.E.S.S., Nuclear Instruments and Methods in Physics Research A, 630, 36

Fabjan, C. W. & Gianotti, F. 2003, Calorimetry for particle physics, Reviews of Modern Physics, 75, 1243

Fegan, D. J. 1997, TOPICAL REVIEW: γ/hadron separation at TeV energies, Journal of Physics G Nuclear Physics, 23, 1013

Heck, D. e. a. 1998, Extensive Air Shower Simulation with CORSIKA: A Users Guide

Heitler, W. 1954, Quantum theory of radiation

H.E.S.S. Collaboration. 2016, to be published in Astronomy and Astrophysics

H.E.S.S. Collaboration, Abramowski, A., Acero, F., et al. 2010, VHE γ-ray emission of PKS 2155-304: spectral and temporal variability, A&A, 520, A83

Hillas, A. M. 1985, Cerenkov light images of EAS produced by primary gamma, International Cosmic Ray Conference, 3

Hinton, J. A., Funk, S., Parsons, R. D., & Ohm, S. 2011, Escape from Vela X, ApJ, 743, L7

Hoecker, A., Speckmayer, P., Stelzer, J., et al. 2007, TMVA - Toolkit for Multivariate Data Analysis, ArXiv Physics e-prints

Hofmann, W., Jung, I., Konopelko, A., et al. 1999, Comparison of techniques to reconstruct VHE gamma-ray showers from multiple stereoscopic Cherenkov images, Astroparticle Physics, 12, 135

Hunter, S. D., Bertsch, D. L., Catelli, J. R., et al. 1997, EGRET Observations of the Diffuse Gamma-Ray Emission from the Galactic Plane, ApJ, 481, 205

James, F. 1994, Minuit

Kalberla, P. M. W., Burton, W. B., Hartmann, D., et al. 2005, The Leiden/Argentine/Bonn (LAB) Survey of Galactic HI. Final data release of the combined LDS and IAR surveys with improved stray-radiation corrections, A&A, 440, 775

Kalberla, P. M. W. & Dedes, L. 2008, Global properties of the H I distribution in the outer Milky Way. Planar and extra-planar gas, A&A, 487, 951

Kalberla, P. M. W., Dedes, L., Kerp, J., & Haud, U. 2007, Dark matter in the Milky Way. II. The HI gas distribution as a tracer of the gravitational potential, A&A, 469, 511

Kalberla, P. M. W. & Kerp, J. 2009, The Hi Distribution of the Milky Way, ARA&A, 47, 27

Kieda, D. B., Swordy, S. P., & Wakely, S. P. 2001, A high resolution method for measuring cosmic ray composition beyond 10 TeV, Astroparticle Physics, 15, 287

Kohnle, A., Aharonian, F., Akhperjanian, A., et al. 1996, Stereoscopic imaging of air showers with the first two HEGRA Cherenkov telescopes, Astroparticle Physics, 5, 119

Kolitzus, D. 2015, PhD thesis, University of Innsbruck

Lemiere, A., Terrier, R., Jouvin, L., et al. 2015, Study of the VHE diffuse emission in the central 200 pc of our Galaxy with H.E.S.S, ArXiv e-prints

Linden, T. & Profumo, S. 2013, Probing the Pulsar Origin of the Anomalous Positron Fraction with AMS-02 and Atmospheric Cherenkov Telescopes, ApJ, 772, 18

Linsley, J. 1985, Standard value for the radiation length in air, International Cosmic Ray Conference, 7

Marandon, V. 2010, PhD thesis, APC CNRS/Universite Paris 7

Matthews, J. 2005, A Heitler model of extensive air showers, Astroparticle Physics, 22, 387

Montanus, J. M. C. 2014, An extended Heitler-Matthews model for the full hadronic cascade in cosmic air showers, Astroparticle Physics, 59, 4

Muslimov, A. G. & Harding, A. K. 2003, Extended Acceleration in Slot Gaps and Pulsar High-Energy Emission, ApJ, 588, 430

Nakamura, K. & Particle Data Group. 2010, Review of Particle Physics, Journal of Physics G Nuclear Physics, 37, 075021

Ohm, S., van Eldik, C., & Egberts, K. 2009, γ/hadron separation in very-high-energy γ-ray astronomy using a multivariate analysis method, Astroparticle Physics, 31, 383

Olive, K. A. et al. 2014, Review of Particle Physics, Chin. Phys., C38, 090001

Panov, A. D. 2013, Electrons and Positrons in Cosmic Rays, Journal of Physics Conference Series, 409, 012004

Parsons, R. D. & Hinton, J. A. 2014, A Monte Carlo template based analysis for air-Cherenkov arrays, Astroparticle Physics, 56, 26

Reynolds, S. P. 1997, in Bulletin of the American Astronomical Society, Vol. 29, American Astronomical Society Meeting Abstracts #190, 827

Reynolds, S. P. 2008, Supernova Remnants at High Energy, ARA&A, 46, 89

Rossi, B. 1952, High-energy particles

Rosswog, S. & Brüggen, M. 2011, Introduction to High-Energy Astrophysics

Schmidt, F. & Knapp, J. 2005, CORSIKA Shower Images

Serpico, P. D. 2009, Possible causes of a rise with energy of the cosmic ray positron fraction, Phys. Rev. D, 79, 021302

Serpico, P. D. 2012, Astrophysical models for the origin of the positron "excess", Astroparticle Physics, 39, 2

Skulls in the Stars. 2009, Skulls in the Stars

Staszak, D. & for the VERITAS Collaboration. 2015, A Cosmic-ray Electron Spectrum with VERITAS, ArXiv e-prints

Ulrich, M. 1996, PhD thesis, Ruperto-Carola University of Heidelberg, Germany

University of Minnesota. 2004, Generating Cerenkov Radiation

Venters, T. M. 2010, Contribution to the Extragalactic Gamma-Ray Background from the Cascades of very High Energy Gamma Rays from Blazars, ApJ, 710, 1530

Wakely, S. P. 2007, Ground-based Observations of TeV Cosmic Rays using Direct Cerenkov Radiation, Journal of Physics Conference Series, 60, 151

Winkel, B., Kerp, J., Flöer, L., et al. 2016, The Effelsberg-Bonn H i Survey: Milky Way gas. First data release, A&A, 585, A41

Zhang, B. & Harding, A. K. 2000, Full Polar Cap Cascade Scenario: Gamma-Ray and X-Ray Luminosities from Spin-powered Pulsars, ApJ, 532, 1150